

VAN ALLEN PROBES SCIENCE OPERATIONS

Abstract

This chapter describes the bent pipe structure of the Van Allen Probes data and science operations. The bent pipe structure required a primary Mission Operations Center (MOC) to handle the primary telemetry-receiving tasks as well as certain scientifically relevant ancillary tasks, e.g. utilization of the JPL NAIF SPICE system for time keeping. Each instrument science team developed a separate Science Operations Center (SOC) specifically focused on science data acquisition, data processing, instrument performance, and tools that supported the instrument team scientists. In parallel with the activities of the instrument SOCs were instrument data/modeling scientists with the task of providing a significant tool base to be used by the instrument science teams as well as making data available to the larger public scientific community. With a mission as complex as the Van Allen Probes each SOC had significant interactions with the other instrument SOC's and the project science team. These planned activities provided for critical coordination of observation modes during specific phases of the seven-year mission as well as for instrument cross-calibrations as appropriate. This chapter describes the specific data solutions implemented by each of the SOC's including discussion of the various coordination activities between each of the SOC's. Described are the underlying trade space in regards to the choices made by each team as well as lessons learned during the mission. The major over-all lesson learned has been the importance of the decision at the outset of the Project to implement individual team SOCs to provide timely and well-documented instrument data for the NASA Van Allen Probes Mission.

Authors

Jerry W. Manweiler¹, Harlan Spence², Geoff Reeves³, Reiner Friedel³, Brian Larsen³, Jonathan Niehof², Sonya Smith², Ruth Skoug³, Bern Blake⁴, Dan Baker⁵, Shri Kanekal⁶, Vaughn Hoxie⁵, Allison Jaynes², John Wygant⁷, John Bonnell⁸, Aaron Breneman⁷, Craig Kletzing⁹, Daniel Crawford⁹, Louis J Lanzerotti¹⁰, Andrew Gerrard¹⁰, Donald G. Mitchell¹¹, Lawrence Brown¹¹, Giuseppe Romeo¹¹, Grant Stephens¹¹, Aleksandr Ukhorskiy¹¹, Thomas Sotirelis¹¹, Robin J Barnes¹¹, Alexa Halford

¹ RBSPICE, Fundamental Technologies, LLC, Lawrence, KS

² ECT, University of New Hampshire, Durham, NH

³ ECT, Los Alamos National Laboratory, Los Alamos, NM

⁴ ECT, Aerospace Corporation, Los Angeles, CA

⁵ ECT, Laboratory for Atmospheric and Space Physics, University of Colorado, Boulder, CO

⁶ ECT, Goddard Spaceflight Center, Greenbelt, MD

⁷ EFW, University of Minnesota, Minneapolis, MN

⁸ EFW, University of California-Berkley, Berkley, CA

⁹ EMFISIS, University of Iowa, Iowa City, IA

¹⁰ RBSPICE, New Jersey Institute of Technology, Newark, NJ

¹¹ RBSPICE and Project, The Johns Hopkins University, Applied Physics Laboratory, Laurel, MD

¹² BARREL, Dartmouth College, Hanover, NH

Current Status of paper Section by Instrument

The following table shows what is done (✓), mostly done (□), NOT DONE (✗), and not needed (⊘).

Please review the table and please provide me content as soon as possible.

Section/Instrument	ECT	EMFISIS	EFW	RBSPICE	Gateway
Post Launch	✓	✓	✓	✓	⊘
Science Coordination	✓	✓	✓	□	⊘
Science Analysis Software	✗	✓	✓	✗	⊘
Science Gateway	⊘	⊘	⊘	⊘	✓
Lessons Learned	✗	✓	✓	✓	⊘
Appendices	✗	✗	✗	□	⊘

Chapter X – Introduction

The Van Allen Probes Mission Science Operations (SOC) was designed to provide the highest level of science return in one of most intense radiation environments to fly an operational mission around Earth. Science operations for this mission were broken into multiple levels that included command and control of the spacecraft and instruments; receipt of telemetry; processing of telemetry into higher level data products. The Mission Operations Center (MOC) as described in the RBSP Mission Book (Fox and Burch, 2012) (MD-I) managed communications between the ground segment and each spacecraft; handled spacecraft operations; and provided detailed ephemerid of the spacecraft for each of the instrument teams. The overall configuration of the Van Allen Probes operations was architected using a “bent-pipe” system where the MOC handled all elements related to the spacecraft and the instrument Science Operation Centers (SOC) handled all aspect of instrument operations.

The success of the extension of the standard satellite “bent-pipe” architecture for the data systems coupled with the distribution of operational responsibilities between the central MOC and the instrument SOC’s cannot be over stated. This configuration provided the highest level of flexibility for the instrument teams especially in situations where rapidly changing spacecraft and instrument conditions required very fast response in order to capture the highest telemetry rates and best quality of data or in some situations in order to protect the health of the instrument. As telemetry was processed into higher level data products, each team provided an instrument scientist and/or a data scientist to verify and validate the resulting data products. Since this responsibility was given to each instrument team and not a centralized production center, the scientists involved in the production of each specific data product had a clearer understanding of the specifics of the instrumentation than might have been in other situations and the production software could be quickly modified to handle changing flight configurations as opposed to the teams submitting change order requests to a centralized production center to be implemented, tested, and verified.

With all of this in mind, this paper provides and documents necessary updates for each of the Instrument Science Operations Centers (SOCs) as to any changes, development of software, and operations at the end of the mission. The following sections describe instrument configuration changes and other details for the following topical categories:

- 1) Post Launch Instrument and SOC Modifications
- 2) Science Coordination activities
- 3) Science Analysis Software
- 4) Science Gateway
- 5) Lessons Learned

It should be noted that in some instances the complexity of instrument operations and SOC operations was difficult to separate between the instrument papers of this volume and this paper. If the reader cannot find the desired information for which they are searching about a particular instrument, then they should also review the details provided in each of the specific instrument chapters of this volume.

Section 1 – Post Launch Instruments and SOC Modifications

The Van Allen Probes Mission started mission development with the announcement in May of 2006 of the selection of the Johns Hopkins Applied Physics Laboratory to build and operate the twin Radiation Belt Storm Probes spacecraft. The instrument selections were subsequently announced in the early July of 2006. Preliminary mission design, Mission Phase B, occurred from instrument selection through 2008. The formal Mission Phases C and D occurred from Jan 2009 to launch. During phase C/D, software design and development efforts were underway with the desire to support launch sometime in 2012. The software design and development required the instrument teams to build as flexible a software system as possible for the instrument specific targeted requirements. With the launch of the spacecraft in August of 2012, the instrument teams and SOC teams were required to shift into operations support no matter what the condition of the software systems. In many cases the primary software production systems for the higher-level data products were still in development and in some cases still in design. Delay in development of the higher-level data products occurred in some instances because the teams needed to understand the instrument performance and have a reasonable understanding of the scientific capabilities before attempting to fully specify higher level data products.

In this light it becomes understandable that changes were necessary to both instrument operations and SOC software to accommodate and adapt to the flight of the instruments in what is considered one of the most hostile environments for spacecraft operations in the solar system. The following subsections attempt to describe changes to the SOC's operationally and/or software configuration post launch as instrument performance and the radiation belt environments were better understood.

Energetic Particle, Composition, and Thermal Plasma Suite (ECT)

HOPE Level 2 Processing Algorithms

HOPE data are affected by changes in on-board energy and angular bins, both over the course of the mission and within an orbit. These are described in Skoug et al. (2021).

HOPE fluxes incorporate a time-varying efficiency correction. This algorithm, and other details of HOPE processing, are detailed in Voskresenskaya et al. (2021). For each of the five sensor heads (pixels) and 72 energy channels, an absolute efficiency is calculated as $(\text{coincidences} * \text{coincidences}) / (\text{starts} * \text{stops})$ and normalized to January 2013, with the switch to the final 72-bin energy assignments on board occurred. This value is calculated hourly by summing each of the counts for the hour; if an hour contains less than 3600 coincidence counts, the time window is expanded until the threshold is reached, and the same relative efficiency value used for all times within the window. Data gathered for $L < 2.5$ are excluded. Earlier releases of the data used a variant of this algorithm; the earliest releases contained no time-varying correction.

HOPE Level 3 Processing Algorithms

HOPE level 3 files are calculated from the level 1 (counts) files and an intermediate pitch angle tags product.

Time tags from level 1, which has a single tag for the entire spin and all energy sweeps, are converted to a single unique tag for each sector of the spin, and each energy value, time-resolving the energy sweep. The spacecraft spin is broken into sectors by HOPE, and during each sector a complete energy sweep is made. This means different energies are measured at different times, and thus slightly different spin phases and look directions. EMFISIS Level 2 data are used to find the magnetic field for each of these

timestamps, with the field interpolated to the timestamp from available field data using the SLERP approach as implemented by LANLGeoMag (Henderson et al. 2018). The angle between the field and the HOPE look direction (rotated into the same frame as the magnetic field using SPICE) is calculated for each record, detector, sector, and energy, and recorded as the pitch angle (0-180 degrees) in the “tags” file. An orthogonal gyro angle (0-360 degrees) is also calculated. Zero gyroangle is defined as the direction of the cross product of the magnetic field direction and the spacecraft spin axis. Before EMFISIS level 2 files were available, EMFISIS quicklook files were used, but they have not been used for the final archive.

From the level 1 counts and the pitch angle tags, a general binning code creates binned level 3 files. This code sums counts into 2D array (for each time) by pitch angle and gyrophase, also tracking total number of samples in each bin. These arrays are treated identically to the 2D array, by detector number and sector. Thus, the same code that calibrates counts to fluxes (count rates, uncertainties) for level 2 is used to calculate fluxes in level 3. For level 3 pitch angle files, a single gyrophase bin is used (and removed on output), with eleven pitch angle bins: nine bins of 18 degrees, and half-width bins for 0-9 and 171-180 degrees, to provide higher resolution at the loss cone. The same code and inputs are used to produce files containing 5 pitch angle and 8 gyroangles as inputs to moment calculations.

REPT Processing Algorithms

The REPT processing algorithms are described in Baker, et. al, 2021.

Combined electron product

A combined electron product, using all ECT sensors (HOPE, magEIS, REPT), is described by Boyd et al. (2021).

Magnetic Ephemeris variables

To provide easy context to the scientific observations, certain quantities from the magnetic ephemeris files (Henderson et al., 2021) are added to all ECT data files. These are interpolated from the one-minute MagEphem files to the same timestamps as the ECT data. This postprocessing step is applied after the generation of the L2 and L3 files with instrument-specific code, using a single generic code. Included quantities are MLT, Roederer L*, model magnetic field at the spacecraft, McIlwain L, model equatorial field, and spacecraft position in geographic coordinates. All are using the OP77Q model.

Electric and Magnetic Field Instrument Suite and Integrated Science (EMFISIS)

The EMFISIS instruments have operated as planned throughout the mission with essentially no changes. A few parameters have been adjusted:

- From Oct 2021-Dec 2021, the length of the electric field booms was increasing, so the parameter used for calculating the electric field was adjusted to provide the correct length as the booms were extended. These factors are incorporated into the EMFISIS data products.
- After monitoring the response to large amplitude signals, the built-in attenuator was switched on continually after early 2013 to ensure minimal clipping of signals. This cut is 15 dB and is included in the physical units for EMFISIS data products.
- Approximately halfway through the mission the threshold for change magnetometer ranges was lowered by about 500 nT to ensure correct switching as the spacecraft moved outbound. Because of the rapid motion of the spacecraft, this change is essentially unnoticeable, moving the location of the change outbound by a fraction of an Earth radius. Indeed, after the change no data users ever noticed!

Beyond these operational changes in the instruments, EMFISIS steadily revised software to correct for the usual coding and calibration errors. For L2 and L3 products there have essentially no change since the second quarter of 2021.

The EMFISIS L4 density product has remained unchanged in form, but due to the need for human intervention to ensure accuracy, the data set is not 100% complete, but is complete at a level of great use to the community.

The L4 wave-normal analysis (WNA) project (described in the EMFISIS post-flight instrument paper) has been the subject of intensive work to improve the electric field accuracy by employing a model of the sheath impedance to the plasma to get correct amplitudes and phases. This effort has been quite successful and provides one of the most accurate sets of 3D electric and magnetic field wave products in terms of parameters such as Poynting flux, ellipticity, polarization, etc.

Some data products produced by EMFISIS were not originally planned for, but were developed because of their utility. These include records of thruster firings, spacecraft charging events, and axial boom shadowing. EMFISIS also developed a data product to provide a set of spacecraft housekeeping data so that instruments could understand housekeeping events which might affect their operation.

Electric Fields and Waves Suite (EFW)

This chapter provides a brief description of instrument and science operations at the Van Allen Probes Electric Fields and Waves (EFW, Wygant et al., 2014) Science Operating Center (SOC). The primary activities of EFW SOC - divided between the University of Minnesota and the University of California Berkeley - included data processing, instrument operation and commanding, scheduling of sensor diagnostic tests, and the collection and telemetry of burst data including support of a number of collaborative campaigns with other missions.

In this Chapter we discuss the EFW data processing chain leading to the production of publicly available data products, and the operation of the burst 1 instrument. Further details are available in the EFW bookend chapter.

EFW data processing chain

This section is an overview of the EFW data processing chain from raw telemetry (level 0) files to fully calibrated, publicly available level 3 files. On a near daily basis UCB SOC received raw telemetry files

from the Mission Operating Center (MOC) at Johns Hopkins University Applied Physics Laboratory. These were decommutated and turned into time-tagged but un-calibrated (level 1 ADC counts) science and housekeeping data quantities. These files were then transferred to UMN SOC where they underwent further calibration. This included the application of a rough calibration to attain physical units (such as mV/m) used for the production of the daily survey *quicklook* plots available at <http://rbsp.space.umn.edu/survey/>. In a few days' time, after official ephemeris data and (roughly calibrated) EMFISIS magnetometer data became available, the quicklook plots were updated to include the more accurate spin-fit survey electric fields. In addition, calibrated level 2 files were developed, and these included quantities such as spin cadence (spin-fit) electric fields in modified GSE (mGSE) coordinates (see EFW bookend chapter Section 4), survey cadence (16 or 32 s/sec) electric-fields in mGSE, probe potentials, and estimates of plasma density. Finally, in the following weeks or months, level 3 data containing the best calibration available were produced as ISTP-compliant CDF files. These files, available at CDAWeb, represent the best possible EFW calibrated data and are recommended for public use.

Radiation Belt Storm Probes Ion Composition Experiment Science Operations:

The RBSPICE Science Operations Center (SOC) as described by Mitchell et. al (2013) was developed over the course of five years prior to launch. Development and enhancement of the operational and scientific software continued throughout the duration of the seven-year mission. This section the changes and enhancements to the RBSPICE SOC and data as compared to Mitchell et. al (2013). Figure 1 presents the final data flow schematic as implemented by the RBSPICE SOC, located at Fundamental Technologies, LLC (FTECS) in Lawrence, KS, and the RBSPICE SOC located at JHUAPL in Laurel, MD. Pre-release Magnetic field data (EMFISIS-L0) was included to allow the RBSPICE SOC to create preliminary pitch angles for analysis in the MIDL software. Enhancements to the external interfaces from FTECS included the development of a RESTful API based upon the Heliophysics Application Programmer's Interface

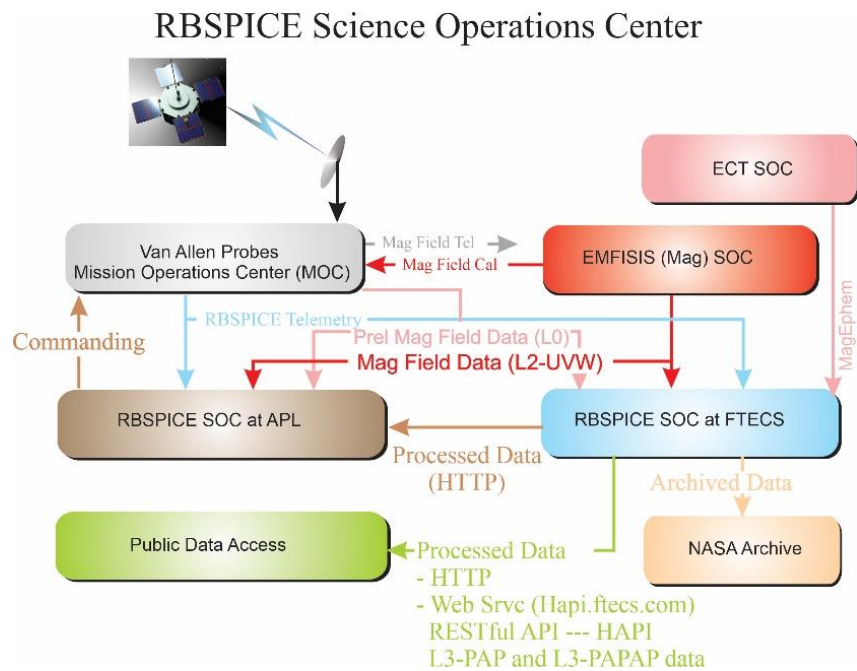


Figure 1 RBSPICE Data Flow Schematic. Figure derived from Mitchell et. al (2013) and updated with final implemented information.

(HAPI – see Vandergriff et. al, 2019) which allows for streaming of RBSPICE data using a JSON object specification.

Summary of RBSPICE Data Pipeline and Products

The RBSPICE data processing pipeline was architected and designed using the Unified Modeling Language (UML – Rumbaugh, 2004; Booch, 1999). It was implemented in Microsoft C# (Wiltamuth, 2006) to run on Microsoft Windows 8.1 with final production occurring on Microsoft Windows 10. The production systems were based upon software and systems used for production of the Cassini Magnetospheric Imaging Instrument (MIMI) data (Krimigis et. al, 2004) although significant modifications and enhancements were made to the overall software systems with a design toward utility and generalization instead of high-speed performance.

The RBSPICE data production pipeline was developed as a series of segments based upon NASA Data Level definitions (see Appendix A) (CSV=Comma Separated Value, CDF=Common Data Format (Kessel, 1995)). Production of each NASA data level in the RBSPICE SOC occurred as a set of dependent steps with all data products for any particular day being generated for each production segment (NASA data level). Enhancement to the L3 data production included two additional products using team-defined binning algorithms. The primary L3 data product includes the L2 differential flux along with calculated pitch and phase angles for each record for each telescope. Additionally, magnetic ephemeris coordinate information is included which was taken directly from the ECT Magnet Ephemeris (MagEphem) data product [Reeves et al., 2021]. See Table 1 for details on RBSPICE data products time resolution, data formats, and primary data units.

Table 1 List of RBSPICE data products per NASA Data Level including time resolution, data formats, and primary data units.

Data Level	Description	Time resolution	Format(s)	Units
L0	Repackaged CCSDS PTP (Payload Telemetry Packet) records	Sector based	CSV, CDF	[# (counts)],
L1	Rate data in instrument units	Sector	CSV, CDF	[#/sec]
L2	Differential flux in physical units	Sector	CSV, CDF	[#/(cm ² *sec*str*MeV)] ¹
L3	Copy of L2 Differential flux packaged with: Magnetic field as pitch angles and specific Ephemeris data	Sector	CDF	[#/(cm ² *sec*str*MeV)]
L3-PAP ²	Differential flux binned into Pitch Angle bins	Spin	CDF	[#/(cm ² *sec*str*MeV)]
L3-PAPAP ²	Differential flux binned into Pitch and Phase angle bins	Spin	CDF	[#/(cm ² *sec*str*MeV)]
L4	Phase Space Density (PSD) ³	Spin Averaged	CDF	[#/(km ⁶ /sec ³)]

¹ Units defined in COSPAR ISTEP Panel on Radiation Belt Environmental Modeling (PRBEM) standards (Bourdarie, 2012))

² PAP and PAPAP designations are not part of the NASA Data level specification but are included since they represent additional RBSPICE Level 3 data products have alternative data organization strategies.

³ L4 PSD was an originally proposed data product but due to limitation of resources is not currently planned for production.

The L3 Pitch Angle and Pressures (L3-PAP) contains L2 differential flux binned by pitch angle, species specific perpendicular and parallel partial pressures, OMNI flux, total intensity, and the species specific partial density. Pressures and density calculations include binned flux for a limited set of energy

channels chosen as reliable and uncontaminated by the RBSPICE instrument/science team. The L3 products called the Pitch Angle, Phase Angle, and Pressures (L3-PAPAP) contains L2 differential flux binned by pitch and phase angles. Phase angles are calculated using the Solar Magnetospheric (SM) reference frame with the zero-degree phase toward the Sun (\hat{x}_{SM}), and the 90° phase in the $-\hat{y}_{SM}$ direction. L3-PAPAP includes the calculation of species-specific pressures, OMNI flux, intensity, and density as in the L3-PAP files. See 2 for details on each data category identifying the data sources, units, access, and overall mission data volume. The RBSPICE instruments were capable of distinguishing between electrons and individual ion species, specifically protons, helium, and oxygen – for further instrument details see Gkioulidou (2021).

Table 2 List of RBSPICE data products by NASA Data Level with data source, accessibility, and total mission data volume.

Data Category	Data Source	Measurement Type / Units	Publication/Access Level	Mission Data Volume
MOC Data Products – not instrument specific	MOC	NA	RBSPICE team only	~419 GB – A ~407 GB – B
RBSPICE Instrument Data (telemetry/Level 0)	RBSPICE SOC	Counts [#]	RBSPICE team only	~514 GB – A ~500 GB – B
RBSPICE Level 1 Data	RBSPICE SOC	Rate [#]/sec	RBSPICE team and Archive systems	~1.93 TB – A ~1.87 TB – B
RBSPICE Level 2 Data	RBSPICE SOC	Flux [#]/(sec*sr*cm ² *MeV)	RBSPICE team and Archive systems	~2.75 TB – A ~2.64 TB – B
RBSPICE Level 3 Data	RBSPICE SOC	Flux and Pitch angles [#]/(sec*sr*cm ² *MeV)	General Public	~1.43 TB – A ~1.38 TB – B
RBSPICE Level 3 PAP data	RBSPICE SOC	Binned Flux by Pitch Angle [#]/(sec*sr*cm ² *MeV)	General Public	~230 GB – A ~224 GB – B
RBSPICE Level 3 PAPAP data	RBSPICE SOC	Binned Flux by Pitch/Phase [#]/(sec*sr*cm ² *MeV)	General Public	~900 GB – A ~840 GB – B
RBSPICE Level 4 data	RBSPICE SOC	Binned Phase Space Density (s ³ /km ⁶)	General Public	~TBD ~TBD

Time System Specifications

The RBSPICE time system utilized the NASA Navigation and Ancillary Information Facility (NAIF) SPICE software system (Acton, 1996; Acton, 2017) to convert spacecraft time (SCLOCK) into the J2000 Ephemeris Time system (ET) (Fukushima, 1995). The MOC was responsible for the production of SPICE kernels maintaining the temporal map between SCLOCK and ET (J2000 epoch). All spacecraft clock event resets were handled by the MOC without creating new SCLOCK partitions.

MOC generate data files were produced for each SCLOCK day (86400 SCLOCK ticks). The first SCLOCK day was created in synch with the UTC Day of launch. Each SOC produced UTC Day files for each data product. This required correct handling of input telemetry files realizing that any particular day of telemetry might include data from as many as three different UTC days. The RBSPICE SOC system created a database map of the SCLOCK to UTC start and stop times for each MOC telemetry file. This allowed for a fast query to find telemetry files containing data for any particular UTC Day.

Table 3 RBSPICE Data Products catalogue of primary counting products along with required ancillary data products showing species, number of energy channels, and the type of data generated at each NASA data level.

Product	Species	Energy Bins	L0 Data Type	L1 Data Type	L2 Data Type	L3 Data Type	L4 Data Type
Electron Energy Mode Basic Data	e ⁻	NA	Counts	Rates			
Ion Energy Mode Basic Data	Ions	NA	Counts	Rates			
Ion Species Mode Basic Data	Ions	NA	Counts	Rates			
Low Energy Resolution High Time Resolution Electron Species Data ¹	e ⁻	14	Counts	Spectra	Spectra Flux	PAD, Aggregates	PSD, 2nd, 3rd Adiabatic,
High Energy Resolution Low Time Resolution Electron Species Data ¹	e ⁻	64	Counts	Spectra	Spectra Flux	PAD, Aggregates	PSD, 2nd, 3rd Adiabatic,
High Energy Resolution Low Time Resolution Ion Species Data ¹	Ions	64	Counts	Spectra	Spectra Flux	PAD, Aggregates	PSD, 2nd, 3rd Adiabatic,
High Energy Resolution Low Time Resolution TOFxE Proton Data	H ⁺	32	Counts	Spectra	Spectra Flux	PAD, Aggregates	PSD, 2nd, 3rd Adiabatic,
TOFxE Proton Data	H ⁺	14	Counts	Spectra	Spectra Flux	PAD, Aggregates	PSD, 2nd, 3rd Adiabatic,
TOFxE non-Proton Data	He ⁿ⁺ , O ⁿ⁺	28	Counts	Spectra	Spectra Flux	PAD, Aggregates	PSD, 2nd, 3rd Adiabatic,
Low Energy Resolution High Time Resolution TOFxE Ion Species Data	Ions	64	Counts	Spectra	Spectra Flux	PAD, Aggregates	PSD, 2nd, 3rd Adiabatic,
Space Weather Data	All	NA	Counts	Rates	Flux		
Auxiliary Data	NA	NA	Aux data				
Critical Housekeeping Data	NA	NA	HSK				

Telemetry Processing and Data Production

The RBSPICE Level 0 data contains 33 individual data products, see for a listing of the primary counting data products together with the required ancillary data products used for production. Each product file contains an unpacked copy of the RBSPICE telemetry file decoding the CCSDS Payload Telemetry Packet (PTP) (Packet Telemetry, 2000) records into count and support data. The only time field provided by each PTP is the spacecraft SCLOCK and the internal RBSPICE flight software derived time fields.

The produced L0 products include three time fields formats: ET (double precision), SCLOCK (string), and Universal Time Coordinated (UTC-string) using the ISO(T) 8601 Ordinal Time Format Specification [ANSI INCITS 30-1997 (R2008) formatted as “CCYY-DDDTHH:MM:SS.hhh”. CCYY = century and year, DDD = ordinal Day of Year, HH = hour, MM = minute, SS = integer second, and hhh = decimal seconds to milliseconds resolution. SCLOCK values are formatted in NAIF Type 1 SCLOCK format [NASA NAIF SPICE, 2010] as [part/ticks:fine] where part = integer partition (always 1), ticks = major ticks (~1 second), and fine = minor ticks of the spacecraft time system in 2⁻¹⁶ increments.

The following sections provide updates to the algorithms used in the creation of the Level 0 Count Files, the Level 1 Rate files, and the Level 2 Intensity (flux) files. Subsequent sections provide the detailed algorithms used in the creation of the Level 3 Pitch Angle files, the Level 3 PAP files, and the Level 3 PAPAP files. A final section discusses the algorithms needed to calculate Level 4 Phase Space Density (PSD) data. Details presented for each of these steps are sufficient in conjunction with the details provided in the original MB-I and the RBSPICE Data Handbook (Manweiler, 2019) to allow other software developers to write their own translation workflow.

Level 0 data product

The Level 0 data products are organized by ephemeris time (ET), spacecraft spin number, and the RBSPICE instrument created virtual sector number with 36 sectors per spin. The starting time of each

sector is determined by the RBSPICE flight software coupled with the spacecraft 1 PPS (Pulse Per Second) status record sent to the RBSPICE instrument. The ground software calculates the beginning of each sector based upon the nominal spin period provided by the RBSPICE Auxiliary telemetry record for the current spin/sector using the Spin Duration field. In the situation where either spacecraft goes into eclipse and loses the nominal 1 PPS signal then the RBSPICE flight software utilizes a hard-coded nominal spin period of 12 sec to calculate the duration of each spin and to time tag the beginning of the next spin record.

Time Stamp Generation

The RBSPICE Auxiliary telemetry (Aux) product is the only component of the received RBSPICE telemetry that provides the ability to create a high time resolution conversion from the full SCLOCK to ET (J2000 epoch). Aux packets are generated by the RBSPICE instrument at the end of each spin and each include a time stamp derived from the timing information provided by the spacecraft 1 PPS (Pulse Per Spin) signal. The SCLOCK value is a four-byte unsigned integer which cycles from 0 to $(2^{32}-1)$. The Fine SCLOCK value is a two-byte unsigned integer number which cycles from 0 to $(2^{16}-1)$ and is in units of $(1/2^{16})$ SCLOCK ticks. In general, each tick of the SCLOCK is approximately 1 second, although this relationship can drift depending upon the heating and cooling of the spacecraft. The SCLOCK value is not a unique value, but repeats every 136.19 years. A compression of the SCLOCK value from the instrument was necessary when converting into NAIF SCLOCK values since the NAIF Fine specification is in 1/50000 sec units. The x323 telemetry record time stamps are decoded by the RBSPICE SOC software system and the resulting SCLOCK and Fine SCLOCK values are converted into a time stamp using the algorithm in Figure 2.

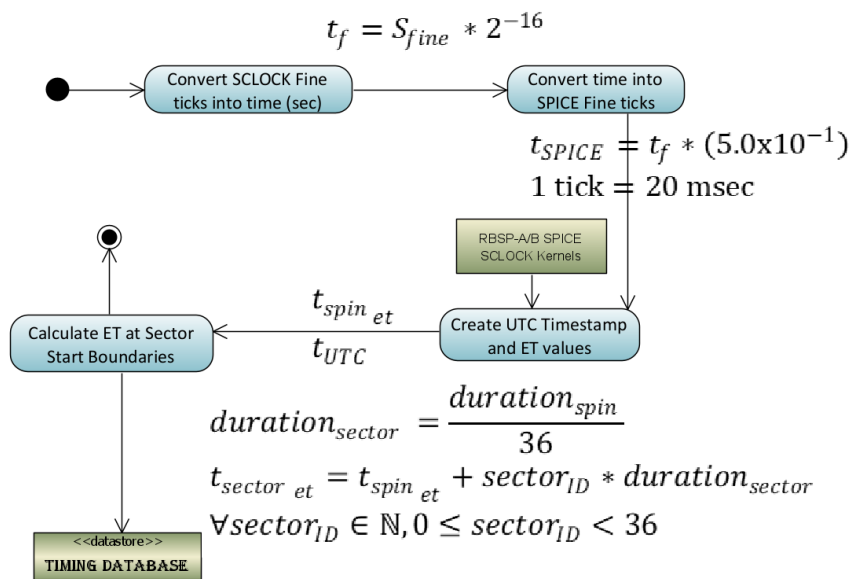


Figure 2 Diagram showing the calculation of timing factors for RBSPICE telemetry.

Duration of Measurement and Start/Stop Times

Level 0 processing calculates the duration of each measurement at the same time the sector timestamp is calculated. The duration cannot be simply calculated as the difference between the next sector and

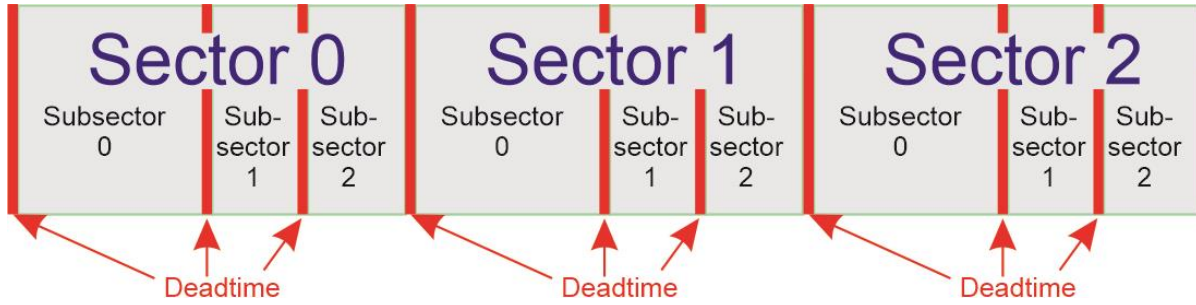


Figure 3 Sector and subsector scheme used by RBSPICE also showing inter-sector and intra-sector dead times.

current sector start times since the RBSPICE instrument has three possible measurement modes which can be assigned to one of the three available subsector accumulation time periods. Figure 5 displays the sector division into three unequal time sized subsector partitions: $\Delta t_0 = \frac{1}{2} t_{sect}$; $\Delta t_1 = \frac{1}{4} t_{sect}$; $\Delta t_2 = \frac{1}{4} t_{sect}$. The RBSPICE instrument can be commanded to use any measurement mode (electron energy, ion energy, and ion species) in any combination of subsectors, providing the ability to simultaneously measure electrons and ions within a sector or, alternatively, to use a single type of measurement for higher time resolution science. Sector “dead time (dt)”, also shown, occurs at the end of each subsector

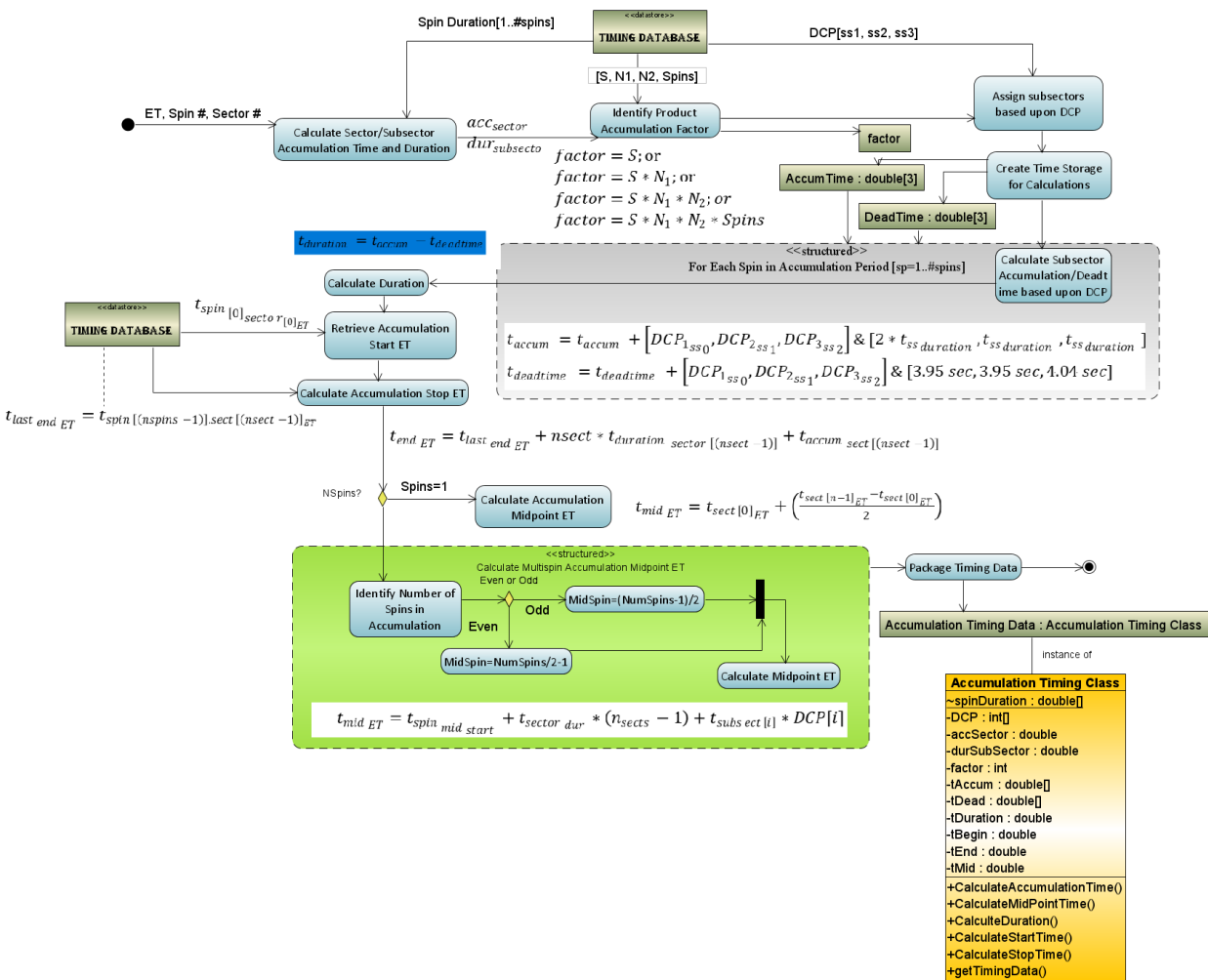


Figure 4 Activity Diagram showing the algorithmic steps in the production of the Level 0 files.

due to instrument electronic state changes, $\Delta t_{01dt} = 3.94 \text{ ms}$; $\Delta t_{12dt} = 3.95 \text{ ms}$; $\Delta t_{20dt} = 4.04 \text{ ms}$. Subsector accumulation time is $\Delta t_{0acc} = \Delta t_0 - \Delta t_{20dt}$; $\Delta t_{1acc} = \Delta t_1 - \Delta t_{01dt}$; $\Delta t_{2acc} = \Delta t_2 - \Delta t_{12dt}$.

The key values required to properly calculate the measurement duration are found in the Aux telemetry packet: Spin Duration (in seconds), Accumulation Mode Values (S, N1, N2, Spin) and Data Collection Pattern (DCP) – the combination of instrument modes for each subsector. The timing system calculates the duration of the measurement using the algorithm in Figure 4. The diagram showing the structured activity (green insert box) provides some detail of the calculation of the midpoint time for the accumulation. For single spin accumulations this calculation is very straight forward as the start ET plus half the delta time for the accumulation, ($t_{mid_{ET}} = t_{start_{ET}} + (t_{end_{ET}} - t_{start_{ET}})/2$). Multi-spin accumulation involves a more complex calculation, see Figure 6. In this example, the calculation is done for a starting accumulation in sector 0 and accumulating over 4 sectors and 10 spins, i.e., $S = 1$; $N_1 = 2$; $N_2 = 2$; $Spin_j = 10$. The sectors involved in the measurement are identified in the table as green with a white square in the middle. A “false” midpoint time is calculated using the simple algorithm $t_{mid_{ET}} = t_{start_{ET}} + (t_{end_{ET}} - t_{start_{ET}})/2$ as indicated with the “x” in the red square outside the actual accumulation time.

The correctly calculated midpoint is shown as the bullseye in the middle of the two white squares. Even this calculation requires attention because the two white squares in the example are still one full spin apart. If the number of spins used in the accumulation is even then the midpoint time is the end of the first of the two white squares but if the number of spins used in the accumulation is odd then there is only a single sector in the white square so the midpoint is halfway between the start and stop of that sector.

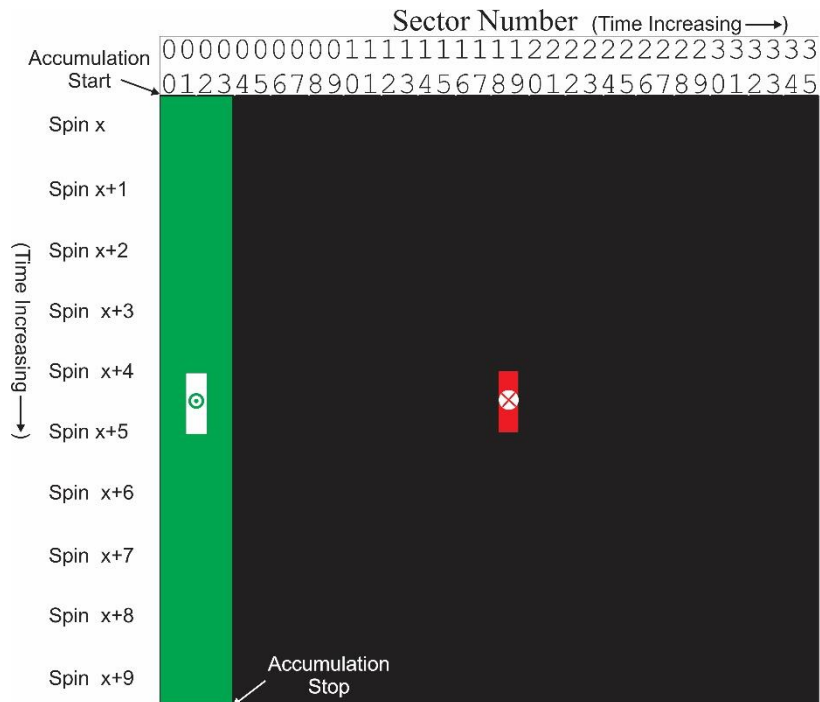


Figure 6 shows the false (red) and correct (green) midpoint calculations of the midpoint time for the current multi-spin accumulation period over a few sectors.

The rest of the RBSPICE Level 0 data product production is thoroughly described in the online version of the RBSPICE Data Handbook (Manweiler, 2019).

Level 1 Processing Algorithms

Level 1 processing is done by converting Level 0 count data into Level 1 rate data as a series of algorithmic steps for which the critical component is the calculation of the Rate-in versus the Rate-out (R_{in} vs R_{out}) algorithm. This is necessary since the instrument electronics has a maximum clock cycle limiting the highest rates observable due to multiple particle events occurring at the same time. Table 4 presents the fields and their definitions, type, and default values that are used in the subsequent R_{in} vs R_{out} formula:

Table 4 R_{in} vs R_{out} R_{in} vs R_{out} variable names, descriptions, variable type, and encoded values.

Name	Description	Type	Value(s)
MaxIDLE	Maximum number of 100ns intervals for which data can be accumulated	UInt32	$\frac{\Delta t}{10^{-7}}$
ClkPeriod	Number of nanoseconds in the RBSPICE DPU clock period	UInt32	100
STDead	Start counter dead time due to synchronization logic	UInt32	2
SPDead	Stop counter dead time due to synchronization logic	UInt32	2
SPVeto	Interval in which additional stop pulses cause the event to be discarded	UInt32	2
RDTVeto	Interval for inhibiting start and stop counter during chip TOF reset	UInt32	1
PKDReset	Interval for resetting the peak detector	UInt32	4
PURVeto	Interval during which a second SSD pulse causes event to be discarded	UInt32	7
TOFxE_PURVeto	Interval during which a second SSD pulse causes event to be discarded (<i>changed in software configuration file for TOFxE only</i>)	UInt32	24
K1E_E	Correction constant term for valid TOFxE events	Float	0.3
K1E_PH	First order correction constant term for valid TOFxPH events	Float	0.15
K2E_PH	Second order correction constant term for valid TOFxPH events	Float	0.15
STMISS	The number of FPGA clock cycles are missed each sector Code variable names: <code>_tofxph_RvsR_EFact</code> or <code>_tofxe_RvsR_Efact</code>	UInt32	2
Cssd	FPGA clock ticks or the required value to reproduce MHR from FPGA, based upon the IBSR record only	UInt32	2
CphSC	Represents the factor for which PH counts miss from the start0 counts	Float	$C_{phA}=0.860$ $C_{phB}=0.775$

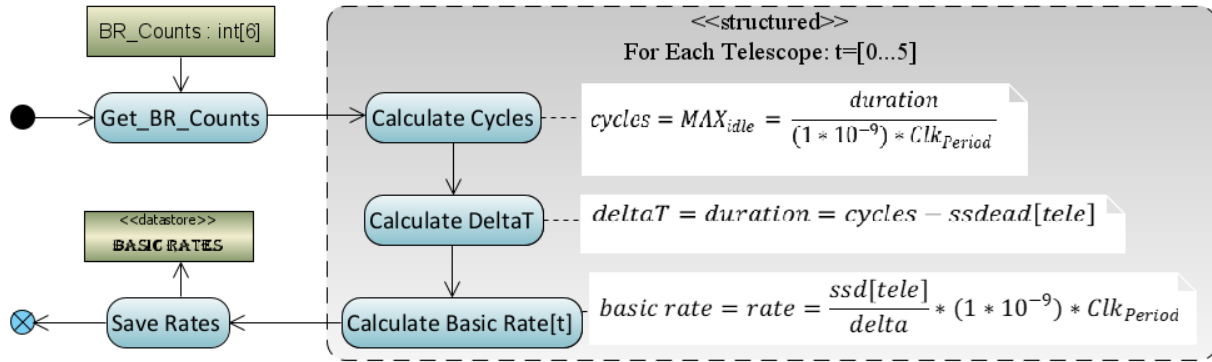


Figure 7 Algorithmic diagram displaying the conversion of basic counts into basic rates.

R_{in} vs R_{out} Algorithm and Formula for specific data products

Basic Rates: EBR (APID: x312), IBR (APID: x313), and ISBR (APID: x315)

Basic rate telemetry includes the measured counts (SSD), dead time correction values (SSDDead) per telescope, and the calculated duration of the accumulation. These values are converted to a rate value using the algorithm in Figure 7:

Energy Rates

The conversion algorithm of the counts obtained for the following energy mode products, ESRLEHT (APID: x317), ISRHELT (APID: x318), and ESRHELT (APID: x319), requires an understanding of the spin information (APID: x323) and the R_{in} vs R_{out} corrected basic rate data (EBR for ESRLEHT and ESRHELT, IBR for ISRHELT) to calculate the rate. For purposes of this algorithm, the count values in the telemetry are referenced as h_{ij} where i refers to the telescope number and j refers to the energy channel of the

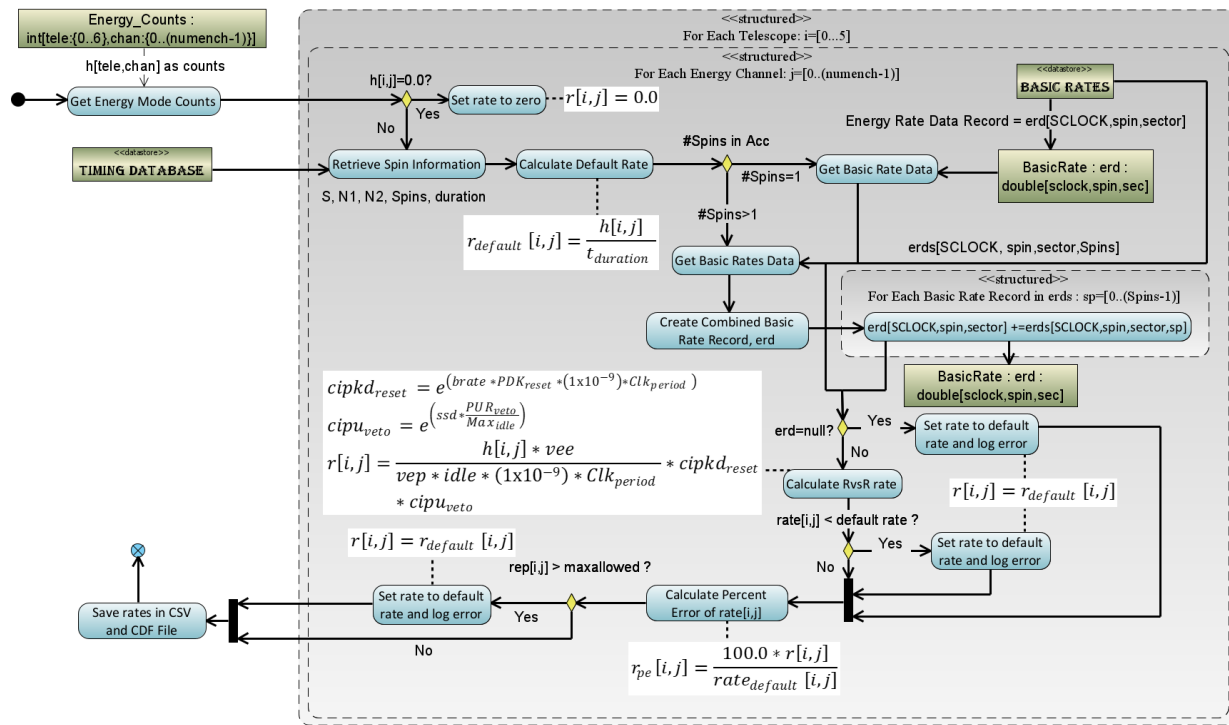


Figure 8 Algorithmic diagram displaying the conversion of Energy Mode counters into Energy rates

measurement. Figure 8 shows the algorithm used in the RBSPICE SOC software for each telescope and each energy channel. The figure includes the formulas used in the calculations.

Species TOF_xPH Rates

Figure 9 displays the algorithm used in the conversion of the species mode TOF_xPH measurements for products TOF_xPHHLEHT (APID: x31D) and TOF_xPHHHELT (APID: x31E) which follows the algorithm for the calculation of Energy Rates (see Figure 8). The key difference in the diagram is the use of the corrected Ion Species Basic Rates (ISBR – APID: x315) and differences in the formula used in the R_{in} vs R_{out} calculation.

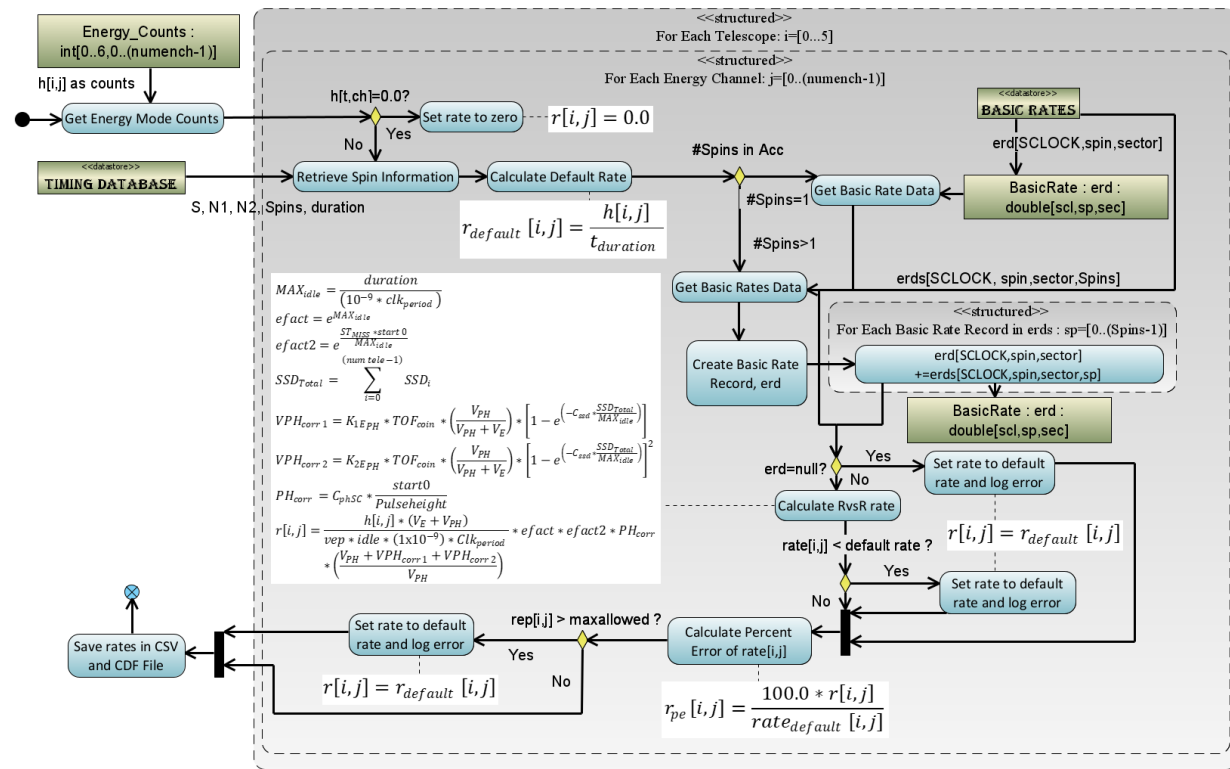


Figure 9 Algorithmic diagram displaying the conversion of TOF_xPH Species Mode counters into TOF_xPH rates

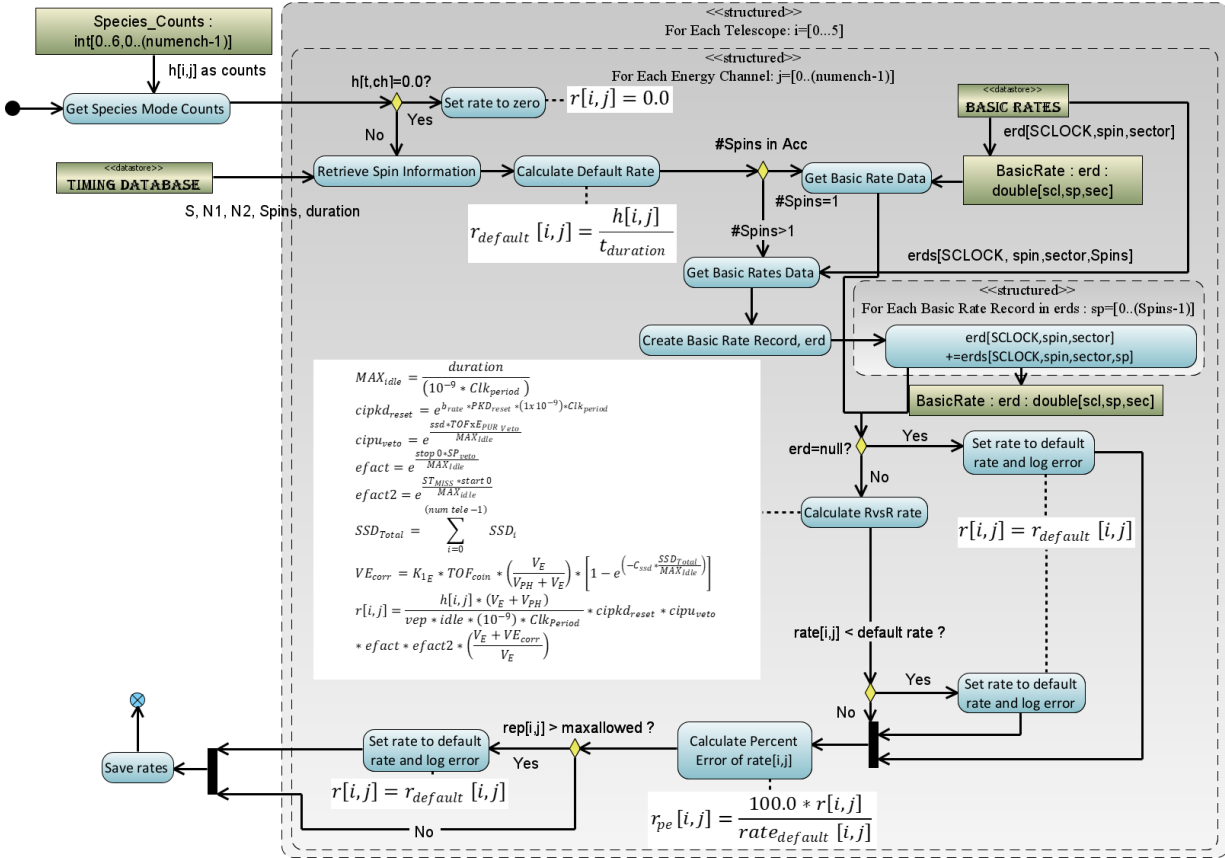


Figure 10 Algorithmic diagram displaying the conversion of TOFxE Species Mode counters into TOFxE rates

Species TOFxE Rates

Figure 10 displays the algorithm used in the conversion of the species mode TOFxE measurements for products TOFxEIOn (APID: x31A), TOFxEH (APID: x31B), and TOFxEonH (APID: x31C) follows a similar algorithm as for Species TOFxEH rates (see Figure 9). The key difference in the diagram is the formula used in the R_{in} vs R_{out} calculation.

Error Calculations for Rate Files

As counts are converted into rates, the Level 1 files capture the statistical Poisson error for the purposes of error propagation in later data levels. Additionally, since we are keeping track of the percent error and including the errors in higher level data products, we have the ability to easily propagate the errors when we do various integration or telescope combination activities in the level 3 data products, see discussion of errors in the Level 3 PAP / PAPAP sections and also Figure 11 for the basic error propagation algorithm used in the RBSPICE production system.

Level 2 Processing Algorithms

The primary activity in processing the Level 1 data into Level 2 data is to convert the rate data into particle intensity (flux) data. This is done in a series of algorithmic steps in which the Level 1 rate data is read into memory, the calibration data for the SC and product are loaded, the intensities are calculated, and the intensities are then written to a Level 2 file. Additional fields are added to the Level 2 file in order to partially fulfill the standards defined by the Panel on Radiation Belt Environmental Modeling (PRBEM: COSPAR ISTEP PRBEM Committee, 2010).

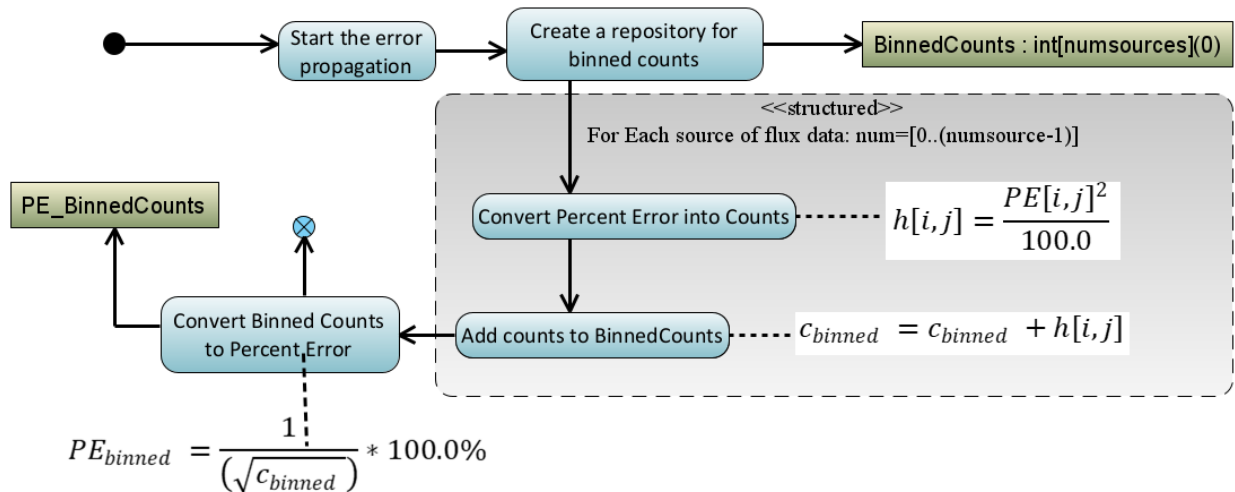


Figure 11 Error propagation algorithm used in later data production especially for the Level 3 PAP and PAPAP files where flux is binned and the errors for any particular bin must be carefully calculated.

Calculation of Intensities (Differential Flux)

Conversion of RBSPICE data into differential flux requires knowledge of the channel and product specific RBSPICE calibration factors. The calibration data can be found on the RBSPICE website at the following locations: http://rbspice.ftecs.com/RBSPICEA_Calibration.html and http://rbspice.ftecs.com/RBSPICEB_Calibration.html or archived at the CDAWeb RBSPICE archive. Note that the reference table in the calibration files of TOF-trigger_ion E is referring to the RBSPICE TOFxE_Ion data products.

The data is organized by product type and contains the necessary information needed to convert RBSPICE rates into differential flux. The calibration data fields are fully described in the RBSPICE Data Handbook. Rates are converted into Intensities using the following equation,

$$flux[tele, enchan] = \frac{rate[tele, enchan]}{(E_{High} - E_{Low}) * G_{size} * eff}$$

The value of the geometrical factor, G_{size} , is based upon the current pixel value (small or large) identified in the Aux data packet for the current spin/sector and ET combination. The final CDF variable that is created to contain the intensities is a two-dimensional variable of type Double (or Double Precision) and sized as $FxDU[tele, enchan]$ so that it contains the data for each telescope and energy channel combination.

Ion Species Mode Flux Data (ISRHELT)

The calibration of the rate and flux data measurements for the Ion Species Rates High Energy Resolution Low Time Resolution (ISRHELT) data product is poorly understood and any science that utilizes this particular data product should at the very least do a relative comparison to the equivalent ECT-MagEIS ion flux observations before utilizing this data to make scientific conclusions.

RBSPICE Background Contamination

The current data files produced by the RBSPICE SOC are not background corrected for contamination. Work is ongoing within the RBSPICE team to correct for these issues but at the time of this writing the rates are still potentially contaminated with accidentals (mostly during perigee) and other background rate contamination issues. **The reader is strongly encouraged to reach out to members of the RBSPICE team prior to doing significant scientific activity in order to avoid utilization of contaminated data and**

deriving erroneous results. The two specific products that are most likely contaminated with background or accidentals are a varying set of the TOF_xPH proton lowest energy channels and all of the TOF_xPH oxygen channels. At some point, the RBSPICE SOC will reprocess the data and at that point when background rates dominate over foreground rates on a channel-by-channel basis then the channel specific data quality flags contained within the CDF files for each flux variable will be properly tagged with a value indicating data contamination. As of the writing of this manuscript the TOF_xPH oxygen data have all data records tagged as contaminated. Work is ongoing to attempt to eliminate the background from the data.

Level 3 Processing Algorithms

Processing Level 2 data into Level 3 data requires the calculation of the pitch angles of each telescope, using the measured magnetic field received from the EMFISIS instrument as well as loading of ancillary data from the ECT Magnetic Ephemeris data files.

EMFISIS Magnetic Field Data

EMFISIS Level 2 UVW magnetic field data files were used to calculate the RBSPICE pitch angles. These files contain data sampled at 60 Hz with over 5 million samples per data file. In order to reduce memory utilization and processing requirements, these files were deprecated by a specific programmable number prior to pitch angle calculations. The final mission wide deprecation factor was set to 8 representing a signal frequency of 7.5 Hz which results in approximately 2-3 magnetic field measurements per RBSPICE sector. No other filtering of the EMFISIS data was utilized during the deprecation stage.

ECT Magnetic Ephemeris Data

Additional fields loaded in the RBSPICE Level 3 CDF files were derived from ECT Magnetic Ephemeris data files. The definitive Olsen-Pfizer 1977 quiet time data were used as the source. Specific data fields used were deemed necessary and pertinent to provide for a full scientific understanding of the RBSPICE energetic particle data: L_{dipole} , L^* , L_{eq} , l (2nd adiabatic moment - single value and pitch angle dependent array), K (3rd adiabatic moment- single value and pitch angle dependent array), and Magnetic Local Time (MLT).

Calculation of Particle Flow Direction

The particle flow direction has been added to the RBSPICE Level 3 files since file version x.1.10. The calculation of particle flow direction, $\hat{v}_0, \dots, \hat{v}_5$ in Figure 13, uses the definitive SPICE CK, FK, and IK kernels for each spacecraft at the time of the observations. The calculation utilizes the NAIF SPICE function `pxform_c(f, t, tmatrix)`: $i = \{n \mid n \in \mathbb{N}, 0 \leq n \leq 5\}$. The variable f represents the “From” reference frame and is the RBSPICE telescope reference frame ($RBSP\{A/B\}_{RBSPICE_T_i}$), e.g. $RBSPB_{RBSPICE_T_3}$ represents RBSPICE telescope 3 of spacecraft B. The variable t represents the “To” reference frame and is the Spacecraft UVW reference frame. The RBSPICE telescope and spacecraft

RBSPICE Pitch Angle Calculation Diagram

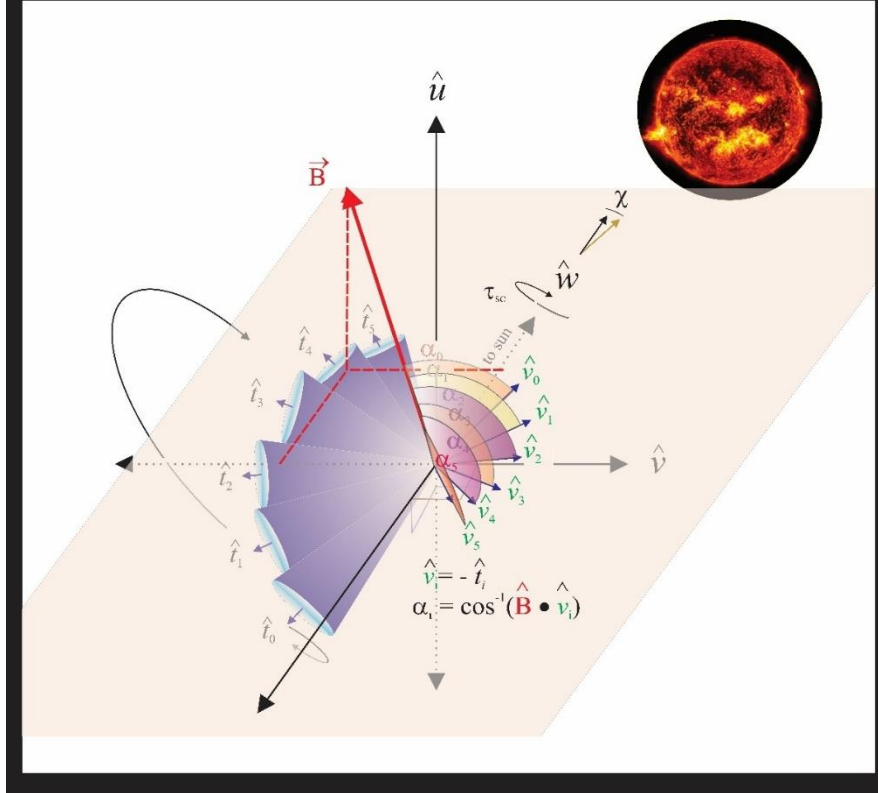


Figure 13 Geometry of the calculation of the RBSPICE Pitch Angles based upon the particle flow velocities for each telescope in the spacecraft UVW reference frame.

UVW reference frames are defined in the Van Allen Probes SPICE frame kernels: rbspa_vxxx.tf and rbspb_vxxx.tf where “xxx” is the highest version number.

The particle flow direction unit vector is then calculated as the negative or reverse of the telescope boresight unit vector transformed into the UVW reference frame, e.g., $\hat{v}_i = -\hat{T}_{iSM}$. Any exceptions occurring during this transformation results in the particle flow direction unit vector set as $\hat{v}_i = (0.0, 0.0, 0.0)$ representing an unknown direction.

Calculation of Pitch Angles

Figure 13 also displays the geometry used in the calculation of the RBSPICE pitch angle for each of the instruments six telescopes. The overall orientation of the diagram is such that the spacecraft \hat{w} -axis points generally toward the sun. The spacecraft rotation around the \hat{w} -axis is also shown and the fan of six RBSPICE telescopes allow for an almost 4π steradian view of the sky for each spacecraft spin period: $\tau_{sc} \cong 10.9 \text{ sec}$. The conical elements of the figure display the telescope look direction unit vectors, \hat{t}_i , centered on the aperture for each telescope as they are mounted on the spacecraft. The particle velocity unit vectors (or particle flow direction) are also shown in the diagram along with the representation of the pitch angles as the angle between the velocity unit vectors and the observed magnetic field unit vectors. The deprecated 7.5 Hz magnetic field signal results in approximately 2-3 magnetic field vectors occurring in the RBSPICE sector ($\sim 0.3 \text{ sec}$) time window.

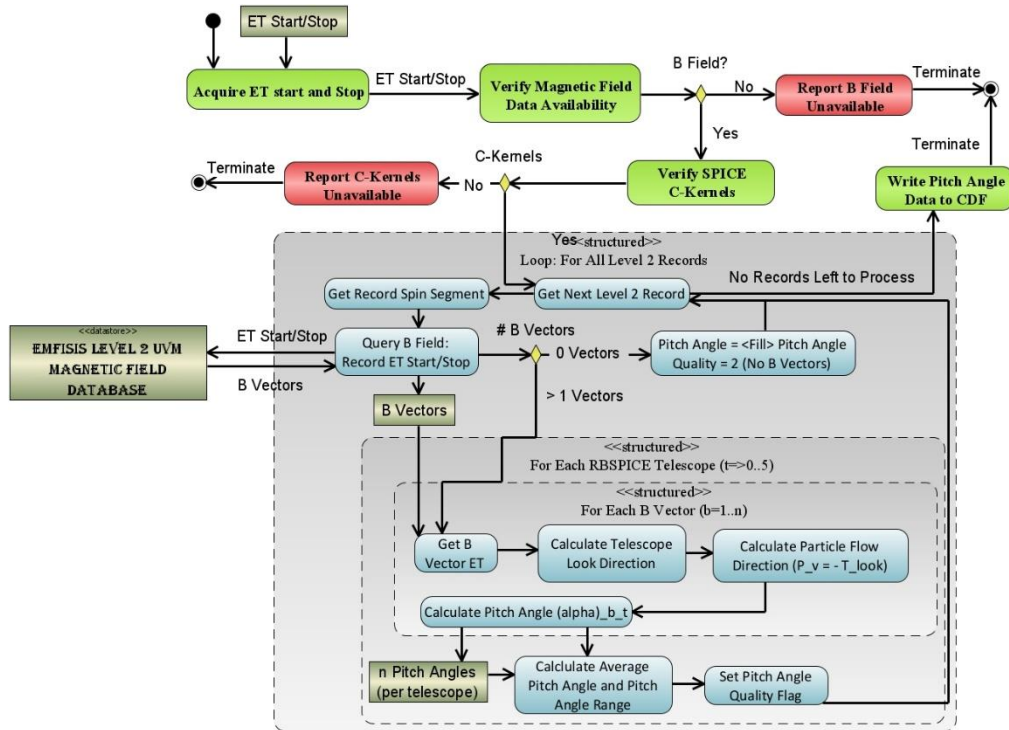


Figure 14 Algorithmic description of the calculation of the RBSPICE Pitch Angles

Algorithmically, a pitch angle is calculated for each of the magnetic vectors that exist within the accumulation period. The final pitch angle is the average of the calculated pitch angles and the deviation between all pitch angles is reported in the CDF variable $FxDU_AlphaRange$. If the deviation between the calculated pitch angles results in variations that are larger than $\frac{1}{2}$ of a sector look direction then the sector pitch angle quality flag is set to a value indicating it is unusable ($AlphaQuality_i = \{0\text{-Good}, 1\text{-Bad}\}$) and the pitch angle is set to the CDF Double Precision fill value of -1.0×10^{31} . Calculation of pitch angles uses the algorithm in Figure 14

Calculation of Phase Angles

The RBSPICE Level 3 data files, as of file version x.2.z, include a calculation of the phase angle of the RBSPICE telescope with respect to the Solar Magnetospheric (SM) reference frame (Laundal, 2017). Figure 15 displays the calculation of the phase angles in the SM reference frame. The magnetic field $\hat{x} - \hat{y}$ plane is first projected into the SM reference frame and then the phase angles are calculated with respect to the SM coordinate system using the projected vectors of $\vec{B}_{x_{SM}}$ and $\vec{B}_{y_{SM}}$. The orientation of this figure is such that the \hat{z} -axis of the SM frame is up (approximately in the direction of \hat{B}_{dipole}); the \hat{x} -axis is away from the Sun; and the \hat{y} -axis completes the orthogonal system. The RBSPICE phase calculation is defined such that the zero-degree phase angle points toward the Sun, i.e., along $+\hat{x}_{SM}$ and the 90-degree phase angle is in the $+\hat{y}_{SM}$ direction. As the spacecraft orbits around the Earth, this reference frame always maintains the relationship between the solar drivers of magnetospheric activity and the phase angle of the particle distribution. The figure also shows the particle velocity vectors and the associated acceptance solid angles for each RBSPICE telescope. The phase angles are calculated in

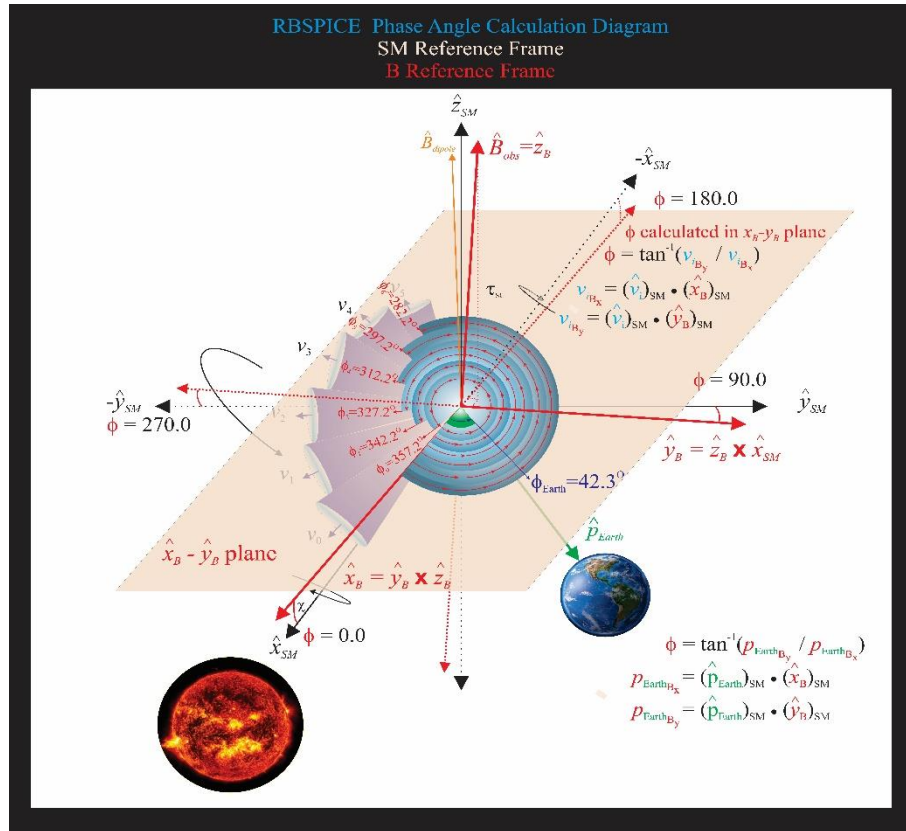


Figure 15 Diagram of the calculation of the phase angle in the SM reference frame. Note that to reduce the complexity of the diagram, the rotation of the spacecraft is shown around the \hat{x}_{SM} axis but the actual rotation of the spacecraft is around the \hat{w} axis of the spacecraft which points approximately along the \hat{x}_{SM} axis.

the XY_{SM} plane and are represented by the blue gradient circles with red lines/arrows starting at the \hat{x}_B -axis and going to the central point of each cone. An example phase angle is shown with $\phi_0 = 357.2^\circ$ and each subsequent phase angle ~ 15 degrees rotated away from the Sun. If the phase angle cannot be calculated then that phase angle is set to the CDF Double Precision fill value of -1.0×10^{31} . This figure also shows the calculation of the phase angle between the vector that points from the Earth toward the SC and the \hat{x}_B -axis in the XY_{SM} plane. This allows a phase shift calculation for scientific analysis of Earth centered radial, tangential, and normal particle flow/anisotropies. Figure 16 shows the algorithm used in the calculation of the RBSPICE phase angle.

Level 3 Pitch Angle and Pressure (PAP) Processing Algorithms

Level 3 differential flux data is used in the calculation of the Level 3 PAP data products by utilizing the pitch angle data from each telescope and a predefined set of pitch angle bins with centers at 7.5, 20, 30, 40, 50, 60, 70, 80, 90, 100, 110, 120, 130, 140, 150, 160, and 172.5 degrees. Part of the binning of the differential flux provides the ability to calculate partial moments of the distributions. The calculated species-specific moments include the perpendicular and parallel partial particle pressures, density for a select set of energy channels, the omnidirectional differential flux for each energy channel, and fully integrated particle flux over the entire energy range (**Note: proceed with caution as this integrated particle flux includes noisy and background contaminated channels**).

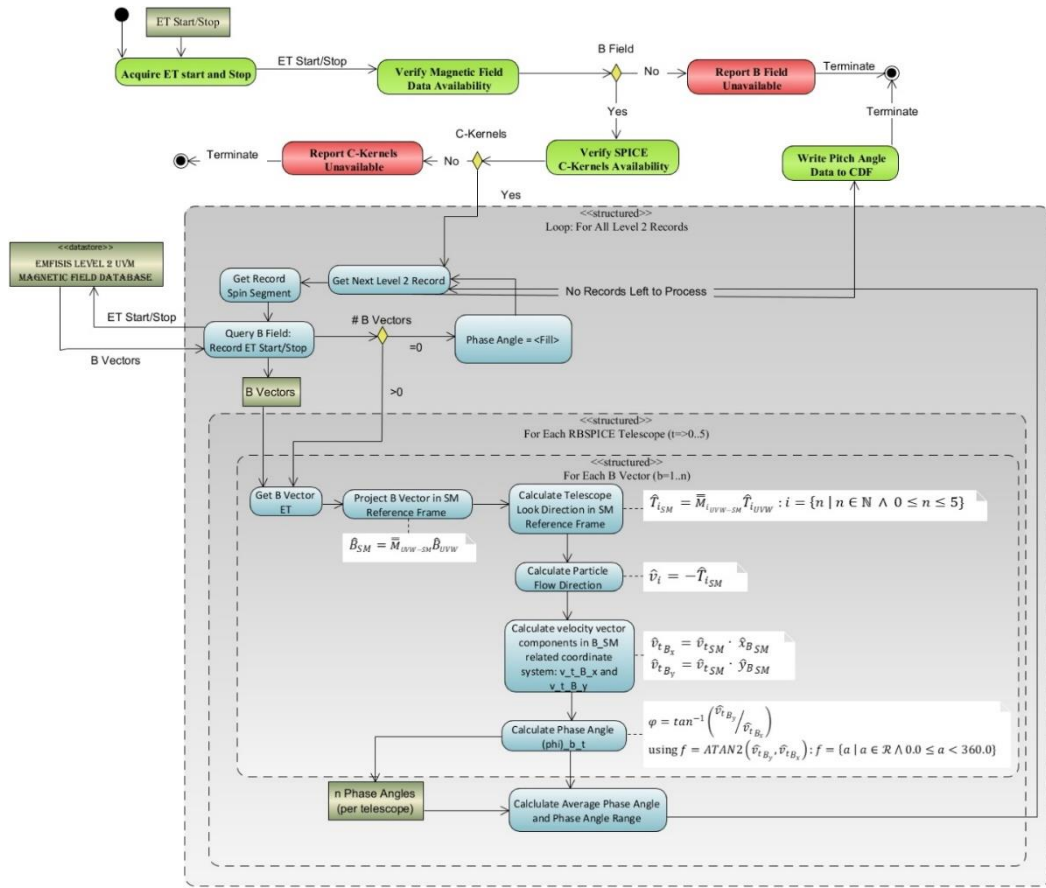


Figure 16 Algorithmic description of the calculation of the RBSPICE Phase Angles.

Binning of Pitch Angles and calculation of aggregate data

PAP data calculation uses the algorithm shown in Figure 17. Calculation of the moments is over a specific set of energy channels for which the RBSPICE science team has determined are reasonably reliable. Table 5 presents the energy channels used in moment calculation as a function of data product, energy channel indices (absolute and relative reference channel range with respect to the Level 3 CDF differential flux variable), and the energy channel passband range. Products that are set “none” do not have moments calculated since the specific product has been identified by the RBSPICE team as untrustworthy either in data or in calibration. Untrustworthy data products also have data quality flags set to a value other than 0=good or 10=unknown indicating that the data should not be used for science.

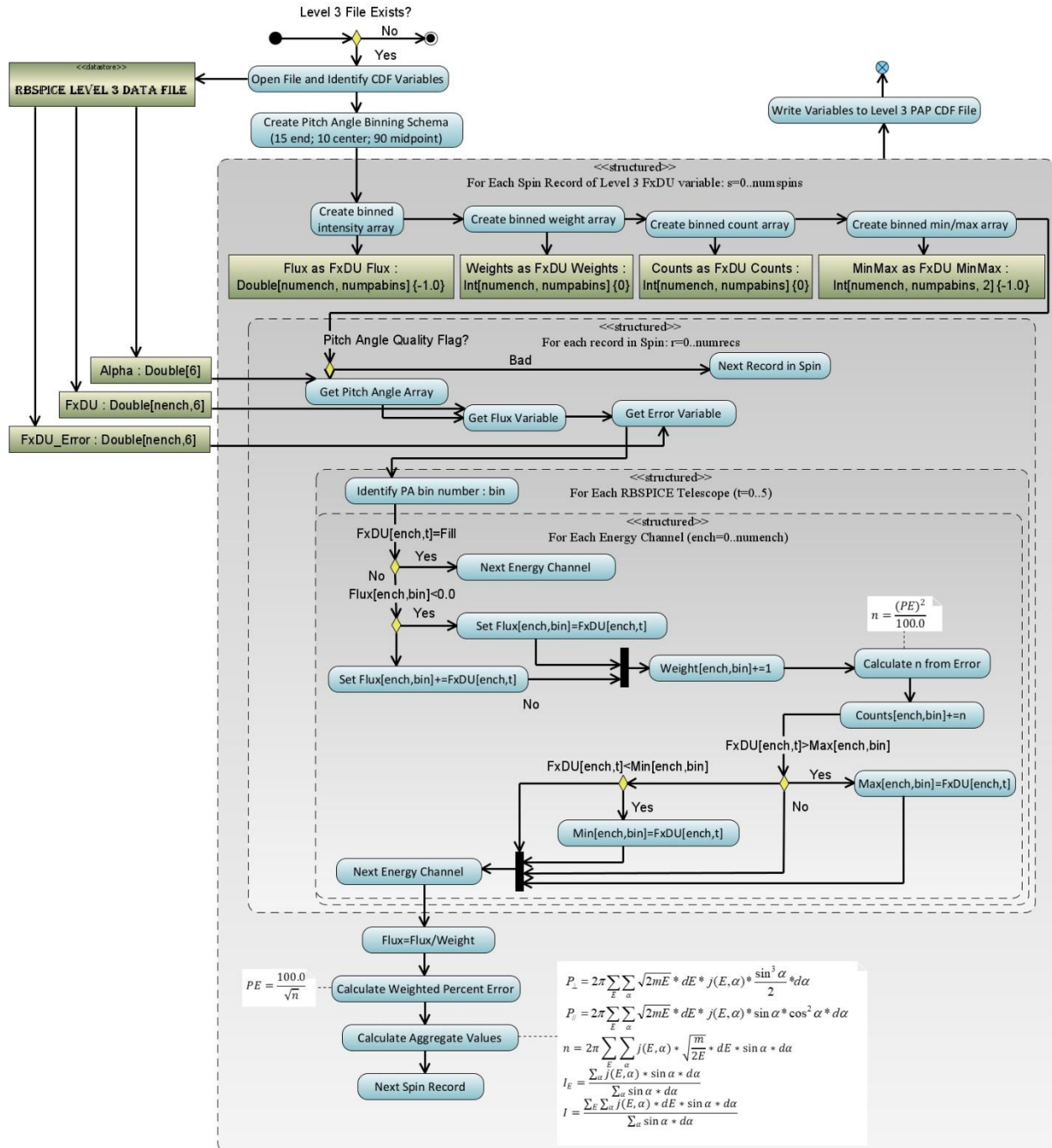


Figure 17 Algorithm for the binning of RBSPICE differential flux and the calculation of moments for the L3 PAP products. With minor modifications this is the same algorithm used in the binning of RBSPICE differential flux and the calculation of moments for the L3 PAPAP products.

Special note: As of the writing of this paper the TOFXPH Oxygen observations are deemed unreliable and no aggregate values are calculated within the PAP data files but the data is provided as a product so that the RBSPICE team can update the calibration information and reprocess the data once the causes of the contamination are understood and can be removed resulting in newly calibrated data considered usable for science.

Table 5 Table showing the specific energy channels used in the calculation of the aggregation (moment) data. Each product shows the absolute channel reference with respect to the Level 3 source data array, the relative channel reference with respect to the energy channels for the specific data product, the mid-point calculated energy passband as well as the full energy passband using the [low, high] values for each passband. Finally, the table shows the mass used in the moment calculation.

Product	Energy Channels (absolute index)	Energy Channels (relative index)	Energy Range (KeV) (Midpoint Passband)	Delta E (KeV)	Energy Range (KeV) (Low-High passbands)	Delta E (KeV)	Species used for mass calculation
ESRHELT	3–63	3–63	24.1–938.7	914.6	23.38–974.39	951.11	e
ESRLEHT	1–13	1–13	27.4–425.8	398.4	24.7–527.0	502.3	e
TOFxE_H	1–13	1–13	54.7–597.6	542.9	49.0–657.6	608.6	p
TOFxE_He (Pre)	0–8	0–8	65.0–518	453	56.8–584.5	527.7	He
TOFxE_He (Post)	0–10	0–10	65.0–870	805	56.8–982.0	925.2	He
TOFxE_O (Pre)	9–17	0–8	142–1127	985	123.8–1256.0	1132.2	O
TOFxE_O (Post)	11–18	0–7	142–870	728	123.8–998.5	874.7	O
TOFxE_Ion	2–63	2–63	50.6–18525.2	18475	48.4–20000	19952	Ions (~1.0 AMU)
TOFxPH_H_LEHT	3–8	0–5	17.4–50.0	32.6	28–100	72	P
TOFxPH_H_HELT	18–30	7–19	14.8–48.9	34.1	14.1–51.4	37.3	P
TOFxPH_O_LEHT	none	none	NA	NA	NA	NA	O
TOFxPH_O_HELT	none	none	NA	NA	NA	NA	O

Level 3 Pitch Angle, Phase Angle, and Pressure (PAPAP) Processing Algorithms

Level 3 differential flux data is used in the calculation of the Level 3 PAPAP data products by utilizing the pitch angle data from each telescope and a predefined set of pitch angle bins with centers the same as for the Level 3 PAP data product. The predefined set of phase angle bins are calculated in thirty (30) degrees separation with the first center set at zero degrees. Moments are also calculated as with the Level 3 PAP data product and include calculated species specific perpendicular and parallel partial particle pressures, density for a select set of energy channels, the omnidirectional differential flux for each energy channel, and fully integrated particle flux over the entire energy range. An algorithm diagram is not shown for this product as it is almost exactly the same as for the Level 3 PAP algorithm with one change. At the point in which we identify the “PA Bin” number for the record we instead identify the PitchBin and the PhaseBin for the record. The FxDU related variables are expanded with one additional dimension, e.g. FxDU as Double[#energy channels, #Pitch bins, #Phase bins].

Level 4 Phase Space Density Data Products

As of the writing of this paper, the RBSPICE science team is contemplating the creation of a standard Level 4 Phase Space Density data product for the proton, helium, and oxygen species separately. The development of this data product is strongly dependent upon available Phase F funding and resources and/or the availability of additional funding to support this activity. The following paragraph describes the primary considerations required for the development of such a product in the light that the RBSPICE team cannot produce the product and others desire to do this development.

More to come on the RBSPICE Level 4 PSD data product algorithms and constraints. JWM

Section 2 – Science Coordination Activities

One of the key elements of the Van Allen Probes Mission was the intentional attempt to have the instrument teams coordinate science activities both within the mission specific group of instrument teams but also to include external teams such as the team from the Balloon Array for Radiation-belt Relativistic Electron Loss (BARREL) Mission and to also include other assets such as ground radar stations. The most important coordination activities between the instrument teams involved the cross calibration of similar instruments e.g., overlap of proton energy channels between ECT-HOPE and RBSPICE/TOF_xPH. The following section describes some of the key coordination activities and results that have been accomplished to this point during the Van Allen Probes Mission.

Electric and Magnetic Field Instrument Suite and Integrated Science (EMFISIS)

Over the course of the Van Allen Probes mission, EMFISIS conducted various science coordination activities. First and foremost, because magnetometer data is essential for calculating particle pitch angles and field-aligned coordinates for fields data, EMFISIS coordinate with all teams to provide good accuracy magnetic field data in spacecraft coordinates.

Other coordination efforts included:

- Working with the BARREL balloon team to coordinate burst mode data taking at times when the Van Allen Probes spacecraft were magnetically conjugate to regions in which the BARREL balloons were flying. This is described in full detail in the EFW section which follows.
- Coordinating with lightning research ins the US and Hungary to take burst data when over regions where they had good ground measurements and the Van Allen probes were magnetically conjugate to those regions This enabled more detailed studies of lightning-generated whistlers.
- Coordinating with researchers at Goddard Space Flight Center to take burst mode data when the Van Allen probes were at perigee in regions where spread-F is observed. This resulted in some highly detailed observation of spread-F including some unusual observations of a magnetic signatures associated with these waves
- EMFISIS coordinated efforts to identify times when the Van Allen probes and the Japanese Arase satellite had conjunctions in order to take burst mode data for cross comparisons between the two missions. This has led to several papers on conjugate observations.

In addition to these efforts. EMFISIS did its best to take burst mode data or implement different modes of operation on requests for short periods of time.

Electric Field and Waves Suite (EFW)

Sub-Section 1

During the Van Allen Probes mission the Electric Fields and Waves (EFW) instrument took part in a number of collaborative science campaigns with other missions including BARREL, FIREBIRD/Ac6, WWLLN, etc. These collaborations were focused efforts to collect high time resolution burst waveform data, generally during times of magnetic or drift shell conjunctions. By mission's end, these efforts had provided valuable science and built-up substantial datasets of spatially separated, high time resolution data during dynamic times.

EFW, chiefly among the RBSP instruments, was most suited to burst campaigns due to its novel and unprecedented 30 GB burst waveform solid state memory. This ground-commanded memory (henceforth burst 1) complemented the onboard-triggered 4 MB burst 2-memory based on *heritage* design. The large memory capacity allowed continuous collection over durations of hours of full 3d electric and magnetic field waveform data at sample rates up to 16 kHz. This duration is a significant fraction of the RBSP orbit and the duration of a storm or substorm. This capability fundamentally redefined the nature of collaborative efforts, expanding the spatial/temporal sphere of influence of RBSP well beyond the two-point measurements of the two probes. This approach is part of a recent paradigm of combining big budget with small budget missions (see Spence, Millan chapters), allowing a cost-effective approach to addressing certain science questions that require (or are enhanced by) distributed multipoint measurements.

For details on the EFW instrument, as well as these collaborative efforts see the EFW instrument paper in this book, as well as Section 5 of this chapter. In this section we discuss details of a few of these campaigns, starting with collaborations with BARREL in 2013 and 2014. Lessons learned from these campaigns (see Section 5 of this chapter) set the stage for huge operational efficiency improvements of subsequent burst 1 operation.

Sub-Section 2: Details of certain campaigns

EFW's first significant collaborative effort was with the Balloon Array for Relativistic Radiation Belt Losses (BARREL) mission of opportunity's first mission in 2013 (Millan et. al, 2021 this volume; Woodger et. al, 2015). During this roughly two-month long effort the BARREL team launched a total of 20 balloons from SANAE and Halley Bay stations in Antarctica. Balloons had an average duration aloft of approximately 12 days, and typically 6 balloons were aloft at any given time (Woodger et. al, 2015). At altitudes of ~30-40 km the balloons measured Bremsstrahlung X-rays created from external sources including electron precipitation from the radiation belts in addition to galactic cosmic rays, solar flares, solar energetic protons. Using a forward folding technique the X-ray spectrum could be reliably used to estimate the spectrum of the incoming flux, particularly when constrained by in situ flux measurements from satellites (See Millan et. al, 2021 this volume; Woodger et. al, 2015 for more details). These measurements filled a gap in the near-equatorial Van Allen Probes observations by allowing a direct measurement of precipitating flux – not typically possible for near-equatorial satellites which cannot resolve the small (~1-2 deg) loss cone.

One of the key science goals of BARREL was to quantitatively investigate wave-particle interactions leading electron precipitation by various wave types and other precipitation drivers at times of magnetic or drift shell conjunction. In 2013(2014) conjunctions were focused in the morning(afternoon) sector, as shown in Figure 18 (derived from Figure 1 in Woodger et. al, 2015). This location played an important role in the EFW burst 1 operation, with morning sector conjunctions typically sampled at the highest rate (16K) in order to resolve chorus waves, and with lower rates for the afternoon sector to resolve lower frequency hiss and EMIC waves.

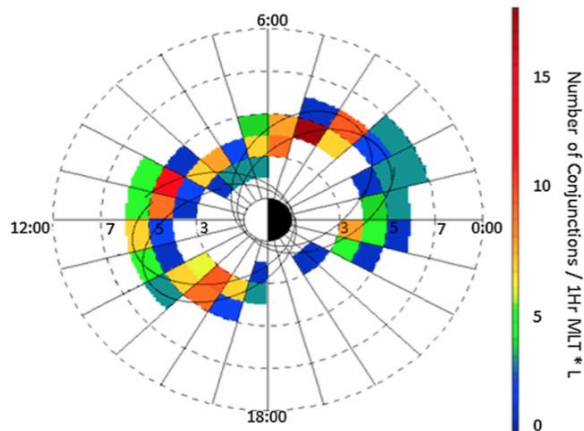


Figure 18 Woodger15 all BARREL/VAP conjunctions 2013-2014

The EFW/BARREL collaboration was highly successful for both missions; planning and communication between the teams was a key component to this success. An approximate three-day lead time was needed to decide on when burst data were to be collected to ensure the commands would be successful uplinked to the satellites. Shorter timeframes were sometimes available for us to make decisions, however we tried to stick to making decisions about burst collection 3 days out. Thus, it was clear that we would need a clear method to plan and prioritize collection periods.

The relevant teams met informally at AGU a year prior to the first BARREL campaign to discuss strategy. A plan was developed for the BARREL team to create expected trajectories as Google Earth KML files to enable prediction of conjunctions between the balloons and satellites. These plots, which included the balloon flight paths and the magnetic footprint of the Van Allen Probes, ground stations, and other satellites, were then referenced when prioritizing burst collection and download.

Starting in mid-December 2012, when the team declared flight-ready in Antarctica, the BARREL team started sending daily emails that included a high-level summary of the space weather and any potential upcoming activity, followed by updates about which balloons were likely to be launched or terminated, as well as which were still afloat. A list of observed precipitation events followed, along with the current burst data collection times and data in the queue to be downloaded. These two pieces of information facilitated discussions between the teams to prioritize downloading data which was likely to be highly impactful. The emails continued with updates from other instruments, missions, and ground observations, along with a more detailed look at the current space environment and predictions of upcoming activity. As these emails were long, they were often ended with a fun fact. This may seem unnecessary to mention or add, but it aided in keeping spirits light which helped with a near 24/7 cadence over a few months.

After the daily emails were sent, the BARREL, EFW, and other instrument and mission teams held a daily phone call to tag up and plan for new burst data collection and downloads. Because we made sure that the emails described above were sent about 2 hours prior to the phone call, our chats were very focused and short. Even with waiting a few minutes at the beginning to make sure everyone was on, say hi, how's the weather, etc. the average length of time for these telecons was 6 minutes. Telecons were cancelled when not needed and the team worked hard to avoid weekend tag ups to give people some much deserved and needed down time.

As many researchers were interested in the ongoings of the BARREL campaigns but did not want to receive daily emails, we offered a few other forms of communication. The emails were paired down to remove the identification of event times and other potentially sensitive information and then posted to a blog <http://relativisticballoons.blogspot.com/>. In the later campaigns this blog was used for public outreach and we added a second science focused blog for researchers. We also started posting when we were launching and terminating balloons, along with some other fun information to a twitter account @keV_Balloons, and on to a Facebook page. These interactions provided unexpected engagement with the broader research community. Specifically, the Twitter interactions with other space physics researchers led to the collection of extra ground data and resulted in successful proposals to get time on EISCAT (which was near conjugate to the Kiruna launch site) for the 3rd and 4th BARREL campaigns.

Through advance planning, respecting people's time, and accommodating their preferred communication format, we were able to have a successful first campaign. This success led everyone to work extra hard, and even look forward to a second and additional intense follow-on campaigns.

Another aspect which enabled the success of BARREL as a mission of opportunity was the openness of the Van Allen Probes Team to include BARREL in other activities. The BARREL team regularly had joint meetings with the EFW and other teams and were always included in the twice-yearly mission meetings. Perhaps most importantly, The BARREL team was included in their efforts for outreach to the broader scientific community. This included the Van Allen Probes Data/Analysis help sessions during posters at AGU and GEM as well as inclusion within chapters such as this one. This was further enabled by the BARREL team ensuring their data was available through CDAWEB and analysis software provided through SPEDAS (Angelopoulos et. al, 2019)

Energetic Particle, Composition, and Thermal Plasma Suite (ECT) Cross Calibration with Radiation Belt Storm Probes Ion Composition Experiment (RBSPICE)

The RBSPICE and ECT teams have worked on cross calibration of the species-specific observations between the ECT/HOPE, ECT/MagEIS, and the RBSPICE instrument observations for similar energy channels. These calibration activities resulted in adjustments to the efficiencies in the calibration table for the RBSPICE instrument with additional work still ongoing. One of the key cross calibration activities has been to resolve an apparent discrepancy between the upper energy channels of the HOPE and the lower energy channels of the RBSPICE proton differential flux measurements. As of the writing of this manuscript there is an approximate factor of 2 difference between the HOPE and RBSPICE proton data for the HOPE release 4 data set. Upon analysis, the problem is significantly more complex than a simple multiplicative factor although there is an expectation that some of this discrepancy will be resolved in the upcoming release 5 dataset. For example, the left panel of Figure 19 shows two combined proton spectra using OMNI data from HOPE (red), RBSPICE/TOF_xPH (blue), and RBSPICE/TOF_xE (green). Error bars reflect the width of each energy channel (\hat{x} -axis) and the Poisson counting errors (\hat{y} -axis). There is a clear mismatch between the HOPE OMNI differential flux higher energy channel measurements and the RBSPICE/TOF_xPH measurements well outside the range of the error bars. In contrast, the TOF_xPH and TOF_xE measurements form a continuous spectrum within the limitations of the errors.

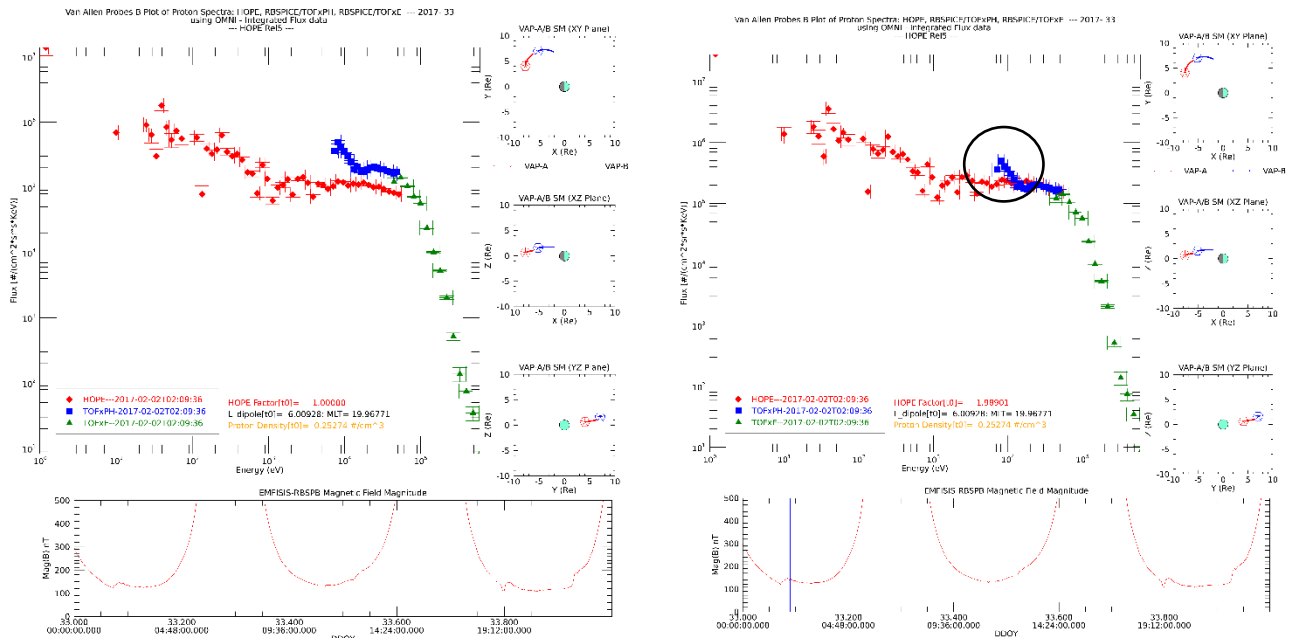


Figure 19 Comparison of ECT/HOPE, RBSPICE/TOF_xPH, and RBSPICE/TOF_xE spectra at 2017-02-02T02:09:36 UTC using the OMNI data variables from each data product. The left panel shows the raw spectra from each instruments data product with HOPE in red, TOF_xPH in blue, and TOF_xE in green. There is a clear discrepancy between the RBSPICE TOF_xPH/TOF_xE OMNI differential flux and that of HOPE. The right panel shows the same data except that the HOPE data has been increased by a factor of ~ 1.98 referenced in the figure as the HOPEMOD factor which is used to shift the measurements such that they now form a continuous spectra excluding the lowest TOF_xPH energy channels. The black circled TOF_xPH energy channels lifted above the merger of the HOPE and TOF_xPH/TOF_xE spectra are due to lower energy oxygen ions in the TOF_xPH system being interpreted as protons. The specific HOPEMOD factor used was calculated using a simple algorithm as described in this section.

In the right panel, a simplistic algorithm has been used to match the HOPE upper energy observations with those of the RBSPICE/TOFxpH observations of similar energy. This figure includes a printout line HOPEMOD Factor (t0) which identifies the scalar multiplicative factor used to change the HOPE flux to match that of the RBSPICE/TOFxpH flux for the time 0 observation. In this particular example, the calculation itself is only accurate for the upper energy channels of the HOPE data. This is in part because the lower energy channels of the RBSPICE/TOFxpH data for the observation time is contaminated with accidentals causing the lifting of the TOFxpH spectra (black circled area). For this particular time, the required factor needed to modify the HOPE flux is ~ 1.98 . The algorithm used is described in the following steps:

- 1) $\langle j_{HOPE} \rangle = \frac{\sum_{i=68}^{70} E_i}{3} : E_{range} = [30.3 \text{ KeV} - 47.8 \text{ KeV}] \Delta E = 17.5 \text{ KeV}$
 $E_{68} = 32.7 \pm 2.5 \text{ KeV}$
 $E_{69} = 38.1 \pm 2.8 \text{ KeV}$
 $E_{70} = 44.4 \pm 2.5 \text{ KeV}$
- 2) $\langle j_{RBSPICE_{TOFxpH}} \rangle = \frac{\sum_{i=15}^{18} E_i}{4} : E_{range} = [31.2 \text{ KeV} - 46.5 \text{ KeV}] \Delta E = 15.3 \text{ KeV}$
 $E_{15} = 32.9 \pm 3.3 \text{ KeV}$
 $E_{16} = 36.3 \pm 3.6 \text{ KeV}$
 $E_{17} = 40.1 \pm 3.9 \text{ KeV}$
 $E_{18} = 44.3 \pm 4.4 \text{ KeV}$
- 3) $R = \frac{\langle j_{RBSPICE_{tofxpH}} \rangle}{\langle j_{HOPE} \rangle}$
 (Note: R is referenced as the HOPEMOD factor or just HOPEMOD in some of the plots)
- 4) $j_{HOPE_{ch}} = R * j_{HOPE_{ch}}$

This particular algorithm provides a 0th order of calibration between the HOPE and RBSPICE instruments spin-by-spin. There are significantly more complex aspects of this calibration problem that includes positionally where the spacecraft is within the orbit by both L and MLT as well as the ongoing level of magnetospheric activity as Sym-H (or Dst) and whether the spacecraft is within the plasmasphere or outside the plasmasphere.

Figure 20 shows the distribution of the values of $R_{HOPEMOD}$ for the entire mission for both spacecraft (A-left, B-right). In the plots, the black curve displays the distribution for the entire mission for all values of $R_{HOPEMOD}$ within the cutoff limits: $R_{range} = [0.01, 100.0]$ and $L_{Dipole} = [3.0R_E, 7.0R_E]$. The rest of the curves show the distributions of $R_{HOPEMOD}$ of L_{Dipole} between $3.0R_E$ and $7.0R_E$ in $0.5R_E$ increments. Each inset plot displays the location of the peak for each curve with errors calculated based upon the width of the individual peaks.

Figure 21 displays these peak measured values for the entire mission for both spacecraft (A-left, B-right) as a function of L_{Dipole} for different times throughout the mission. The time segments each represent one quarter of a precession of the petals of the Van Allen Probes orbits throughout the mission. Each time segment is centered on one of the primary MLT points of **Midnight**, **dusk**, **noon**, or **dawn** in order of precession periods over the 7-year mission. There are RBSPICE HV gain adjustments in 2013 and 2015

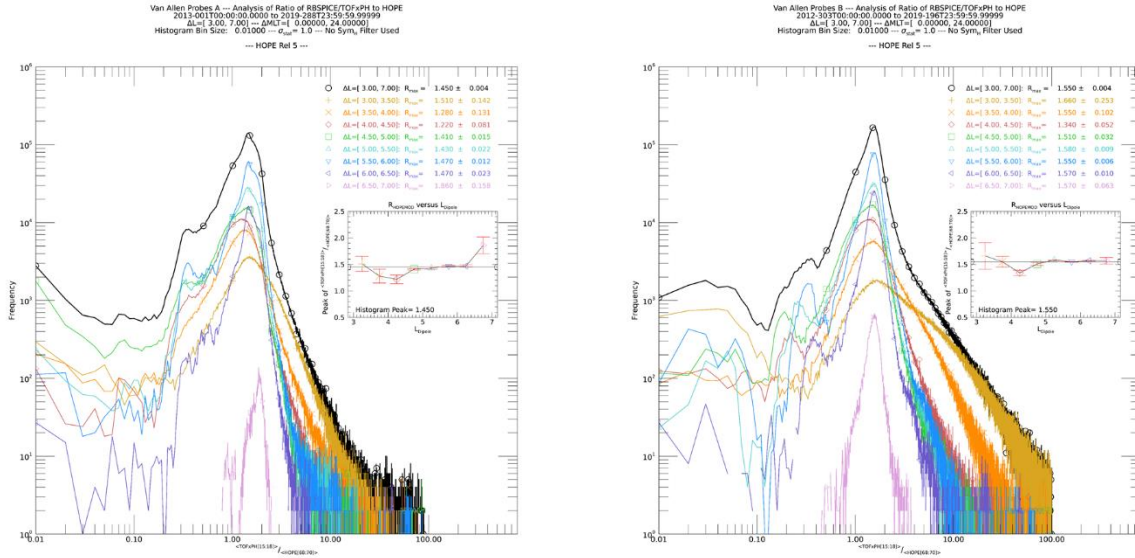


Figure 20 Distribution of the correction factor, $R_{HOPEMOD}$, for each spacecraft (A-left, B-right) accumulated over the entire mission. Each black curve includes all data and the rest of the curves provide the breakout by L_{Dipole} segments between 3.0 and 7.0 in $0.5 R_E$ increments. The consistency across L_{Dipole} is reflective of the significant work to cross calibrate the ECT-HOPE and RBSPICE observations throughout the mission.

where the ratio of HOPE to RBSPICE/TOFxpH flux observations remains fairly constant for those years but starts to drift downward thereafter.

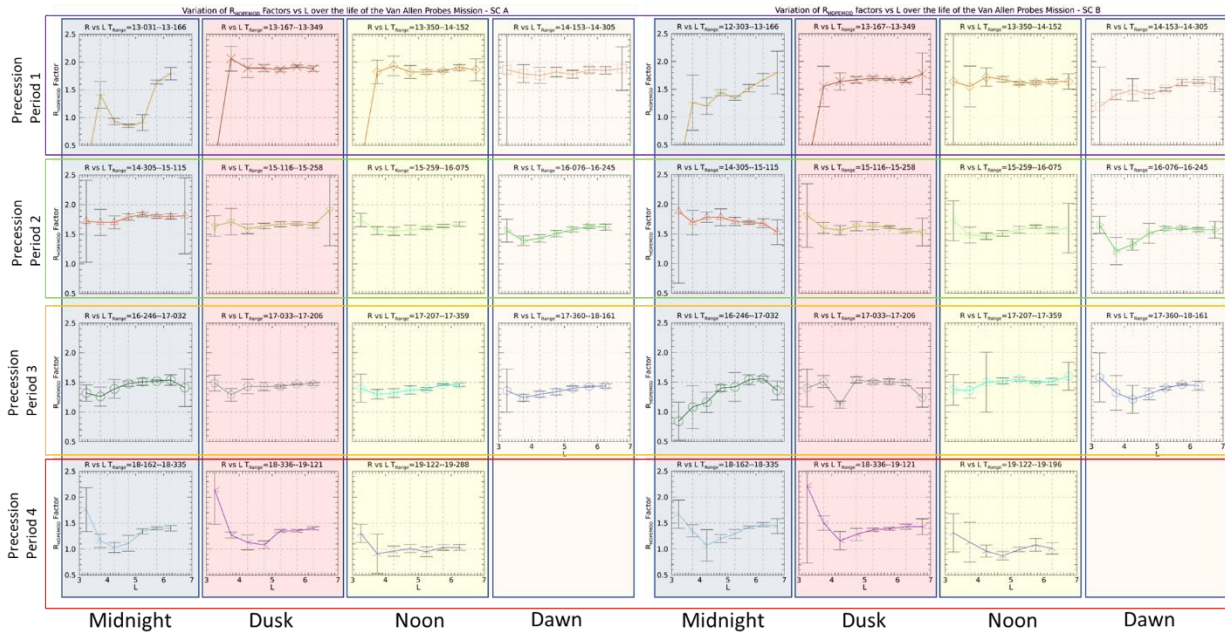


Figure 21 Plot of the L_{Dipole} dependency of $R_{HOPEMOD}$ for different periods throughout the mission. The dependency on L_{Dipole} is fairly constant throughout the mission except for 1) the initial quarter period (2013-031 through 2013-166) where both instruments are adjusting HV gain to stabilize rates and 2) the final precession period (or so) where the RBSPICE instrument performance has degraded especially for $L < 5$.

Figure 22 displays the peak measured value of R for different times within the mission (A-top, B-bottom). These curves more clearly show that there is a drift in the $R_{HOPEMOD}$ value which is indicative of deprecation of each of the RBSPICE detectors. Each curve shows a constant value of $R_{HOPEMOD}$ until the final calibration changes in 2015 and thereafter the value degrades. The remaining details of the calibration story of HOPE and RBSPICE proton observations are presented in the paper by Mouikis and Manweiler, (2021, this volume).

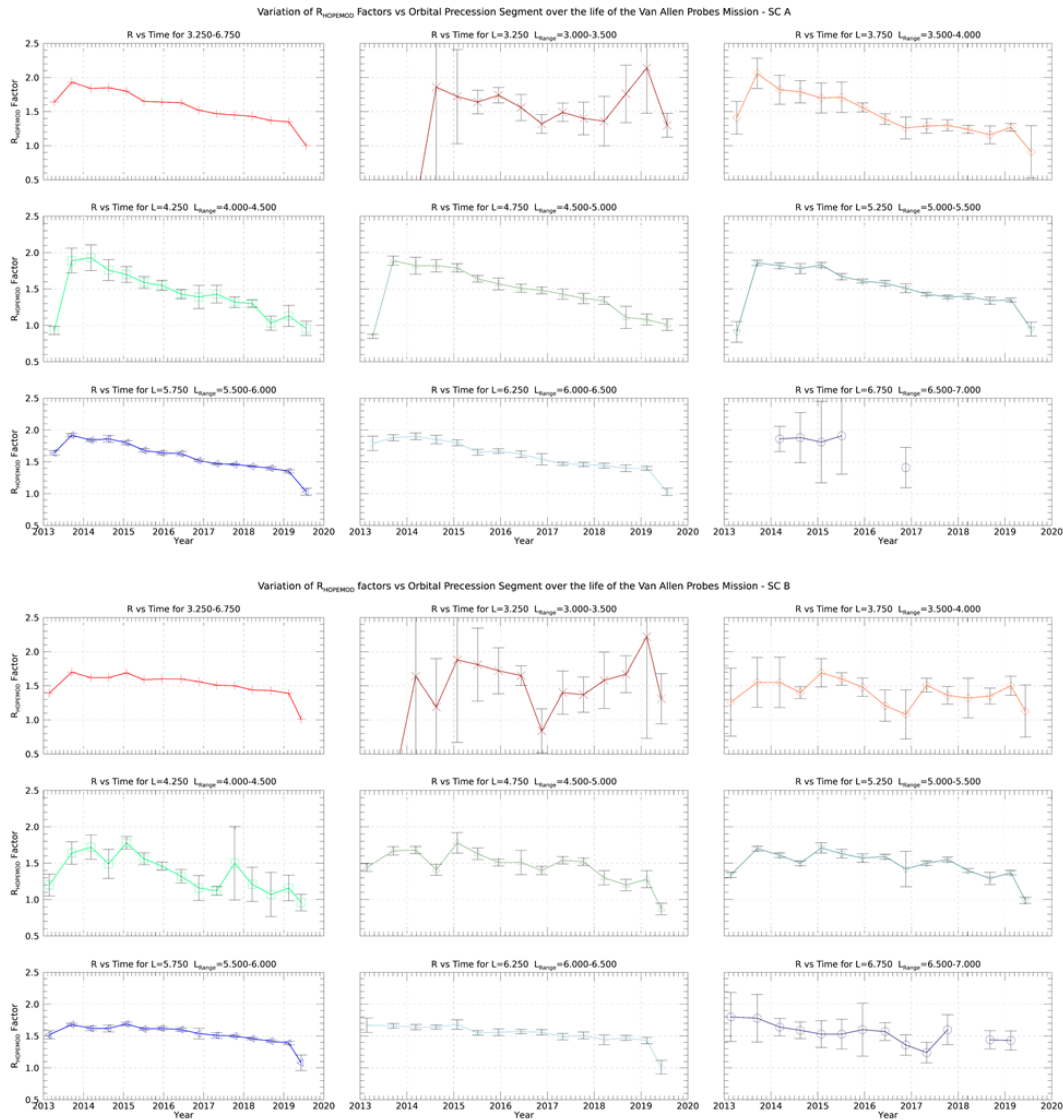


Figure 22 Plot of the $R_{HOPEMOD}$ for SC-A (top) and SC-B (bottom) for individual segments of L_{Dipole} as a function of Mission time. After the last RBSPICE calibration adjustment in January 2015 there is a slow degradation of the RBSPICE instrument that is captured very clearly in these plots comparing the RBSPICE and HOPE proton flux over time.

Section 3 – Science Analysis Software

Each of the Van Allen Probes Science Operations Centers (SOCs) used existing software or designed and programmed new software to provide a graphical view of the key indicators of instrument performance. The programs used were highly specific to the instruments with fully understanding of instrument variables and parameters allowing the engineering and science teams the capability of fine-tuning instrument performance throughout the mission. The sections below provide details on the software programs used by each of the instrument teams.

Electric and Magnetic Field Instrument Suite and Integrated Science (EMFISIS) and Energetic Particle, Composition, and Thermal Plasma Suite (ECT)

While EMFISIS employed substantial analysis software to generate the L4 WNA products, the software itself was not released to the public. That being said, EMFISIS was one of the primary sponsors of the development of the Autoplot analysis and display tool developed by Jeremy Faden ([Faden et al. 2010](#)). This is a free data analysis tool written in Java which allows it run on virtually any OS with Java support. Quoting the Autoplot website ([Autoplot.org](#)): “Autoplot is an interactive browser for data on the web; give it a URL or the name of a file on your computer and it tries to create a sensible plot of the contents in the file. Autoplot was developed to allow quick and interactive browsing of data and metadata files that are often encountered on the web. For more information, see [Faden et al. 2010](#) and the introductory [PowerPoint](#) slides.”

This tool was originally developed for use by the NASA virtual observatories (VxO's) but has since been adopted by both the ECT and EMFISIS teams as their primary data tool for working with the various measurements made on the Van Allen Probes. Some of the features of the software that were critical to both instrument teams are:

- Reads multiple ASCII formats including [Complex ASCII tables](#); [Binary tables](#); [Common Data Format \(CDF\)](#); [NcML](#); [SPASE](#); [Cluster Exchange Format](#); [NetCDF](#); [OpenDAP](#); [HDF5](#); [TSDS](#); [FITS](#); [Excel](#); [Wav](#); [PNG, JPG, etc.](#)
- Data is located with compact URI addresses. These contain the location of the data and additional information needed to use it.
- Special support for [CDAWeb server](#) at NASA/Goddard, [HAPI](#), and other data servers.
- [Das2](#) library used to create interactive graphics with slicing and custom interactions.
- Wildcards can be used to [aggregate](#) (combine) data from multiple files into one time series.
- Long time series may be rendered as a sequence of images as a ["pngwalk"](#) and viewed as a Cover Flow, table of thumbnails, or on a time line.
- Any displayed data may be saved to disk in ASCII, [Common Data Format \(CDF\)](#), and other formats, or plotted as PNG, PDF, or SVG.
- GUI State may be saved as an XML [".vap"](#) file and restored.
- Software may be run client side or server side.
- Data access layer for file reading may be used in [MATLAB](#), [IDL](#), or [SciPy](#) (via Java bridge), providing a common interface regardless of data source.
- Scripting via Jython, to control the application and read in data using metadata-aware datasets.
- [Open-source](#) (GPL with classpath exception) and may be used

This tool has turned out have enormous value and continues to be used widely by the science community both for Van Allen probes data as well as for other missions.

Electric Fields and Waves Suite (EFW)

EFW SOC software contributions are divided as follows:

- -SOC software for internal usage
- -SPEDAS routines

Note that burst memory management code written for the collaborative campaigns is discussed in the EFW instrument paper.

During the lead up to launch, as well as throughout the mission and post mission, the EFW team has written software as part of the IDL SPEDAS software package (Angeloupolos, 2019) intended for data access, calibration, and analysis (currently only bleeding-edge release). Routines are reliant on other code in the SPEDAS package, spike kernels from the CSPICE package, NASA's CDF file library, and magnetic field mapping routines in the IDL Geopack package. Installation instructions for these packages can be found at the respective websites.

EFW SPEDAS routines are found in the subfolder `/general/missions/rbsp/efw/` and can be divided into the following general categories:

- Routines that load EFW data to produce a certain data product
- Files/routines that contain data used for calibration.
- Crib sheets, examples

A more detailed explanation of these routines:

These routines can be generally divided into two types. The first type is the "from scratch" routines, written early on to load L1 data, and from these provided simple calibrations of the data. The second are the ones that load more refined calibrated data such as L2, L3, and L4. The second type should generally be used as they represent the best "general" calibrations for various data products, and are typically much faster to run. These also include code that was used to produce the official CDF files.

These routines are not intended to be called in isolation. Examples include a file with the boom deploy lengths vs time, a routine that grabs eclipse times, etc.

These are contained in the "examples" folder and are intended to let users know how to easily load and manipulate EFW data products.

Radiation Belt Storm Probes Ion Composition Experiment (RBSPICE)

Mission Independent Data Layer – RBSPICE

Short writeup on MIDL for RBSPICE (Larry Brown)

Section 4 – The Van Allen Probes Science Gateway

Introduction

The primary goal of the Van Allen Probes mission was to “Quantify the processes governing the Earth’s radiation belt and ring current environment as the solar cycle transitions from solar maximum through the declining phase.” The mission consists in a set of several instruments that collect different types of scientific data used to characterize the Earth’s magnetosphere. The Van Allen Probes mission architecture has no centralized Science Operation Center (SOC). Instead, individual instrument suites maintain their own SOCs and serve science data from those SOCs. This approach has the great advantage of leaving the responsibility of processing and delivering the data in the hands of the instrument teams who have the necessary scientific expertise. On the other hand, there is the disadvantage that the mission lacks of a centralized data center which the scientific community can access all the mission desired data in a single place. To address this shortcoming, the Van Allen Probes mission developed the concept of a “Science Gateway”, which is a web site focused on the science investigation and provides a single point of entry for each instrument SOC. The site, as will be illustrated below, provides access to:

- plot and retrieve scientific data, including Space Weather data
- planning tools, e.g., Multi-Mission Orbit Plotter
- ancillary data, e.g., Ephemerides
- Van Allen Probes related bibliography

The Gateway was developed using “Drupal”, an open-source content management system (<http://drupal.org>). The usage of Drupal allows registered users to contribute new material and greatly simplifies the maintenance of the site. Although registration is not required to access most of the content of the Gateway, we strongly encourage users to register using the “Create Account” button at the top of the page to take full advantage of all its content.

Science Gateway web interface

The URL for the Science Gateway is <https://rbspgway.jhuapl.edu/> and the front page on the Science Gateway is illustrated in Figure 23.

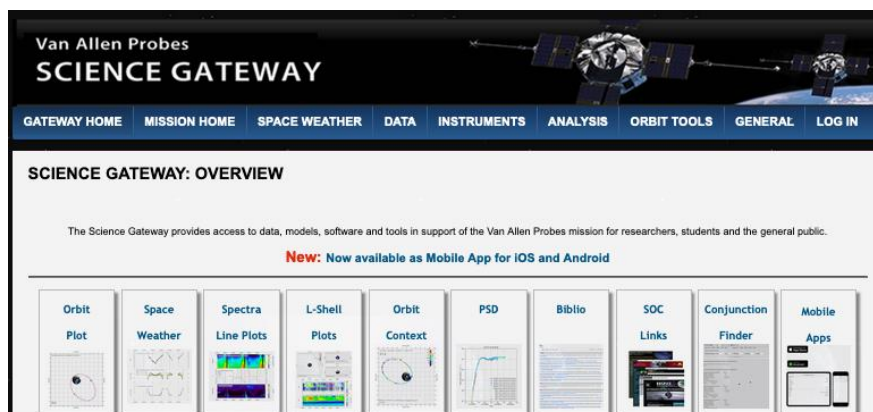


Figure 23 Front page of the Van Allen Probes Science Gateway showing the capabilities available for users.

The page contains a main menu at the top of the page, and shortcut links for the most used tools in the form of clickable icons/buttons.

Plotting Utilities

The Van Allen Probes mission contains several instruments, and the needs of the Science Gateway plotting utilities were expected to fit the following requirements:

- Flexible to handle all the data different format from all instruments.
- Able to generate different, high-quality plots (spectrograms, line plots, L-shell, Orbit-context, etc.)
- Capable of handling large amount of data with very little burden on the user/client side.
- Available via web from everywhere, to everyone (on mobile and non-mobile devices).
- Wide range of user customizations.
- Capable of saving the user created plot in the form of a URL, to be retrieved at a later time, and also capable of saving the user plot in PNG or PDF format.
- Allowing users to download the data used to generate the plots in CDF files. These files are not the same as the originally generated SOC files since they contain only a subset of the original data.

The Van Allen Probes Science Gateway can generate plots based on CDF files coming from each instrument SOC. Users have also access to auxiliary data such as DST, Kp indices together with solar wind speed data from ACE/OMNI. Users can also add MLT/MLAT/L-shell as auxiliary x-axis for each spacecraft. Plots are available as spectrograms/line plots, L-shell plots, and orbit-context plots. All links for these types of plots are under the “DATA” in the top main menu. The plotting infrastructure is based on a combination of JavaScript and PHP for the client side, and C-compiled code for the server side.

Spectrograms and Line Plots

All Van Allen Probes related data can be used to generate either spectrograms or line plots, depending on the type of data. This includes level 2 (L2), level 3 (L3), level 4 (L4), and Space Weather data. The page main user interface is shown in Figure 24.



Figure 24 Plotting main user interface for the Van Allen Probes Science Gateway

Users can select the end of the time interval and its extent back in time. The “Customize” button allows the addition/deletion of plots and also their customization as shown in figures :

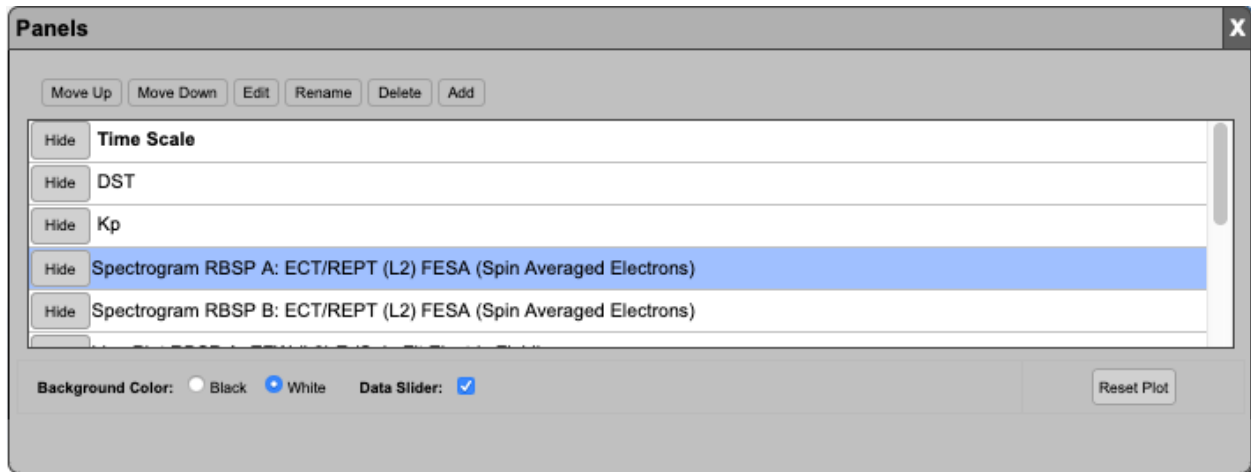
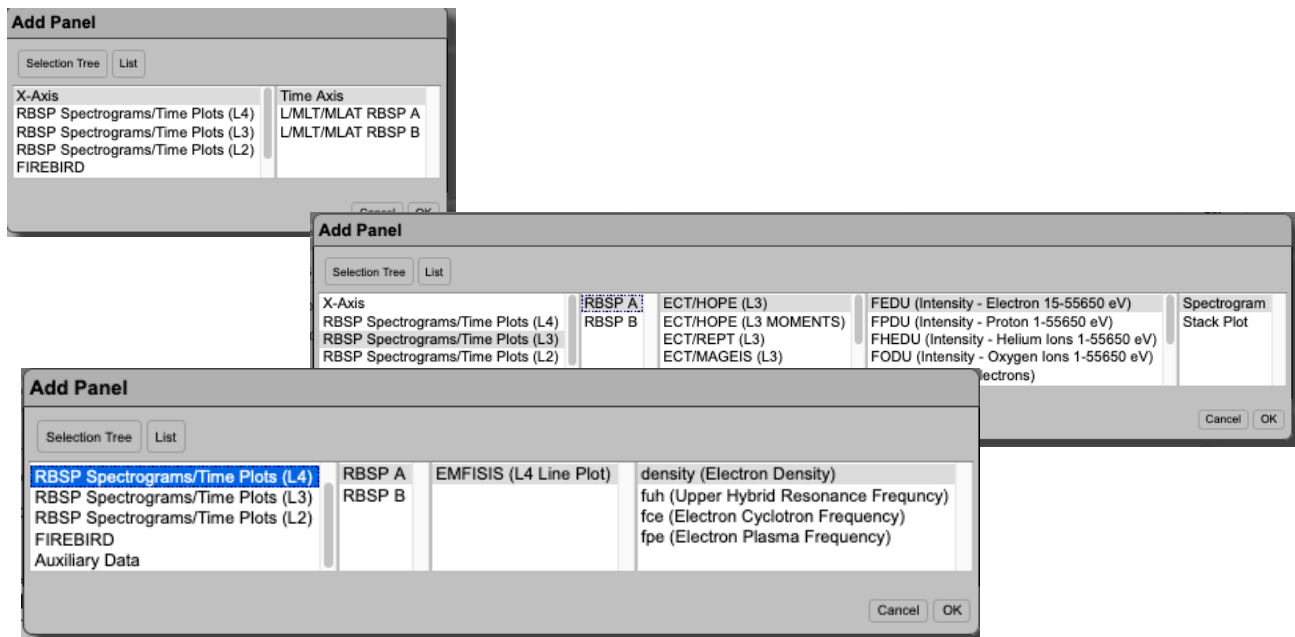
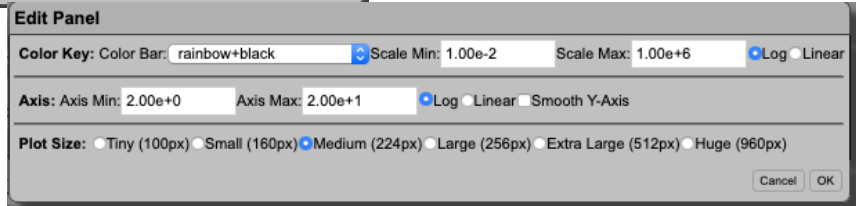
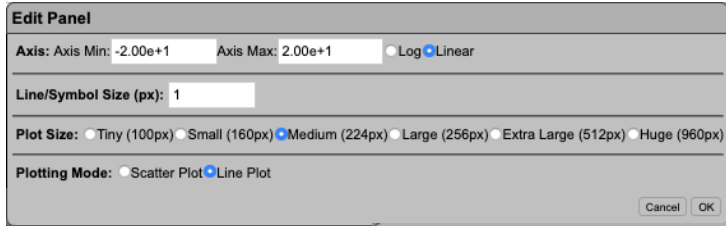


Figure 25 Data selection user interface.

To create a new plot, a user selects the “Add” button, and the dialog shown in Figure xxx is displayed.

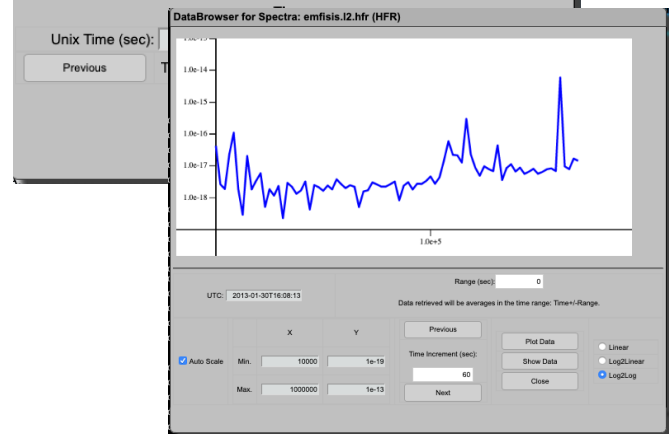
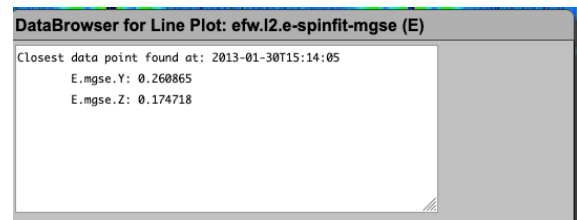


This allows to select all Van Allen Probes data, and also FIREBIRD and Auxiliary data such as Solar Wind data. Once the data type and plot type (where applicable) is selected and the plot has been generated, it can be further customized by selecting, and clicking the “Edit” button on the main “Customize” dialog. The “Edit” dialog format depends on the type of plot. Here are some examples for Line plot and Spectrogram:



Data Slider

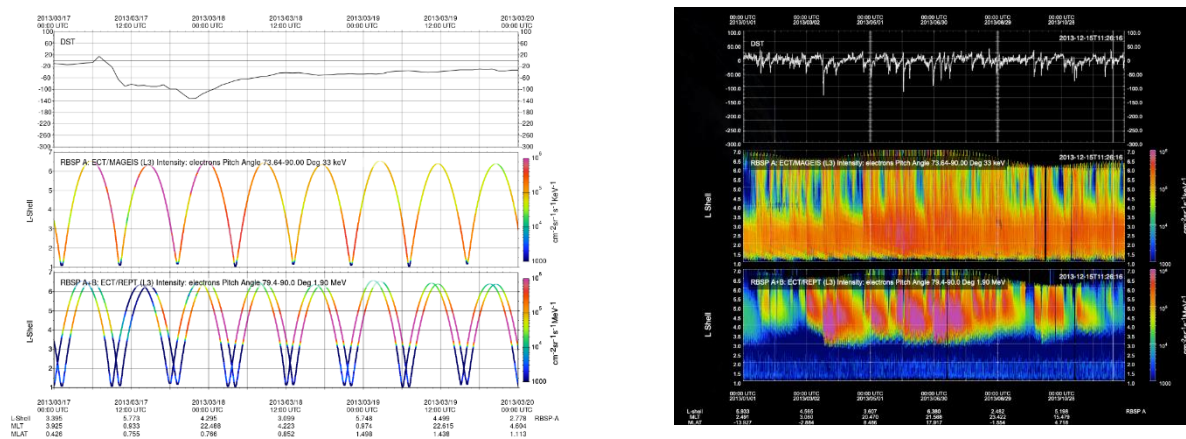
When hovering on plots with the mouse, a vertical line will appear; this is the data slider (as seen in the image on the left below) that allows to slice the data at the selected time when the user click with the mouse on the plot. The dialogs on the right will appear:



The Data Slider can easily be disabled by using the “Customize” button.

L-shell Plots

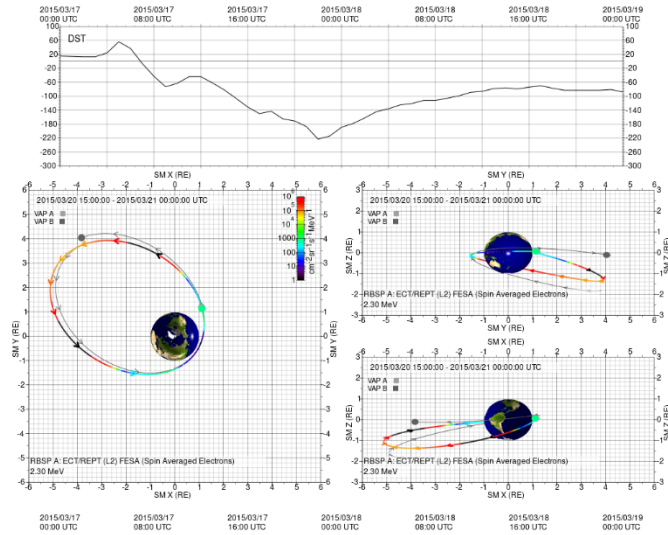
The Van Allen Probes Science Gateway offers also the capability of creating L-shell plots for spacecraft A, B and their combination:



Data can be plot in time intervals that range from 6 minutes to 360 days; the data slider is available for L-shell plots.

Orbit context Plots

The Science Gateway offers the capability of creating orbit context plots where data from the select spacecraft and instrument are overlaid on the probe orbit at the selected time:



Saving Plots

The Plotting infrastructure on the Science Gateway allows 3 different ways to save a plot.


1. Downloading the plots as PDF file
2. Downloading the plots as PNG file
3. Generate a unique URL and QR code that can be share with collaborators

URL/QR Code

The URL listed below can be used to recreate the current plot. Please copy the exact form of the URL when you distribute it.

<http://rbspgway.jhuapl.edu/rPlotTime?orb.UzMeN>

The URL is also encoded into the QR code shown below. You can recreate the plot by scanning this code.



[Download Image](#)

Downloading Plots Data

After creating and customizing plots, users can directly download the data used to generate their plot through an ad-hoc CDF. This file will contain ONLY the mentioned data, and must not be confused with the official instrument SOC generated files. Notice that this feature is available only to users who have an account on the Science Gateway, and have logged into their account. Once the “Get Data” button is clicked, the process of making the ad-hoc CDF file is run on server, and the user will receive an email telling where to download the files and their expiration date.

PLANNING TOOLS

The Science Gateway offers a wide range of web applications that can be used for planning purposes, starting with position calculator, but also orbital tools such as Multi Mission Orbit Plotter and the Conjunction Finder. All these tools will be described below.

[Multi Mission Orbit Plotter](#)

This web applications allows to plot orbits for a selected time interval of several space missions, related to the Van Allen Probes. The main interface is illustrated below

Time (UTC): Previous 1 June 2019 00:00 Next Time Step: 10 Minutes Length of Orbit Track: 9 Hours

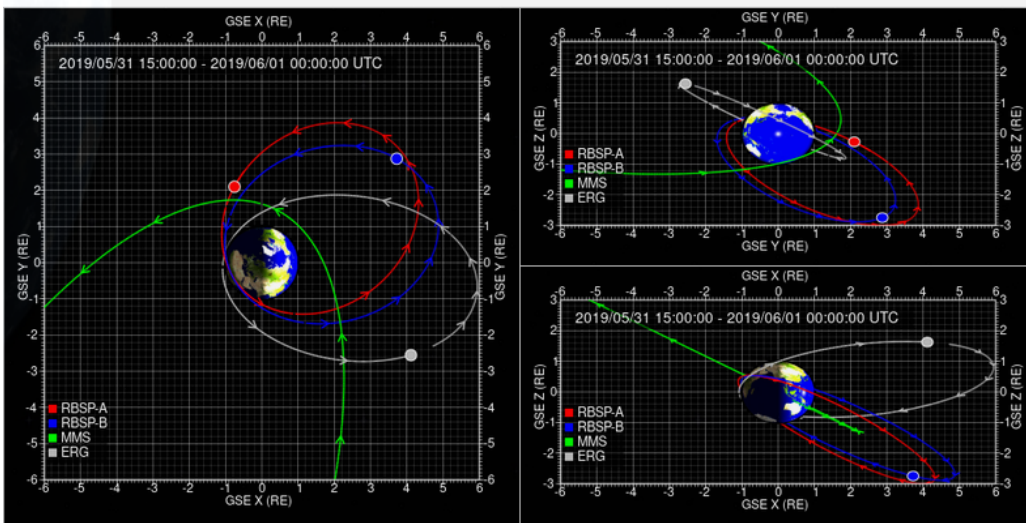
Coordinate System: GEI GEO GSM GSE SM Plot Scale: 6 RE Tick Mark Interval: 60 Minutes Show Grid Show Realistic Earth

Background Color: Black White

Orbit Tracks:

Spacecraft	Show	Track Color	Track Thickness
RBSP A	<input checked="" type="checkbox"/>	Red	Medium
RBSP B	<input checked="" type="checkbox"/>	Blue	Medium
MMS	<input checked="" type="checkbox"/>	Green	Medium
ERG	<input checked="" type="checkbox"/>	Grey	Medium
CLUSTER-1	<input type="checkbox"/>	Yellow	Thin
CLUSTER-2	<input type="checkbox"/>	Lime	Thin
CLUSTER-3	<input type="checkbox"/>	Crimson	Thin
CLUSTER-4	<input type="checkbox"/>	Coral	Thin
THEMIS	<input type="checkbox"/>	Orange	Thin
GEOTAIL	<input type="checkbox"/>	Purple	Thin
GOES13	<input type="checkbox"/>	Cyan	Thin
FIREBIRD3	<input type="checkbox"/>	LightGreen	Thin
AEROCUBE6	<input type="checkbox"/>	Brown	Thin
DSX	<input type="checkbox"/>	Teal	Thin
PROBA-V	<input type="checkbox"/>	Coral	Thin

Hide Spacecraft Options Get PDF Get PNG



The interface allows to user to customize the plot by

- Selecting the end of the time interval and its extent
- Change the coordinate frame (choices are GEI, GEO, GSM and SM)
- Zoom in or out by changing the “Plot Scale”; units are in R_e
- The “Tick Mark Interval” allows the user to set when the orbital ticks are to be plotted
- Add or remove a spacecraft, and customize the color used to plot the orbit, and the thickness of the orbital line
- Plots can be downloaded either as PDF or PNG files.

Conjunction Finder

This tool allows to find times when 2 selected spacecraft are in conjunction. Unfortunately, the definition of “conjunction” is not unique, and it might entail different conditions for different users. The finder on the Science Gateway uses several user-specified parameters to identify such time intervals when the selected spacecraft are said to be in conjunction. The parameters are

1. Δr – Spatial separation between the spacecraft
2. $\Delta \rho$ – Spatial separation between the spacecraft in X-Y plane
3. Δmlt – Separation in mlt (magnetic local time)
4. $\Delta mlat$ – Separation in magnetic latitude
5. ΔL – Separation in L-shell

Notice that any parameter left blank will not be used. Users can choose to find conjunction between several satellites. The tool is available at <https://rbspgateway.jhuapl.edu/conjfind> and has the interface illustrated below:

Time (UTC): Previous 20 May 2019 14:00 Next Extent: 15 Days

Spacecraft 1: RBSP A
 RBSP B
 ARASE
 MMS1
 DSX
 PROBA-V
 CLUSTER-FM5
 CLUSTER-FM6
 CLUSTER-FM7
 CLUSTER-FM8
 THEMIS-A
 THEMIS-D
 THEMIS-E
 DMSP-18

Spacecraft 2: ARASE

Conjunction Criteria: $\Delta p_{x,y}$ 0.4 Δmlt (hours) $\Delta mlat$ (deg) ΔL -shell

Find Conjunctions Get ASCII

Conjunction between spacecraft RBSP A and ARASE with these parameters:
 $\Delta p_{x,y} = 0.4$

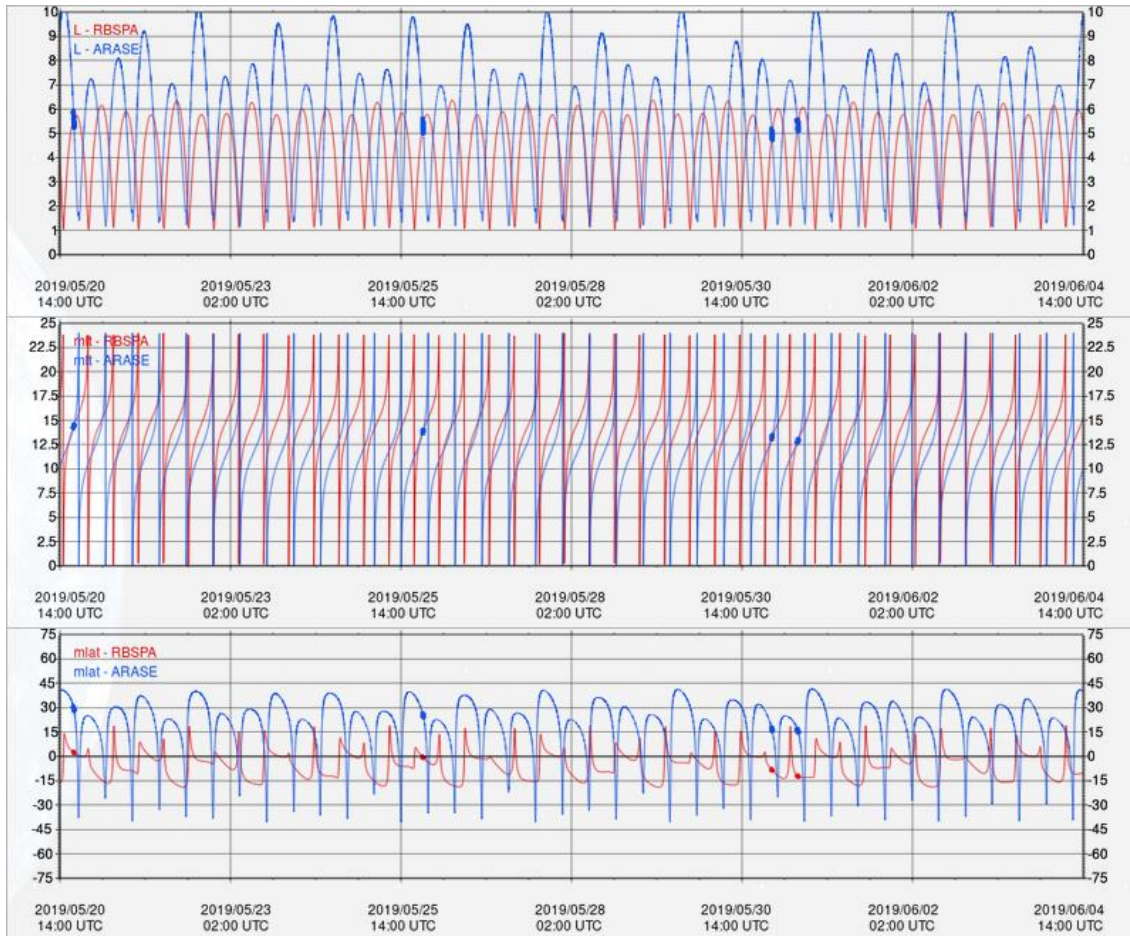
Minimum Distance between spacecraft: 16827.9 km
Minimum rho difference: 0.105
Minimum L difference: 0.009
Minimum MLT difference: 0.002 hours
Minimum MLAT difference: 26.232 deg
Conjunction 1
Start Time: 2019-05-20T18:43:00
End Time: 2019-05-20T18:58:00
Duration: 15 minutes

Minimum Distance between spacecraft: 15113.4 km
Minimum rho difference: 0.095
Minimum L difference: 0.012
Minimum MLT difference: 0.023 hours
Minimum MLAT difference: 25.202 deg
Conjunction 2
Start Time: 2019-05-25T21:36:00
End Time: 2019-05-25T21:52:00
Duration: 16 minutes

Minimum Distance between spacecraft: 13620.3 km
Minimum rho difference: 0.095
Minimum L difference: 0.020
Minimum MLT difference: 0.129 hours
Minimum MLAT difference: 24.401 deg
Conjunction 3
Start Time: 2019-05-31T00:24:00
End Time: 2019-05-31T00:40:00
Duration: 16 minutes

Minimum Distance between spacecraft: 15370.7 km
Minimum rho difference: 0.095
Minimum L difference: 0.004
Minimum MLT difference: 0.041 hours
Minimum MLAT difference: 27.336 deg
Conjunction 4
Start Time: 2019-05-31T09:28:00
End Time: 2019-05-31T09:49:00
Duration: 21 minutes

Furthermore, the tool generates the plots below to help visualize better the time intervals during which the conjunctions take place:



Position Calculator and Orbit Number Calculator

The Position Calculator generates spacecraft position in several coordinate frames and for user specified time intervals:

Time (UTC): Previous 20 May 2020 14 00 Next Extent: 24 Hours

Coordinate System: GEI GEO GSM GSE SM Spacecraft: RBSP A RBSP B ARASE Include Header

Get ASCII

The Spacecraft Ephemerides cover the following interval:

Start Date: Thu, 30 Aug 2012 09:24:00 GMT End Date: Wed, 14 Oct 2020 00:00:02 GMT

Year	Month	Day	Hour	Minute	Second	SMX (km)	SMY (km)	SMZ (km)
2020	05	20	14	00	00	-30014.355469	-15481.236328	-6609.105957
2020	05	20	14	01	00	-30003.298828	-15613.829102	-6636.519043
2020	05	20	14	02	00	-29991.105469	-15745.883789	-6663.789551
2020	05	20	14	03	00	-29977.777344	-15877.398438	-6690.917480
2020	05	20	14	04	00	-29963.320312	-16008.370117	-6717.900879
2020	05	20	14	05	00	-29947.742188	-16138.795898	-6744.738770
2020	05	20	14	06	00	-29931.046875	-16268.672852	-6771.430664
2020	05	20	14	07	00	-29913.238281	-16398.000000	-6797.974609
2020	05	20	14	08	00	-29894.324219	-16526.773438	-6824.370117
2020	05	20	14	09	00	-29874.306641	-16654.990234	-6850.616699
2020	05	20	14	10	00	-29853.193359	-16782.648438	-6876.711914
2020	05	20	14	11	00	-29830.990234	-16909.746094	-6902.655762
2020	05	20	14	12	00	-29807.699219	-17036.279297	-6928.446777
2020	05	20	14	13	00	-29783.326172	-17162.248047	-6954.083984
2020	05	20	14	14	00	-29757.876953	-17287.644531	-6979.566406
2020	05	20	14	15	00	-29731.355469	-17412.472656	-7004.892578

Similarly, the Orbit Number Calculator generates the orbit number

Time (UTC): Previous 20 May 2020 15 00 Next Extent: 72 Hours

Mode: Ascending Node Perigee Spacecraft: RBSP A RBSP B

Get ASCII

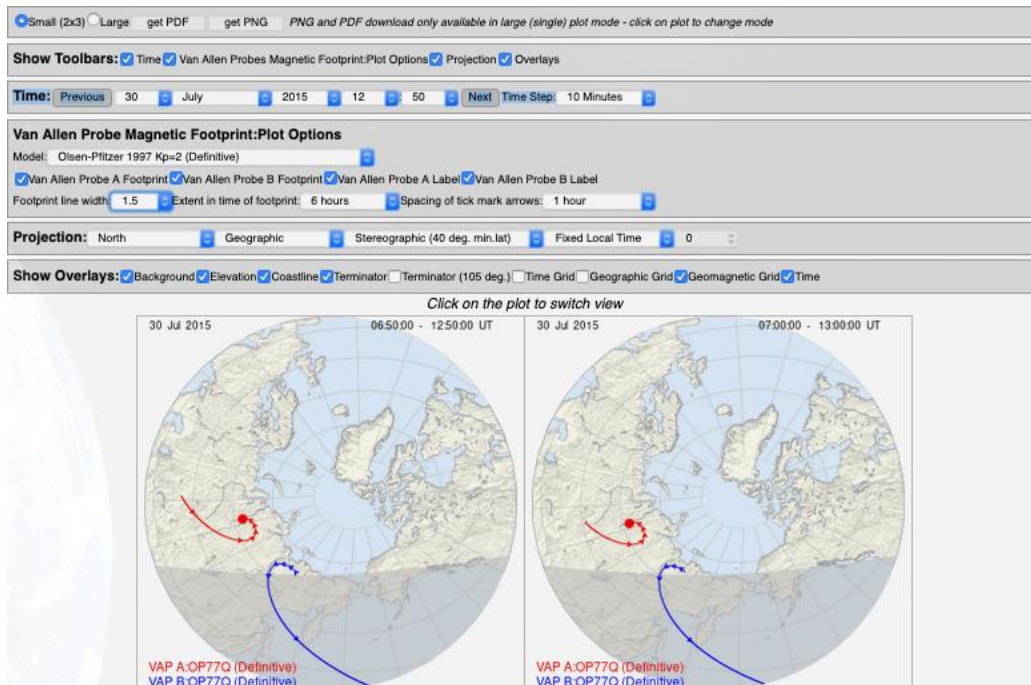
The currently available spacecraft ephemerides cover the following interval:

Start Date: Thu, 30 Aug 2012 09:24:00 GMT End Date: Wed, 14 Oct 2020 00:00:02 GMT

No.	Event UTC	A-NODE	Event SCLK	A-NODE	OP-Event UTC	D-NODE	SC Lon	SC Lat	Alt	Inc	Ecc	LonNode	Sem
7585	2020 MAY 20 19:18:05		1/0327698287:25050		2020 MAY 20 20:15:46		224.33	-0.00	2411.92	10.09	0.694	32.96	2
7586	2020 MAY 21 04:00:42		1/0327729645:06769		2020 MAY 21 04:58:08		93.13	0.00	2439.51	10.09	0.694	32.77	2
7587	2020 MAY 21 12:43:19		1/0327761001:42855		2020 MAY 21 13:40:31		321.93	0.00	2467.56	10.09	0.694	32.59	2
7588	2020 MAY 21 21:25:55		1/0327792357:42494		2020 MAY 21 22:22:52		190.74	-0.00	2495.35	10.09	0.694	32.41	2
7589	2020 MAY 22 06:08:30		1/0327823712:40641		2020 MAY 22 07:05:13		59.55	0.00	2523.76	10.09	0.694	32.22	2
7590	2020 MAY 22 14:51:04		1/0327855066:41822		2020 MAY 22 15:47:33		288.36	-0.00	2552.65	10.09	0.694	32.03	2
7591	2020 MAY 22 23:33:37		1/0327886420:01145		2020 MAY 23 00:29:53		157.19	-0.00	2581.35	10.09	0.694	31.85	2
7592	2020 MAY 23 08:16:10		1/0327917772:08913		2020 MAY 23 09:12:11		26.01	0.00	2610.66	10.09	0.694	31.67	2

Magnetic Footprint

This tool allows the user to calculate the magnetic footprint of both spacecraft for selected time intervals using different magnetic ephemerides obtained from different models. The interface is illustrated in the figure below. Users can download the customized plots as PNG, PDF or as Google Earth KMZ files.



VAN ALLEN PROBES BIBLIOGRAPHY

The Science Gateway offers the capability of accessing a searchable bibliography of all published related to the Van Allen Probes scientific mission and its findings. The bibliography contains currently more than 900 entries, and it is maintained on a monthly basis. The interface offers the capability of searching the bibliographic archive using

- Author Last Name
- Keyword
- Publication Year

Bibliography

Hide Biblio Search

NOTICE: Use the parameters below to customize your search. Regular expressions and boolean "AND" will to match the search. In the case of "Author name", the search is performed using only for the last name.

Author name:
Keyword:
Year:

Search Biblio

Reset Search

Found 180 entries in the Bibliography.

Showing entries from 1 through 50

2020

[Global ENA Imaging and In Situ Observations of Substorm Dipolarization on 10 August 2016](#)

Abstract This paper presents the first combined use of data from Magnetospheric Multiscale (MMS), Two Wide-angle Imaging Neutral-atom Spectrometers (TWINS), and Van Allen Probes (RBSP) to study the 10 August 2016 magnetic dipolarization. We report the first correlation of MMS tail observations with TWINS energetic neutral atom (ENA) images of the ring current (RC). We analyze 15-min, 1° TWINS 2 images in 1–50 keV energy bins. To characterize the high-altitude RC we extract peak ENA flux from L= 2.5 to 5 in the postmid ...

Goldstein, J.; Valek, P.; McComas, D.; Redfern, J.; Spence, H.; Skoug, R.; Larsen, B.; Reeves, G.; Nakamura, R.;

YEAR: 2020 DOI: 10.1029/2019JA027733

substorm dipolarization; cross-scale physics; imaging; multipoint in situ; ring current; Van Allen Probes

[Radial Response of Outer Radiation Belt Relativistic Electrons During Enhancement Events at Geostationary Orbit](#)

Abstract Forecasting relativistic electron fluxes at geostationary Earth orbit (GEO) has been a long-term goal of the scientific community, and significant advances have been made in

Each entry contains a link in the publication title that leads to a page that reports the amount of information illustrated in the figure below

Global ENA Imaging and In Situ Observations of Substorm Dipolarization on 10 August 2016

Author	J. Goldstein P. Valek D. McComas J. Redfern H. Spence R. Skoug B. Larsen G. Reeves R. Nakamura
Keywords	substorm dipolarization cross-scale physics imaging multipoint in situ ring current Van Allen Probes
Abstract	Abstract This paper presents the first combined use of data from Magnetospheric Multiscale (MMS), Two Wide-angle Imaging Neutral-atom Spectrometers (TWINS), and Van Allen Probes (RBSP) to study the 10 August 2016 magnetic dipolarization. We report the first correlation of MMS tail observations with TWINS energetic neutral atom (ENA) images of the ring current (RC). We analyze 15-min, 1° TWINS 2 images in 1–50 keV energy bins. To characterize the high-altitude RC we extract peak ENA flux from L= 2.5 to 5 in the postmidnight sector. We estimate peak low-altitude ion flux from ENAs near the Earth's limb. For a local perspective, we use spin-averaged proton fluxes from the RBSP A Helium Oxygen Proton Electron (HOPE) spectrometer. We find that the 1000 UT dipolarization triggered an abrupt and significant increase in low-altitude ions and a gradual but modest increase in the high-altitude RC. The relative strength and timing of the low versus high-altitude flux indicate that the dipolarization isotropized the injected ions and initially filled the loss cone. The substorm injection brought cooler ions in from the magnetotail, reducing the peak energy at both low and high altitudes. The post-dipolarization low-altitude flux exhibited a decay rate dispersion favoring longer decay times at lower energies, possibly caused by growth of the low energy RC providing enhanced flux into the loss cone. A variety of finer scale local injection structures were observed in the high-altitude RC both before and after the dipolarization, and the average system level RC intensity increased after 1000 UT.
Notes	
Year of Publication	2020
Journal	Journal of Geophysical Research: Space Physics
Volume	125
Number	
Date Published	04/2020
URL	https://agupubs.onlinelibrary.wiley.com/doi/abs/10.1029/2019JA027733
DOI	10.1029/2019JA027733
	Google Scholar DOI BibTeX EndNote X3 XML EndNote 7 XML Endnote tagged Marc RIS

1 The TS07D Empirical Magnetic Field Model

The Van Allen Probes Science Gateway serves as the host of the TS07D empirical magnetic field model (Tsyganenko & Sitnov, 2007; Sitnov and Tsyganenko, 2008). Empirical magnetic field models have long been useful tools in magnetospheric physics as they allow for evaluation of the global 3D magnetic field. This enables observations to be correlated via the tracing of magnetic field lines, a necessary capability in mapping ground and ionospheric signatures to the magnetosphere and vice versa, determination of spacecraft magnetic conjunctions, and evaluating spacecraft footpoints. Additionally, knowledge of the 3D magnetic field is necessary in computing particle adiabatic invariants and tracing particle paths through the magnetosphere.

The general approach to empirical modeling is to formulate an analytical description of the system and then fit the corresponding non-linear parameters and linear amplitude coefficients to the available data. However, this is not straight forward for the magnetosphere. Not only does the magnetosphere react to changes in the solar wind, such as increasing and decreasing in size with changes in solar wind dynamic pressure P_{dyn} , it also undergoes global internal reconfigurations, for example during geomagnetic storms. Furthermore, there is a limited amount of data considering the volume of the magnetosphere is on the order $\sim 10^4 R_E^3$ (when limiting the modeling domain to $25 R_E$ down tail) and at any given moment there only on the order of tens or less magnetospheric spacecraft equipped with scientific magnetometers taking observations above low earth orbit. The earlier approaches (Tsyganenko, 2013 and references therein) were to individually formulate a description of the magnetic field for each of the primary electric current systems: the field-aligned current (FAC), symmetric ring current (SRC), partial ring current (PRC), tail current, and their associated magnetopause currents. The size and magnitude of these systems were made to be predefined functions of solar wind values and geomagnetic indices. The parameters of these functional forms were then found by performing a least-squares regression against the database of the available magnetometer data. The primary shortcoming of this earlier approach is that it is rigid both spatially and temporally. The TS07D model sought to enable the data to dictate the current sheet morphology instead of the model developer using two conceptual advancements. Firstly, the rigid equatorial current descriptions (SRC, PRC, and tail current) are replaced by a single regular expansion with no predefined azimuthal or radial structure (Tsyganenko & Sitnov, 2007). Secondly, the dynamical evolution of the system is driven by a simple albeit powerful data-mining technique termed nearest-neighbors (Cover & Hart, 1967). The general idea is that during a geomagnetic storm the state of the magnetosphere can be characterized by a finite dimensional state-space (Vassiliadis, 2006). This state-space is constructed from a set of macroscopic parameters derived from solar wind measurements and geomagnetic indices. As storms progress in time they trace similar trajectories in this state-space. Thus, although at any given moment during a storm there are only several spacecraft observations, in state-space there are numerous observations from moments when the magnetosphere was presumably in a similar configuration. This bin of data points is then used to fit the model's non-linear parameters and linear amplitude coefficients. Likewise, every other step in time (the TS07D model uses a 5 min cadence) also has a unique bin of data points and resulting parameter and coefficient fit.

Because the magnetometer data now drives the equatorial current structure, the TS07D model is a powerful scientific tool in its own right. The model has been used to contrast the morphology of the ring current dynamics during geomagnetic storms driven by coronal mass injections (CMEs) versus those driven by corotating interaction regions (CIRs) (Sitnov et al., 2007, 2010). During CME driven storms it found the magnetosphere responds by forming a hook like PRC that closes through a region-2 FAC. In contrast, during CIR driven storms the formation of the region-2 FAC is inhibited, forcing the PRC to instead close through the magnetopause, resembling a strong tail-like current system. It was then applied to steady magnetospheric convection events (SMCs), finding two distinctive tail configurations (Stephens et al., 2013).

Figure 1 showcases TS07D's reconstruction of the magnetospheric current systems during the March 2015 Saint Patrick's day storm, the strongest storm to occur during the Van Allen Probes mission. The left set of panels are of the quiet-time magnetosphere several hours before the CME

arrives. All current systems are relatively weak or nearly non-existent, with the only discernable feature being a tail-like current at $7 R_E \leq r \leq 15 R_E$. The center panels are during the main phase of the storm, when the storm index $Sym-H^* = 150$ nT. The whole magnetosphere is now quite compressed as $P_{Dyn} \approx 15$ nPa. There is a large degree of day-night asymmetry, with equatorial currents generally being much stronger on the nightside. The divergence of the equatorial arrows on the night side at $r \approx 4 R_E$ and strength of the region-2 FACs indicates the formation of a PRC. The nightside field lines are extremely stretched while the dayside is compressed. A relatively small amount of the nightside equatorial current flows to noon, with the rest either closing through the ionosphere or outflowing to the magnetopause. The right panels are ten hours later. By this time the solar wind driving has diminished, allowing the storm to enter the early recovery phase. Although $Sym-H^*$ is similar in magnitude to the center panels, the morphology is quite different. P_{Dyn} has returned to a nominal level, expanding the magnetosphere. The FAC intensity is similar, but they have begun to shift poleward. While a day-night asymmetry still exists in the ring current, much less of the nightside current closes through the magnetopause, and instead closes through a clearly developed SRC. This indicates the particle trajectories are now largely on closed drift paths, and that convection of particles on open drift paths has diminished. The nightside field lines are still quite stretched to about $r = 15 R_E$ in which the stretching abruptly stops.

Here, the TS07D model will be described in two parts. The first part will overview the model's architecture (section 1.1) including the mathematical description of the magnetic field (section 1.1.1) followed by the nearest-neighbor data-mining algorithm (section 1.1.3). Next, section 1.2 will detail the model's source code and describe how users can find and use the model for themselves.

1.1 TS07D Model Architecture

1.1.1 Mathematical Description

Within the magnetosphere, the total magnetic field can be decomposed as the sum of the approximately dipolar internal field and the external field which is generated by electric currents flowing in space, $\mathbf{B}_{tot} = \mathbf{B}_{int} + \mathbf{B}_{ext}$. Although the internal field is instrumental in determining the magnetosphere's overall morphology, it originates from the magnetic dynamo deep inside the Earth and thus is beyond the scope of magnetospheric physics. The TS07D model only attempts to capture the external magnetic field and the commonly used International Geomagnetic Reference Field (IGRF) model (Thébault et al., 2015) is employed to represent the internal field. Although the current systems are interconnected it is useful to model each individually. Here, the external magnetic field is assumed to be comprised from the equatorial currents, FACs, and magnetopause currents, $\mathbf{B}_{ext} = \mathbf{B}_{eq} + \mathbf{B}_{FAC} + \mathbf{B}_{MP}$.

The first major advancement of the TS07D model was to replace the ad-hoc mathematical descriptions of the SRC, PRC, and tail currents with a single regular expansion (Tsyganenko & Sitnov, 2007). This expansion derives from the general solution of the magnetic scalar potential

of a thin current sheet, from which the magnetic vector potential equivalent is derived, the curl of which has the form

$$\mathbf{B}_{eq}(\rho, \phi, z) = \sum_{n=1}^N a_{0n}^{(s)} \mathbf{B}_{0n}^{(s)} + \sum_{m=1}^M \sum_{n=1}^N (a_{mn}^{(o)} \mathbf{B}_{mn}^{(o)} + a_{mn}^{(e)} \mathbf{B}_{mn}^{(e)}) \quad (1)$$

where $\mathbf{B}_{0n}^{(s)}$, $\mathbf{B}_{mn}^{(o)}$, and $\mathbf{B}_{mn}^{(e)}$ are the basis fields having symmetric, odd, and even azimuthal symmetry respectively. The basis amplitude coefficients are thus represented by $a_{0n}^{(s)}$, $a_{mn}^{(o)}$, and $a_{mn}^{(e)}$ and are determined when the model is fit to the data. The resolution of the model is determined by the number of expansions represented by M and N , corresponding to the azimuthal and radial resolution respectively. If M and N are too small the model will smear out mesoscale features, on the other hand, if they are too large the data will be overfit. The adopted resolution is $(M, N) = (4, 5)$. In order to allow the equatorial current to respond to changes in the solar wind dynamic pressure P_{Dyn} the coefficients in equation (1) are replaced by $a_{\alpha\beta}^{(\gamma)} \rightarrow a_{0,\alpha\beta}^{(\gamma)} + a_{1,\alpha\beta}^{(\gamma)} \sqrt{P_{Dyn}}$. Panels c, e, and g in Figure 1 demonstrate how this equatorial description naturally reconstructs tail like currents (Figure 1c and 1e), SRCs (Figure 1g), and PRCs (Figure 1e and 1g).

A further complication is that the Earth's approximately dipolar magnetic field \mathbf{B}_{int} is not perpendicular to the flow of the solar wind. Near the planet ($r \lesssim 4R_E$), the magnetosphere morphology generally aligns with the solar magnetic (SM) coordinate system in which the primary axis is the magnetic dipole. Further away ($r \gtrsim 8R_E$), the geocentric solar magnetic (GSM) coordinate system is more appropriate as its primary axis is along the sun-earth line, the approximate direction of the solar wind flow. The angle between these two coordinate systems is termed the dipole tilt angle and it continuously changes as the Earth rotates and orbits the sun. To account for this effect, the general deformation technique (Stern, 1987; Tsyganenko, 1998) is employed. In particular, this technique is used to bend, warp, and twist the flat current system presented in equation (1) into a shape that more accurately reflects the actual configuration of the equatorial currents (Tsyganenko, 2002) due to dipole tilt angle effects. Figure 1d, 1f, and 1h demonstrate the impact of the dipole tilt deformation on the equatorial currents. Note how near the planet the current sheet is perpendicular to the dipole axis, but further down the tail it aligns with the Sun-Earth axis instead.

The ionosphere connects to the magnetosphere via the FACs. When observed by low earth orbiting spacecraft, these appear as two sets of concentric ovals (Iijima & Potemra, 1976), the higher and lower latitude ovals termed region-1 and region-2 FACs respectively. TS07D describes these by bending a model of purely radially directed conical currents sheets $\mathbf{J} = J_r \hat{\mathbf{r}}$ (Tsyganenko, 1991) to match the realistic shape of magnetic field lines (Tsyganenko, 2002) using the general deformation technique, which also accounts for both the day-night asymmetry and dipole tilt effects. Two such systems are used, one for the region-1 and one for the region-2 FACs, with the latter being allowed to rotate in local time. Two free parameters are introduced that allow the systems to independently shift equatorward and poleward. An ionospheric slice of the FACs are inset in Figure 1c, 1e, and 1g, showing their evolution during the March 2015 Saint Patrick's day storm. The divergence of the equatorial arrows on the night side, at $r \approx 4 R_E$ and

$r \approx 6 R_E$ for the main and recovery phases respectively, shows how the region-2 system interacts with the equatorial system to naturally form a PRC.

The TS07D model assumes a closed magnetosphere, that is, the total magnetic field does not penetrate the magnetopause boundary, which can be represented by $\mathbf{B}_{tot} \cdot \mathbf{n}|_S = 0$, where S is the model's magnetopause surface and \mathbf{n} is the normal on that surface. The only field not yet defined is \mathbf{B}_{MP} , meaning the above constraint must be used to define this field. Although in the real magnetosphere \mathbf{B}_{MP} is generated by magnetopause currents, it is convenient to limit the domain of the model to just inside the boundary. The result is that \mathbf{B}_{MP} is curl free and can be represented by a magnetic scalar potential, $\mathbf{B}_{MP} = -\nabla U_{MP}$, the solution of which is found by solving Laplace's equation $\nabla^2 U_{MP} = 0$ using separation of variable resulting in a regular expansion form for U_{MP} . Each of the magnetic fields inside the magnetopause is given a complementary shielding field such that $\mathbf{B}_{MP} = \mathbf{B}_{int}^{(sh)} + \mathbf{B}_{eq}^{(sh)} + \mathbf{B}_{FAC}^{(sh)}$. The exact form for $U_{MP,int}$, $U_{MP,eq}$, and $U_{MP,FAC}$ depends on the underlying geometry of the field that is being shielded. For example, $U_{MP,int}$ (appendix of Tsyganenko, 1998) and $U_{MP,FAC}$ (eq. 34 of Tsyganenko, 1995) use an expansion of Cartesian harmonics while $U_{MP,eq}$ is formulated using Fourier-Bessel harmonics (eq. 20 of Tsyganenko & Sitnov, 2007). The coefficients of these expansions are determined by sampling the model's magnetopause boundary and minimizing $(\mathbf{B} + \mathbf{B}^{(sh)}) \cdot \mathbf{n}$ using linear least squares regression.

When the solar wind P_{Dyn} increases, in order to ensure pressure balance, the magnetosphere compresses and likewise decreases in P_{Dyn} expands the magnetosphere. As with nearly all other empirical magnetic field models (Tsyganenko, 2013), the TS07D model assumes the entire magnetosphere expands and contracts in a self-similar fashion. This is mathematically represented by a simple rescaling of the position vector $\mathbf{r}' = \mathbf{r}(P_{Dyn}/P_{Dyn,0})^\kappa$, where $P_{Dyn,0} = 2$ nPa is the baseline dynamic pressure and κ is taken to be 0.155 (Shue et al., 1998).

1.1.2 Database of Spaceborne Magnetometer Data

The spacecraft in the magnetometer database were chosen to overlap with the advent of continuous solar wind monitoring with the launch of the WIND spacecraft in late 1994 and the ACE spacecraft in 1997. Originally, the TS07D model was constructed with data from the Geotail, Cluster, Polar, GOES 8, 9, 10, and 12, Imp-8 missions (Tsyganenko & Sitnov, 2007). The database was later expanded to include the twin Van Allen Probes and the five THEMIS spacecraft (Stephens et al., 2019). This new database also reprocessed and extended the Cluster and Polar datasets.

The IGRF model field is subtracted from the spacecraft measurements so that only the external magnetic field remains. The vectors are then averaged to a 5 min cadence when the spacecraft are within $r < 5.0 R_E$ and 15 min cadence when $r \geq 5.0 R_E$ to reflect the slower spacecraft speeds. The data was filtered to limit the radial extent from $1.5 R_E \leq r \leq 31 R_E$. The lower limit eliminates potentially problematic measurements where the internal approximately dipolar field is relatively large making it difficult to distinguish the external field. The upper limit corresponds to the largest apogee used during the THEMIS mission. The sparsity of Geotail, THEMIS, and

IMP-8 data beyond this distance was found to sometimes make the fitting process unstable if they were included.

In total the database contains 3,589,288 records, and it is publicly available on the Space Physics Data Facility at the following URL: https://spdf.gsfc.nasa.gov/pub/data/aaa_special-purpose-datasets/empirical-magnetic-field-modeling-database-with-TS07D-coefficients/.

1.1.3 Data Mining

The second major advancement is the application of data-mining to determine the dynamical evolution the model. For a particular moment in time, the Nearest-Neighbor (NN) approach (Cover & Hart, 1967; Mitchell, 1997; Sitnov et al, 2008, 2012) identifies many other moments when the magnetosphere is in a similar configuration, allowing for a unique bin of magnetometer data to be used to fit the model, which is then repeated for each step in time. In this approach, the magnetosphere is assumed to be characterizable by a finite set of macroscopic parameters which form the components of a time-dependent state vector $\mathbf{G}(t)$ (Vassiliadis, 2006) which resides in a state-space. As TS07D is a storm-time model, the components of $\mathbf{G}(t)$ are formulated from three parameters that characterize storms, the solar wind electric field vB_z^{IMF} , the storm index $Sym-H$, and the time derivate of $Sym-H$.

A major driver of geomagnetic storms is a strong and prolonged southward interplanetary magnetic field (IMF). In particular, the solar wind electric field parameter vB_z^{IMF} (defined as the X_{GSM} component of the solar wind bulk flow velocity multiplied by the Z_{GSM} component of the IMF time propagated to the bow shock nose) is directly related to storm indices (Burton et al., 1975). As the westward flowing ring current intensifies during a storm, the horizontal (H) component of the magnetic field at mid and low-latitudes decreases which is observed by ground based magnetometers. By averaging across a collection of mid-latitude ground based magnetometers positioned around the globe a longitudinally symmetric H component index $Sym-H$ is computed (Iyemori, 1990). $Sym-H$ can be considered a higher resolution version of the DST index. Here, a dynamical pressure correction is applied $Sym-H^* = A \cdot Sym-H - B \cdot (P_{dyn})^{1/2}$ (Gonzalez, 1994 and references therein) where the values A and B are taken to be 0.8 and 13.0 respectively (Tsygaenko, 1996). Furthermore, the values are smoothed by convolving them with cosine windows (Sitnov et al., 2012):

$$G_1(t) = \langle Sym-H^* | \propto \int_{-\Pi/2}^0 Sym-H^*(t + \tau) \cos(\pi\tau/\Pi) d\tau \quad (2)$$

$$G_2(t) = D \langle Sym-H^* | / Dt \propto \int_{-\Pi/2}^0 Sym-H^*(t + \tau) \cos(2\pi\tau/\Pi) d\tau \quad (3)$$

$$G_3(t) = \langle vB_z^{IMF} | \propto \int_{-\Pi/2}^0 vB_z^{IMF}(t + \tau) \cos(\pi\tau/\Pi) d\tau \quad (4)$$

where the operators $\langle \dots |$ indicate that the limits of integration are only over past data. The proportionality signs reflect that the components of $\mathbf{G}(t)$ are normalized to give each dimension of the state-space similar scale lengths. A half window $\Pi/2 = 6$ hours is used to eliminate higher

frequency oscillations caused by noise and shorter time scale dynamics such as substorms. The impact of the smoothing process is plotted as the dashed and dotted lines in Figure 1a and 1b.

As a storm progresses in time $\mathbf{G}(t)$ will trace a trajectory in the 3D state-space. For the moment of interest t' there will be other storms in which $\mathbf{G}(t)$ will be close in the state-space (for example see Figures 2 and 3 in Sitnov et al., 2008). Once discretized (here to 5 min resolution) $\mathbf{G}(t)$ becomes individual points. Now for the moment of interest t' there is a set of K_{NN} other points $\{\mathbf{G}(t_i)\}$ which are closest to $\mathbf{G}(t')$ (its nearest-neighbors or NNs). Here the standard Euclidean metric is used to measure distance. Many of the points in the set of NNs will be adjacent in time as they represent segments of storms in the state-space. Each collection of adjacent NNs thus has a corresponding time interval associated with it. These time intervals are then intersected with the database of magnetometer data described in section 1.1.2 to assemble a unique bin for the moment of interest t' , thus mining the database for other data when the magnetosphere was most similar to t' . This unique bin of data is then used to fit the model resulting in a unique set parameters and coefficients for that moment. The non-linear parameters are fit using the down-hill simplex method while the linear amplitude coefficients utilize the singular value decomposition method for linear least squares (Press et al., 1992) by minimizing the difference between the modeled and observed magnetic field vectors (Tsyganenko & Sitnov, 2007). The number of NNs was chosen to be $K_{NN} = 8,000$, roughly one NN per R_E^3 . This process is repeated for each time step, thus allowing the data to dictate the model's dynamical evolution.

Throughout this work the source of the data used for the solar wind parameters and geomagnetic indices is the bow shock nose propagated 5 min cadence OMNI database (https://omniweb.gsfc.nasa.gov/ow_min.html), which compiles data from the IMP-8, ACE, WIND, Geotail, and DSCOVR missions as well as the World Data Center for Geomagnetism, Kyoto (<http://wdc.kugi.kyoto-u.ac.jp/>).

The above procedure for determining a unique bin of magnetometer data and resulting set parameters and coefficients has been performed for each step in time from the beginning of 1995 through the end of 2018 using the same 5 min cadence. The next section details how users can access the source code and run the TS07D model for themselves.

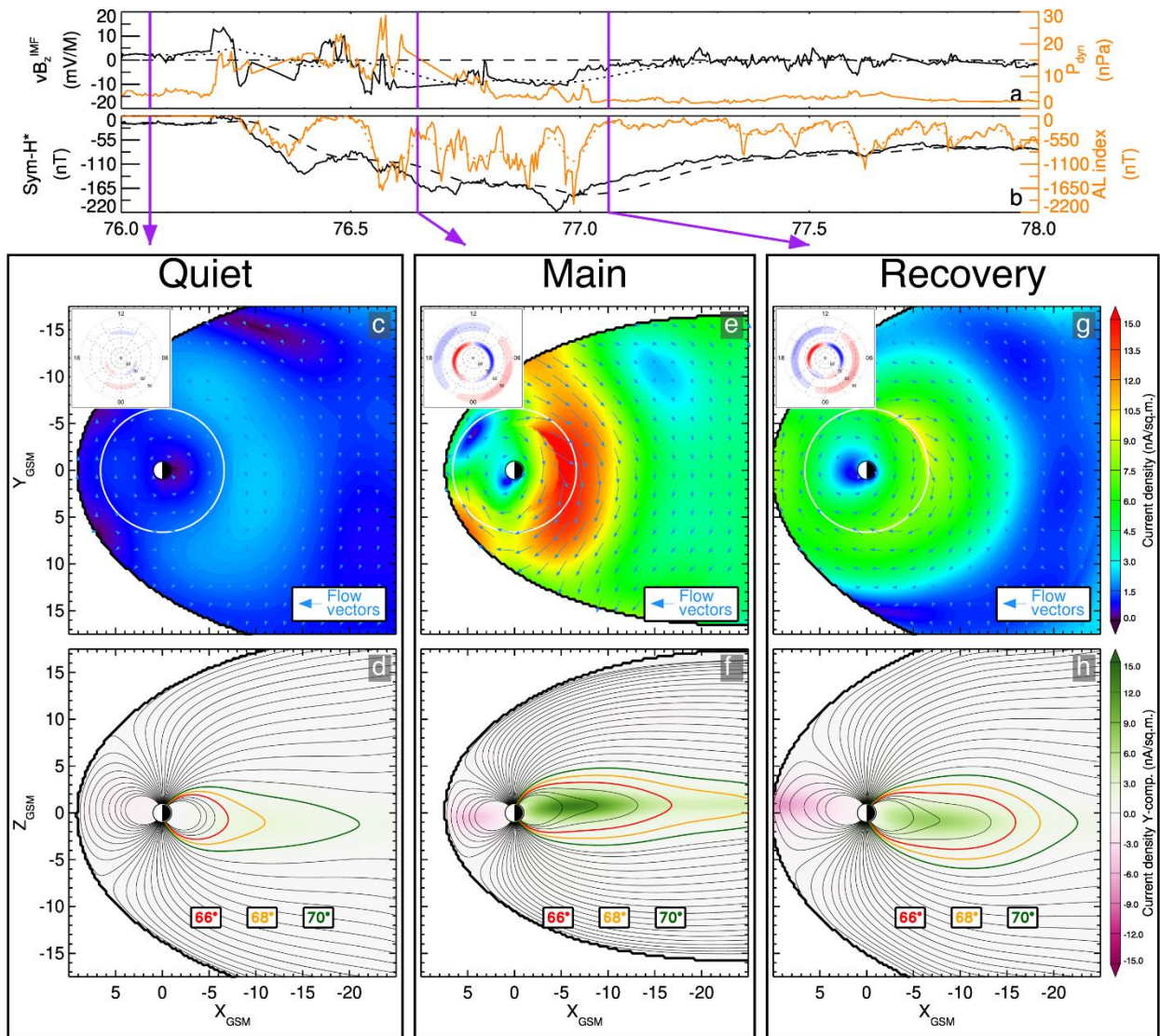


Figure 26: The TS07D reconstruction of magnetospheric current systems during the March 2015 Saint Patrick's day geomagnetic storm. (a) The solar wind electric field parameter vB_z^{IMF} (black line) and dynamic pressure (orange line). (b) The geomagnetic indices: pressure corrected storm index $Sym-H^*$ (black line) and substorm index AL (orange line). The dashed and dotted lines indicate the smoothed values. The purple vertical bars show the 3 moments of interest, corresponding to (c and d) the quiet time prior to the start of the storm, (e and f) the main phase of the storm, and (g and h) the early recovery phase of the storm. (c, e, and g) Equatorial slices (with no dipole tilt deformation effects) of the current density with the color representing the magnitude and the arrows showing the direction of the current density field. Inset in the upper left of this panel is the current density showing FACs flowing into (blue) and out of (red) the ionosphere. (d, f, and h) The meridional slices of the Y-component of the current density with the color indicating current flowing out of (green) and into (purple) the page. Magnetic field lines are overplotted in black starting from a magnetic latitude of 60° with a 2° step size, with three of the field lines being highlighted.

1.2 TS07D Model Usage

The model source code is hosted on the Van Allen Probes Science Gateway under ‘Analysis’ → ‘Model’ → ‘Empirical Geomagnetic Field Models’, or at the following link: https://rbspgway.jhuapl.edu/sites/default/files/SpaceWeather/ts07dmodel_july2017update.for. It is coded using a FORTRAN 77 style syntax which can readily be compiled using the freely available GNU Fortran compiler (<https://gcc.gnu.org/fortran/>).

The two primary advancements realized in the TS07D model, the regular expansion description of the equatorial current systems (section 1.1.1) and the data-mining driven dynamical evolution (section 1.1.2), both increase the complexity of the source code as compared to most other Tsyganenko models, which are available on Professor Tsyganenko’s website (<http://geo.phys.spbu.ru/~tsyganenko/modeling.html>). The former requires a large number of shielding coefficients. Typically, these are hard-coded, but here that is impractical. The later results in a unique set of non-linear parameters and amplitude coefficients for each moment in time. Both of these necessitate additional configuration steps. Users are encouraged to refer to the following example program provided on the gateway: http://rbspgway.jhuapl.edu/sites/default/files/SpaceWeather/ts07d_geopack_example_july2017update.for.

First, users must download the zip file containing static coefficients from the gateway onto their local machines (http://rbspgway.jhuapl.edu/sites/default/files/SpaceWeather/TAIL_PAR.zip) and then the file must be unzipped. Next, the coefficients from the files must be parsed and stored into the common blocks TSS, TSO, and TSE (see the example program). This step must be performed before the model can be evaluated, but it only needs to be done once.

The next step is to load the time dependent inputs. This includes the variable set of parameters and coefficients as well as the solar wind dynamical pressure P_{Dyn} . The coefficient files have been generated from the beginning of 1995, corresponding to the beginning of continuous solar wind monitoring by the WIND spacecraft, through the end of 2018 at a 5 min cadence and are located on the gateway at https://rbspgway.jhuapl.edu/new_coefs_mag_models_v02. They are compressed into tar archives for each day (~210 KB), year (~75 MB), and the complete set (~1.7 GB). Once downloaded, they will need to be decompressed and can then be parsed and loaded into the /PARAM/ common block. The format is human readable ASCII and each entry has been annotated with a brief description. Additionally, the dipole tilt angle and P_{Dyn} are appended to the end of the file and can also be parsed. P_{Dyn} needs loaded into the /INPUT/ common block, while the dipole tilt angle is passed into the subroutine as an argument. Again, all these steps are demonstrated in the sample program. As these inputs are a function of time, every time the user wishes to change the time step, this process must be repeated.

Finally, now that the static shielding coefficients, the variable parameters/coefficients, and P_{Dyn} have been loaded into common blocks, the top level subroutine *TS07D_JULY_2017* can be called. Note, the signature of this subroutine mirrors that of all the other Tsyganenko magnetic field models, allowing the model to plug into Professor Tsyganenko’s Geopack tracing routines. The subroutine requires six inputs, IOPT, PARMOD, PS, X, Y, and Z. The integer IOPT allows the user to break out the individual field components: 0 = \mathbf{B}_{ext} , 1 = \mathbf{B}_{MP} , 2 = \mathbf{B}_{eq} , 3 = \mathbf{B}_{FAC} .

The double array PARMOD is required for consistency with other Tsyganenko models but is not used in the TS07D model and is thus a dummy input. PS is a double representing the dipole tilt angle in radians and is appended to the coefficient files described above. The X, Y, and Z inputs are the Cartesian coordinates representing the GSM position in which the model will be evaluated. The units are in Earth radii using the standard geomagnetism radius of $1 R_E = 6,371.2 \text{ KM}$. Note, the model will return values even when the supplied position is beyond the modeled magnetopause. To determine if the position is within the modeled magnetopause the subroutine *T96_MGNP_D* must be called. The output of the model are BX, BY, and BZ which correspond to the magnetic field in GSM coordinates in units of nT. The complete set of inputs needed to evaluate the model are summarized in Table 1.

In order to evaluate the total magnetic field, the TS07D model must be used alongside a model for the internal magnetic field \mathbf{B}_{int} , such as the IGRF model (Thébault et al., 2015), an implementation of which is included in the Professor Tsyganenko's Geopack library which can be found at his website: <http://geo.phys.spbu.ru/~tsyganenko/modeling.html>. Additionally, several other useful utilities, including geophysical coordinate conversions and magnetic field line tracing are included in the Geopack library.

The TS07D model has also been incorporated into the IDL Geopack DLM (http://ampere.jhuapl.edu/code/idl_geopack.html), making the model available in the Interactive Data Language (IDL) programming language as a dynamic link module (DLM), as well as the International Radiation Belt Environment Modeling (IRBEM) FORTRAN library (<https://sourceforge.net/projects/irbem/>). The IRBEM library also includes IDL and MATLAB wrappers.

Table 1.The top level TS07D subroutine *TS07D_JULY_2017* arguments.

Name	Type	Input/Output	Frequency	Description
BXTS, BYTS, BZTS, BXTO, BYTO, BZTO, BXTE, BYTE, BZTE	Double Arrays	Input Common Block	Once	Set of static shielding coefficients for the equatorial currents
A	Double Array	Input Common Block	Every time step	An array containing the parameters and coefficients
PDYN	Double	Input Common Block	Every time step	Solar wind P_{DYN} (nPa)
IOPT	Integer	Input	Always	Option to switch between the total model and its individual constituents
PARMOD	Double Array	Input	Always	Not used
PS	Double	Input	Always	The dipole tilt angle (rad)
X	Double	Input	Always	Supplied X_{GSM} position (R_E)
Y	Double	Input	Always	Supplied Y_{GSM} position (R_E)
Z	Double	Input	Always	Supplied Z_{GSM} position (R_E)
BX	Double	Output	Always	The modeled $B_{x,GSM}$ field (nT)
BY	Double	Output	Always	The modeled $B_{y,GSM}$ field (nT)
BZ	Double	Output	Always	The modeled $B_{z,GSM}$ field (nT)

Section 5 – Lessons Learned

Introduction --- More to Come --- JWM

Energetic Particle, Composition, and Thermal Plasma Suite (ECT)

Electric and Magnetic Field Instrument Suite and Integrated Science (EMFISIS)

To a great extent, EMFISIS SOC operations have proceeded as expected and without significant hiccups. However, one key lesson worth noting is the use of autoplot (described above) for both spacecraft integration and test as well as for flight. While this required early development of software to take spacecraft data packets and put them into the cdf data format that EMFISIS uses for its data products, it paid large dividends in not having to go through a second software development cycle for flight data as is common for many instruments on a variety of NASA missions. An additional benefit was that the EMFISIS team had good experience in looking at the data using autoplot prior to launch which allowed very quick verification of proper instrument operations early in the mission.

Electric Field and Waves Suite (EFW) – Lessons Learned

Section 1: X-spec data. How mistakes here informed on PSP product.

asdfasdf

Section 2: Efficiency of burst 1 collection

•Close coordination b/t UMN [Breneman, Tian, Colpitts, Tyler, Kersten, Thaller, Dai] and Berkeley [Schroeder, McTiernan, Bonnell, Rachelson]
Halford; Woodger; Millan
Sample; Johnson; Shumko.

List of constraints

- 1) sample rate (chorus or EMIC?)
- 2) How quiet or active things are or are predicted to be
- 3) Science focus (close conjunctions, loose drift conjunctions?)
- 4) How much interesting data is currently in memory, and how long will it take to play back?
- 5) How many spacecraft contacts are available in the next few days?
- 6) Amount of burst 1 *hopscotch* required.
- 7) Exhaustion of Tohban, etc.
- 8) Prediction of future conjunctions, balloon launches. High altitude winds? Number of simultaneous balloons desired. FIREBIRD campaign focus; WWLLN predictions.

Operation of the EFW burst 1 instrument

This chapter describes the operation of EFW's burst 1 waveform memory, a 30 GB solid state (ground-commanded) memory used to store DC-coupled high cadence 3d electric and magnetic field waveforms. This memory was orders of magnitude larger than any previously flown on an EFW instrument and allowed continuous waveform collection for long durations at rates from 512-16,384 samples/sec. Table 1 presents a breakdown of instrument operation and data collection over the entire mission. Varying collection rates from 512 to 16,384 samples/sec were utilized to target interesting waves and structures in different regions of the magnetosphere. Further details of this data product are presented in Section IV of the EFW bookend chapter.

Table 1. EFW burst 1 capabilities. The green values show all the possible collection rates that were used during the mission, each corresponding to a maximum number of hours of continuous data collection, and a set number of hours of playback per day. Note that these values assume that the EB1 data is telemetered. The playback rate increased by 30% after stopping to telemeter EB1 in 2013. The blue values show for each Probe and mode the total telemetered data volume (hrs) over the entire mission, and the total number of burst data samples ($\times 10^9$). The totals over all the modes are shown in red.

(A) Collection rate (Samples/s)	(B) Temporal memory size	(C) Playback rate (hrs/day)	Total telemetered burst data over entire mission			
			Probes A & B (hrs)		Probes A & B (Samples × 10 ⁹)	
512	24d 8hr	8	1415	1025	2.61	1.89
1,024	12d 4hr	4	180	507	0.67	1.87
2,048	145.6 hr	2	48	44	0.36	0.33
4,096	72.8 hr	1	326	568	4.82	8.38
8,192	36.4 hr	0.5	34	20	1.02	0.62
16,384	18.2 hr	0.25	621	509	36.67	30.06
		Total	2627	2675	46.13	43.14

The burst 1 capabilities made EFW well-suited to focus data collection during targeted science opportunities. For example, higher collection rates targeting chorus waves were generally used in the morning sector, while lower rates targeting EMIC waves were generally used in the afternoon sector. The large memory size allowed ample time to evaluate what to telemeter based on inspection of survey data, particularly at lower collection rates.

In addition, burst 1 collection was often focused during times of close conjunctions between the two probes (lapping events), and this data was used to determine the spatial size of chorus and EMIC wave packets (see Section II in the EFW bookend chapter). EFW also took part in a number of collaborative campaigns by providing high rate collection during magnetic conjunctions with other missions. The three most significant collaborations were:

BARREL (Balloon Array for Radiation Belt Relativistic Electron Losses) - The EFW and BARREL teams worked closely together for six balloon campaigns in order to determine the temporal and spatial characteristics of magnetospheric waves and resulting electron loss. These campaigns included the 2013 and 2014 Antarctica campaigns (roughly Jan-Feb, 2013 and Dec, 2013-Feb, 2014), three Kiruna, Sweden *turnaround* campaigns (7 balloons in Aug, 2015; 7 balloons in Aug, 2016, 2 balloons in June, 2018), and an Antarctica *superpressure* campaign where a single balloon remained aloft from Dec, 2018 to Feb,

2019. Details on these campaigns from the BARREL perspective are discussed by **Woodger et al., 2015**, and in the bookend compilations by **Millan et al.** and **Sample et al.**

FIREBIRD (Focused Investigations of Relativistic Electron Burst Intensity, Range, and Dynamics) and AC6 (AeroCube 6) - EFW provided burst 1 collection during times of close magnetic conjunction in order to further understand the connection of magnetospheric waves (primarily chorus) and microburst precipitation. This included several month-long campaigns from 2015-2019 (see **Johnson et al., 2020** for details).

WWLLN (World Wide Lightning Location Network) - EFW provided burst collection during times when the Van Allen Probes mapped to magnetic field lines over the continental United States in order to study the manner in which lightning activity couples into whistler mode radiation in the inner magnetosphere. The decision to telemeter burst data was based on whether or not significant lightning activity was detected (Zheng et al., 2016).

By mission's end, EFW had telemetered a substantial dataset of spatially separated, high time resolution data during dynamic times, leading to a number of publications (see Table 1, and Section 3 of the EFW bookend chapter).

EFW approaches for increasing burst data return

Unlike more traditional burst memories, burst 1 memory was ground-commanded by an EFW Duty Scientist who decided when to collect, at what rate, and what parts of memory to designate for collection or preservation. Collection was often tailored to a particular science focus such as observations of a particular wave type. For example, collection in the tail region was often tailored to capture VLF waves associated with dynamic injection events.

Due to telemetry constraints, typically only a small fraction of collected data was telemetered.

The decision to play back data was based on survey data (e.g. EFW or EMFISIS, or data from other missions), predicted activity levels, or spatial proximity to another payload (e.g. magnetic conjunctions). Examples include: playback during close approaches of the two Van Allen Probes designed to capture a large spread of spacecraft separations needed to determine the scale sizes of chorus waves; playback during the BARREL and FIREBIRD campaigns focused around magnetic conjunctions; and playback during the WWLLN campaigns based on the amount of lightning activity observed.

At lower collection speeds (~512-2048 samples/sec) the operation of the burst 1 memory was typically straightforward. Days of continuous data could be collected, and with playback rates of up to 1 hr per day the 30 GB burst memory was seldom at risk of being completely filled. In contrast, at the highest sample rate of 16,384 samples/sec a single hour of collection took up a sizable chunk of the memory and about four days to play back (Table 1, column c). Overcommitting to 16,384 samples/sec collection could quickly gridlock the memory, significantly limiting options for the collection of further, possibly more interesting data. Early in the mission gridlocking was avoided by using a highly conservative approach to data collection, reducing the telemetry of interesting data. This was made particularly evident during the first collaborative campaign with the BARREL balloon mission in 2013. This experience showed that during times of intensive collection efforts managing the EFW burst 1 memory was very labor intensive, was associated with a high risk of mistakes, and limited the return of scientifically interesting data. EFW addressed these issues when collecting at high collection speeds by adopting a sprint burst collection methodology and a visual based memory management software package. With these enhancements, along with experience gained along the way, the daily averaged burst data return more than tripled. This is shown in the timeline plots in Figure 1 as the sudden increase in averaged daily (panel c) and monthly (panel a) telemetry and increase in the slope in the total accumulated burst data volume (panel b). The sprint burst collection methodology and visual software are explained in the following subsections.

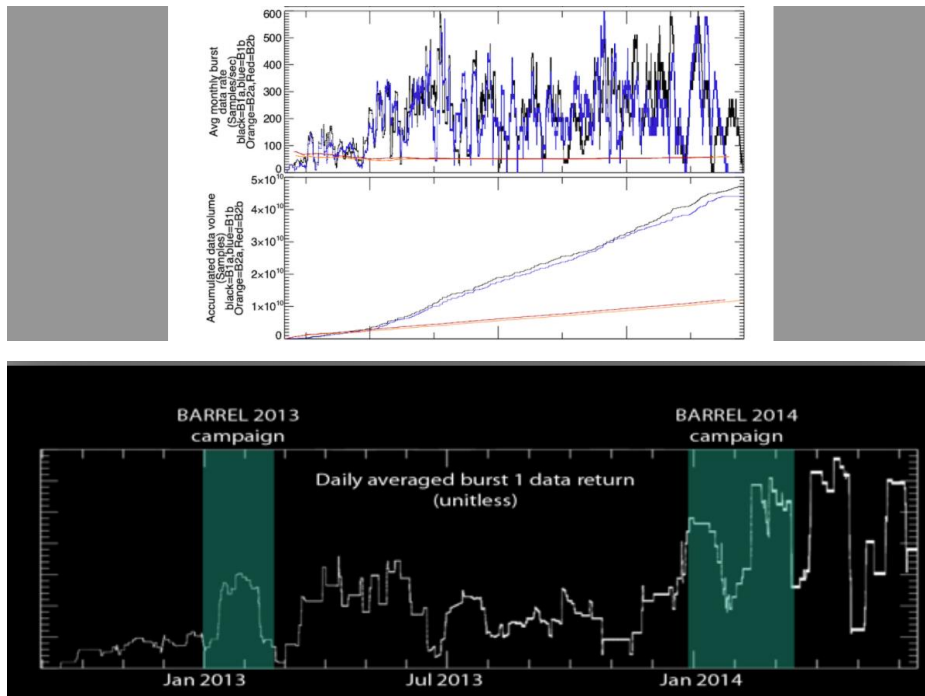


Figure 1. Burst 1 and 2 timeline. Panel a shows the average monthly data rate in samples/sec for both burst 1 (blue) and burst 2 (red), and, for comparison, the inverted DST index (black). Panel b shows the accumulated data volume. The last panel is a zoomed-in view of the averaged monthly rate showing the

significant increase in data volume following the adoption of the sprint methodology and the burst 1 visual memory management software.

Sprint burst collection methodology

The sprint methodology was designed to significantly increase the amount of burst data collected while avoiding memory gridlock by identifying data worth telemetering based on real-time space weather indices and predictive models rather than on-orbit survey data. The survey data were available only after a 2-3 day delay, which was longer than the time it took to fill the burst memory when collecting at 16,384 samples/sec. The sprint methodology involved the following:

- 1) continuous collection of data at 16,384 samples/sec (typically within +/- 2.5 hours of each apogee), and occasional lower rate collection near perigee.
- 2) Use of real-time space weather indices or predictive models to predict what parts of stored memory likely contained interesting wave data.
- 3) Protecting these memory locations against future overwriting.
- 4) Thoughtful selection of which data to telemeter in order to prevent a large backlog of playback requests which would limit future collection

This real-time decision making capability meant that long durations (typically ~5 hrs) of 16,384 samples/sec burst data could be collected at every apogee, and times of potentially interesting data could be flagged and protected before being at risk of being overwritten by a future collection. This approach had the advantage of significantly increasing collection capability, but with the tradeoff of relying on predictive models (rather than actual survey data) to flag interesting times.

The sprint approach was used successfully for the majority of the Van Allen Probe mission and was a significant factor in increasing the volume of telemetered data as indicated in Figure 1.

Visual software

In order to reduce the required efforts for burst 1 operation the EFW team developed a visual burst memory control software package that significantly automated the workflow of managing the burst 1 memory. Figure 2 shows an example of the software's visual output. The top panel indicates information related to the circular burst memory, with the y-axis representing the position in memory. The red curve is the historical trace of the predicted record pointer location as future collection was requested. The thick black lines show actual recorded data, while the thick blue lines show data that has been scheduled for future playback. This presents a clear visual indicator allowing the duty scientist to easily manage the burst 1 memory.

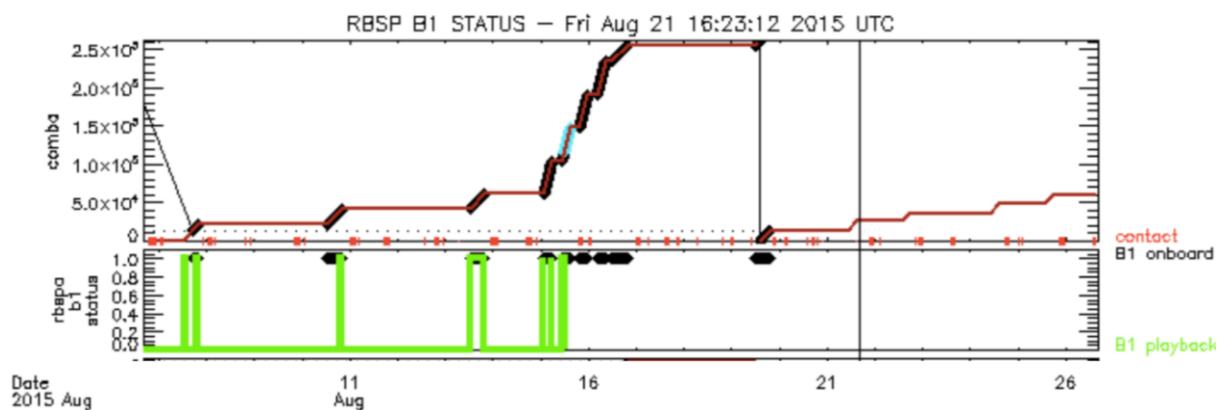


Figure 2. Example of the timeline output of the EFW burst memory manager software for RBSPa. (a) Red lines show the future prediction of the memory pointer location, thick black lines show currently recorded data, and thick blue lines show locations of potentially interesting data that have been designated as protected from overwrite. Spacecraft contacts are shown as the orange ticks, while the vertical line indicates the last time the code was run. (b) The thick black lines are a flattened version of those in panel (a), and the area under the green lines indicates data that has been telemetered.

This software was typically run on a daily basis, giving the Duty Scientist the most up to date picture of the burst memory and allowing them to maximize the return of scientifically useful burst data.

The software was first used at the start of the second BARREL campaign in 2014. Its effect can clearly be seen by the distinct increase in daily averaged burst 1 data return seen in the last panel of Figure 1. This early success set a trend for later collaborations, and this higher data return rate was largely maintained throughout the rest of the mission. Following this approach, EFW could go on to collect an unprecedented dataset of burst waveform data.

As previously discussed, the sprint approach was very labor intensive and stressful. In order to alleviate the required efforts and avoid Tohban burnout and errors the EFW team developed a visual burst memory control software package. This automated a majority of calculations needed to schedule collection and playback, and allowed recording and playback indicators to be predicted with high accuracy over days to weeks, significantly decreasing the Tohban workload. As the above plot shows, this sprint approach and software, implemented prior to the start of the 2014 BARREL campaign, led to significant increases in the rate of data return over time. This early success set a trend for later collaborations, and this higher data return rate was largely maintained throughout the rest of the mission. This huge flexibility and capability allowed for a wide range of dynamic campaigns to be undertaken depending on collection needs (rate, location, occurrence).

Following this approach, EFW could go on to collect an unprecedented dataset of burst waveform data during times of conjunctions, and would set a precedent that would be adopted by MMS. During the FIREBIRD and BARREL campaigns this included hundreds of hours of burst data (see TableXX in EFW Data Quantities chapter).

Radiation Belt Storm Probes Ion Composition Instrument (RBSPICE) – Lessons Learned

Data production planning required upgrades to server and data systems

RBSPICE production system hardware was underspecified for the needs of production for a seven-year mission. The nominal RBSP mission was identified as a two-year mission but the fuel tank was “topped off” so that the mission could extend as long as maneuvering fuel was available. The RBSPICE SOC production hardware was purchased based upon the nominal mission and expected telemetry rates. After the third year of production it became clear to the SOC operations team that the hardware required upgrades as well as the operating systems to allow the overall daily production to occur within a reasonable time frame. As the necessity for reprocessing occurred during the mission due to revised calibrations or identified software defects, the production system hardware was taxed beyond its capabilities. This required purchase of additional hardware for reprocessing activities. Toward the end of the mission, system virtualization was used to handle the required hardware scaling issues. Virtualization was done using a Hyper-V system running on DELL server R720 hardware capable of running a total of ten Virtual Machines (VMs) – five per spacecraft. In the last year of extended mission II, the total reprocessing effort going from telemetry through Level 3 PAP took approximately 2.5 months. After this particular reprocessing effort was finished the DELL hardware was upgraded to a DELL R840 allowing for 20 VMs per spacecraft for full reprocessing efforts reducing the reprocessing effort total time to approximately ½ - 1 month.

Telemetry volume was significantly larger than planned

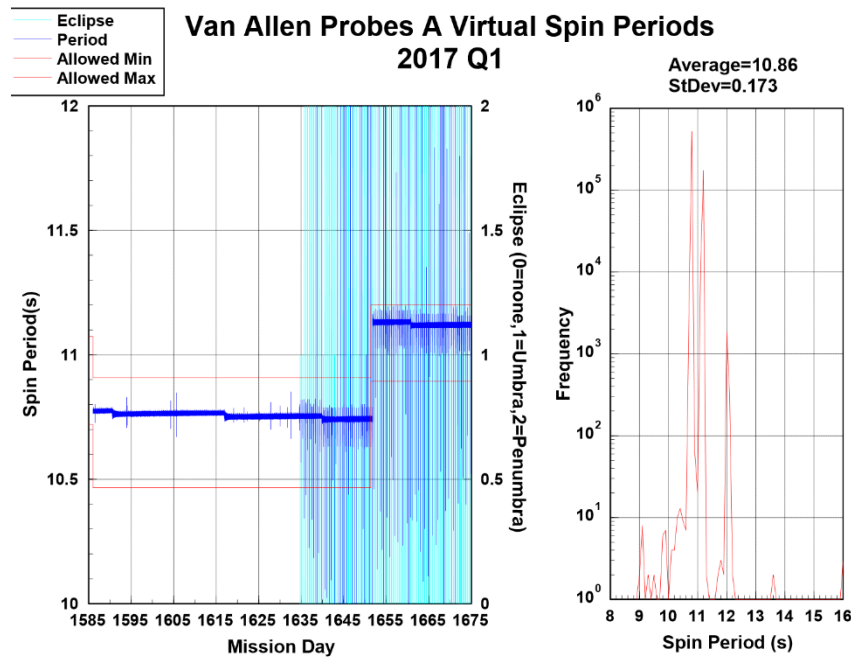
RBSPICE instrument telemetry minimum bitrate to meet the science goals was specified at 1.565 Kbps and the nominal telemetry rate was 3.935 Kbps. During the course of the mission the Mission Operations Center (MOC) team became comfortable that the overall total volume from each spacecraft was not exceeding key thresholds and later in the mission the MOC team released reserve bandwidth for science telemetry. This increased the total RBSPICE bandwidth to JWM kbps. The impact of the transition from the nominal bandwidth to the end of mission bandwidth increased the overall data load on the SOC production systems requiring upgrading from a single stack of 10x4TB hard disk drives (HDD for 40TB total) to 4 stacks of 10x4TB (160 TB) HDDs and a 32x2TB (64TB) HDDs SAN system to provide for redundancy, backup, and offline disaster recovery. The final configuration added another 20x4TB HDDs (80TB) and 24x1.62TB NVMe drives (NMD) (38.8TB) for a tiered drive system providing for faster production coupled with higher throughput.

Programming of the nominal RBSPICE virtual spin period during eclipse

The RBSPICE virtual spin system programmed into the instrument flight software had difficulty maintaining the true spacecraft spin during eclipses. The nominal spin period for each spacecraft programmed into the software was 12 sec. The RBSPICE flight software was designated as NASA Computer Software Configuration Item (CSCI) Class B software with the specification of “Non-Human Space-Rated Software Systems”. The Class B designation exists to prevent and/or significantly reduce the potential impact of the introduction of a software defect into operational flight software. It was determined to not change this software because the virtual spin period existed as part of the flight software and making the change was determined to be expensive for the benefit.

The flight software spin virtualization worked exceptionally well under this configuration except for times in which the spacecraft would go into an eclipse for durations that exceeded several spin periods. The actual spin period of each spacecraft was approximately 10.9 seconds although this period varied

throughout the mission. Since the spacecraft were configured as a sun pointing spacecraft, every three weeks each spacecraft required commanding to adjust orbital pointing to reduce the sun pointing angle and prevent instruments from having a direct UV exposure. Each commanded adjustment caused the spin period to reduce slightly and after a year or more of operations the MOC would need to command each spacecraft with spin-down operations in order to reduce the spin rate (increase the spin period). These spin-down operations occurred five times for SC A on Mission Days (MD) 257 (5/13/13), 624 (5/15/14), 1086 (8/20/15), 1651 (3/7/17), and 2373 (2/27/19-deorbit burn); and twice on SC B on MDs 1086 (8/20/15), and 2493 (6/27/19-deorbit burn).



During an eclipse the RBSPICE flight software would automatically switch from the nominal ~10.9 sec spin period to a 12 second spin period. If this spin to spin offset continued for more than a few spins then the spacecraft pointing information became unreliable as the software would indicate that the instrument was in a sector that was mismatched with respect to the actual instrument pointing. Figure X displays an example of the RBSPICE virtual spin period for the first quarter of 2017. The dark blue curve in the left panel plots record by record values of the virtual spin period of the flight software and the light blue colored shaded areas show periods where the spacecraft would include an eclipse within the orbit. The plot is done during a time when the spacecraft is commanded during MD 1651 to do a spin down maneuver increasing the spin period. The variation of the virtual spin is very small while the spacecraft is outside an eclipse period but has significant variation during eclipse periods. The right-side panel displays the distribution of spin periods showing that the majority are well within the nominal spacecraft spin range. That figure also shows a smaller number of times when the coded 12 sec period is utilized during an eclipse and when the spacecraft exits the umbra of the eclipse and reacquires the sun then the flight software does some dramatic changes in the virtual spin period to either slow down or catch up to the actual spacecraft spin. The number of spins required to resynch the virtual spin with the actual spin was less than two or three spins. During the times when the virtual spin was out of synch

with the spacecraft spin, the accumulation records were tagged by the flight software with sector numbers shifted in phase compared to the actual spacecraft pointing. During these times the quality flags of the Level 3 and above RBSPICE data is tagged as bad.

Section 6 – References

Acton, C.H.; "Ancillary Data Services of NASA's Navigation and Ancillary Information Facility;" Planetary and Space Science, Vol. 44, No. 1, pp. 65-70, 1996.

Acton, C.H., N. Bachman, B. Semenov, E. Wright; A look toward the future in the handling of space science mission geometry; Planetary and Space Science (2017), DOI 10.1016/j.pss.2017.02.013

Booch, G. I. Jacobson, J. Rumbaugh, The Unified Modeling Language Reference Manual, Addison Wesley Longman, Inc., 1999, ISBN: 020130998X

Bourdarie, S., B. Blake, J. B. Cao, R. Friedel, Y. Miyoshi, M. Panasyuk, C. Underwood, Panel on Radiation Belt Environmental Modeling (PRBEM) Standard File Format Guidelines, COSPAR ISTP PRBEM Website: <https://cosparhq.cnes.fr/scientific-structure/panels/panel-on-radiation-belt-environment-modeling-prbem/> and <https://craterre.onera.fr/prbem/home.html>

COSPAR ISTP PRBEM Committee, Panel on Radiation Belt Environment Modeling File Format Specifications, <http://craterre.onecert.fr/prbem/home.html>, 2010.

Packet Telemetry. Recommendation for Space Data Systems Standards, CCSDS 102.0-B-5. Blue Book. Issue 5. Washington, D.C.: CCSDS, November 2000.

Fox, N. J., and J.L. Burch, (eds). *The Van Allen Probes Mission*. Springer, Boston, MA, 2014.

Fukushima, T., Time ephemeris, Astronomy and Astrophysics, vol. 294. pp. 895–906, 1995.

Kessel, R. L., R. M. Candey, S. W. Hsieh, S. Kayser, "Visualization of International Solar-Terrestrial Physics Program (ISTP) data", *Visualization techniques in space and atmospheric sciences*, 85-93, 1995

Krimigis, S & Mitchell, D & Hamilton, D & Krupp, N & Livi, Stefano & Roelof, E & Dandouras, J & Armstrong, T. & Mauk, B & Paranicas, C & Brandt, P & Bolton, Scott & Cheng, Andrew & Choo, T & Gloeckler, George & Hayes, J & Hsieh, K & Ip, Wing-Huen & Jaskulek, S & Woch, J. (2005). Dynamics of Saturn's Magnetosphere from MIMI During Cassini's Orbital Insertion. *Science* (New York, N.Y.). 307. 1270-3. 10.1126/science.1105978.

Laundal, K.M., Richmond, A.D. Magnetic Coordinate Systems. *Space Sci Rev* **206**, 27–59 (2017). DOI:10.1007/s11214-016-0275-y

Manweiler, J. W., H. Zwiener, RBSPICE Data Handbook, 2019, RBSPICE, http://rbspice.ftcs.com/RBSPICE%20Data%20Handbook_Rev_f.pdf

Mitchell D.G. et al. (2013) Radiation Belt Storm Probes Ion Composition Experiment (RBSPICE). In: Fox N., Burch J.L. (eds) *The Van Allen Probes Mission*. Springer, Boston, MA. DOI:10.1007/978-1-4899-7433-4_8

NASA NAIF SPICE SCLOCK Type 1 specification, https://naif.jpl.nasa.gov/pub/naif/toolkit_docs/C/req/sclk.html , 2010.

Reeves et al., 2021, this volume

Rumbaugh, J., I. Jacobson, G. Booch, The Unified Modeling Language Reference Manual, 2nd Edition, Pearson Higher Education, 2004, ISBN: 978-0-321-24562-5

Wiltamuth, S., Hejlsberg, A., Golde, P. (2006). *The C# Programming Language*. Malawi: Addison-Wesley, ISBN: 9780321562999

Angelopoulos, V., Cruce, P., Drozdov, A. *et al.* The Space Physics Environment Data Analysis System (SPEDAS). *Space Sci Rev* **215**, 9 (2019). <https://doi.org/10.1007/s11214-018-0576-4>

Baker, D.N., Kanekal, S.G., Hoxie, V. *et al.* The Relativistic Electron-Proton Telescope (REPT) Investigation: Design, Operational Properties, and Science Highlights. *Space Sci Rev* **217**, 68 (2021). <https://doi.org/10.1007/s11214-021-00838-3>

Boyd, A. J., *et al.* (2021). RBSP-ECT Combined Pitch Angle Resolved Electron Flux Data Product. *Journal of Geophysical Research*, **126**(3), e2867, <https://doi.org/10.1029/2020JA02837>

Burton, R. K., McPherron, R. L., & Russell, C. T. (1975). An empirical relationship between interplanetary conditions and Dst. *Journal of Geophysical Research*, **80**(31), 4204–4214. <https://doi.org/10.1029/JA080i031p04204>

Cover, T. M., & Hart, P. E. (1967). Nearest neighbor pattern classification. *IEEE Transactions on Information Theory*, **13**(1), 21–27. <https://doi.org/10.1109/TIT.1967.1053964>

Gonzalez, W. D., Joselyn, J. A., Kamide, Y., Kroehl, H. W., Rostoker, G., Tsurutani, B. T., & Vasyliunas, V. M. (1994). What is a geomagnetic storm? *Journal of Geophysical Research*, **99**(A4), 5771. <https://doi.org/10.1029/93JA02867>

Henderson, M. G., *et al.* (2021), magesphem paper of unknown title, this volume.

Henderson, M. G., Morley, S. K., Niehof, J. T., and Larsen, B. A. (2018), LANLGeoMag. <https://doi.org/10.5281/zenodo.1133781>.

Iijima, T., & Potemra, T. A. (1976). Field-aligned currents in the dayside cusp observed by Triad. *Journal of Geophysical Research*, **81**(34), 5971–5979. <https://doi.org/10.1029/JA081i034p05971>

Iyemori, T. (1990). Storm-time magnetospheric currents inferred from mid-latitude geomagnetic field variations. *Journal of Geomagnetism and Geoelectricity*, **42**, (11), 1249–1265 (1990). <https://doi.org/10.5636/jgg.42.1249>

Mitchell, T. M. (1997). *Machine learning*, (first ed.). New York, NY: McGraw-Hill, Inc.

Press, W. H., Teukolsky, S. A., Vetterling, W. T., & Flannery, B. P. (1992). *Numerical recipes in Fortran 77*, Cambridge, ed. 2, pp. 51–63

Shue, J. H., Song, P., Russell, C. T., Steinberg, J. T., Chao, J. K., Zastenker, G., *et al.* (1998). Magnetopause location under extreme solar wind conditions. *Journal of Geophysical Research*, **103**(A8), 17,691–17,700. <https://doi.org/10.1029/98JA01103>

Sitnov, M. I., Tsyganenko, N. A., Ukhorskiy, A. Y., & Brandt, P. C. (2008). Dynamical data-based modeling of the storm-time geomagnetic field with enhanced spatial resolution. *Journal of Geophysical Research*, **113**, A07218. <https://doi.org/10.1029/2007JA013003>

- Sitnov, M. I., Tsyganenko, N. A., Ukhorskiy, A. Y., Anderson, B. J., Korth, H., Lui, A. T. Y., & Brandt, P. C. (2010). Empirical modeling of a CIR-driven magnetic storm. *Journal of Geophysical Research*, 115, (A7), A07231. <https://doi.org/10.1029/2009JA015169>
- Sitnov, M. I., Ukhorskiy, A. Y., & Stephens, G. K. (2012). Forecasting of global data-binning parameters for high-resolution empirical geomagnetic field models. *Space Weather*, 10, S09001. <https://doi.org/10.1029/2012SW000783>
- Skoug, R. M. et al. (2021), HOPE final paper (title unknown), this volume.
- Stephens, G. K., Sitnov, M. I., Kissinger, J., Tsyganenko, N. A., McPherron, R. L., Korth, H., & Anderson, B. J. (2013). Empirical reconstruction of storm time steady magnetospheric convection events. *Journal of Geophysical Research: Space Physics*, 118, 6434–6456. <https://doi.org/10.1002/jgra.50592>
- Stephens, G. K., Sitnov, M. I., Korth, H., Tsyganenko, N. A., Ohtani, S., Gkioulidou, M., & Ukhorskiy, A. Y. (2019). Global empirical picture of magnetospheric substorms inferred from multimission magnetometer data. *Journal of Geophysical Research: Space Physics*, 124, 1085–1110. <https://doi.org/10.1029/2018JA025843>
- Stern, D. P. (1987), Tail modeling in a stretched magnetosphere: 1. Methods and transformations, *Journal of Geophysical Research*, 92, 4437–4448. <https://doi.org/10.1029/JA092iA05p04437>
- Thébault, E., Finlay, C. C., Beggan, C. D., Alken, P., Aubert, J., Barrois, O., et al. (2015). International geomagnetic reference field: The 12th generation. *Earth, Planets and Space*, 67(1), 79. <https://doi.org/10.1186/s40623-015-0228-9>
- Tsyganenko, N. A. (1991). Methods for quantitative modeling of the magnetic field from Birkeland currents. *Planetary and Space Science*, 39(4), 641–654. [https://doi.org/10.1016/0032-0633\(91\)90058-I](https://doi.org/10.1016/0032-0633(91)90058-I)
- Tsyganenko, N. A. (1995). Modeling the Earth's magnetospheric magnetic field confined within a realistic magnetopause. *Journal of Geophysical Research*, 100(A4), 5599–5612. <https://doi.org/10.1029/94JA03193>
- Tsyganenko, N. A. (1996). Effects of the solar wind conditions on the global magnetospheric configuration as deduced from data-based field models, in *Proceedings of the ICS-3 Conference on Substorms*, Eur. Space Agency Spec. Publ., ESA SP-389, 181.
- Tsyganenko, N. A. (1998). Modeling of twisted/warped magnetospheric configurations using the general deformation method. *Journal of Geophysical Research*, 103(A10), 23,551–23,563. <https://doi.org/10.1029/98JA02292>
- Tsyganenko, N. A. (2002). A model of the magnetosphere with a dawn-dusk asymmetry, 1, mathematical structure. *Journal of Geophysical Research*, 107(A8), SMP 12-1–SMP 12-15. <https://doi.org/10.1029/2001JA000219>
- Tsyganenko, N. A. (2013). Data-based modeling of the Earth's dynamic magnetosphere: A review. *Annales Geophysicae*, 31(10), 1745–1772. <https://doi.org/10.5194/angeo-31-1745-2013>
- Tsyganenko, N. A., & Sitnov, M. I. (2007). Magnetospheric configurations from a high-resolution data-based magnetic field model. *Journal of Geophysical Research*, 112, A06225. <https://doi.org/10.1029/2007JA012260>

Vassiliadis, D. (2006). Systems theory for geospace plasma dynamics. *Reviews of Geophysics*, 44, RG2002. <https://doi.org/10.1029/2004RG000161>

Voskresenskaya, M., et al. (2021). Data correction algorithms for the final processing of HOPE data, this volume.

Angelopoulos, V., Cruce, P., Drozdov, A. et al. The Space Physics Environment Data Analysis System (SPEDAS). *Space Sci Rev* **215**, 9 (2019). <https://doi.org/10.1007/s11214-018-0576-4>

Baker, D.N., Kanekal, S.G., Hoxie, V. et al. The Relativistic Electron-Proton Telescope (REPT) Investigation: Design, Operational Properties, and Science Highlights. *Space Sci Rev* 217, 68 (2021). <https://doi.org/10.1007/s11214-021-00838-3>

Boyd, A. J., et al. (2021). RBSP-ECT Combined Pitch Angle Resolved Electron Flux Data Product. *Journal of Geophysical Research*, 126(3), e2867, <https://doi.org/10.1029/2020JA02837>

Burton, R. K., McPherron, R. L., & Russell, C. T. (1975). An empirical relationship between interplanetary conditions and Dst. *Journal of Geophysical Research*, 80(31), 4204–4214. <https://doi.org/10.1029/JA080i031p04204>

Cover, T. M., & Hart, P. E. (1967). Nearest neighbor pattern classification. *IEEE Transactions on Information Theory*, 13(1), 21–27. <https://doi.org/10.1109/TIT.1967.1053964>

Gonzalez, W. D., Joselyn, J. A., Kamide, Y., Kroehl, H. W., Rostoker, G., Tsurutani, B. T., & Vasyliunas, V. M. (1994). What is a geomagnetic storm? *Journal of Geophysical Research*, 99(A4), 5771. <https://doi.org/10.1029/93JA02867>

Henderson, M. G., et al. (2021), magephem paper of unknown title, this volume.

Henderson, M. G., Morley, S. K., Niehof, J. T., and Larsen, B. A. (2018), LANLGeoMag. <https://doi.org/10.5281/zenodo.1133781>.

Iijima, T., & Potemra, T. A. (1976). Field-aligned currents in the dayside cusp observed by Triad. *Journal of Geophysical Research*, 81(34), 5971–5979. <https://doi.org/10.1029/JA081i034p05971>

Iyemori, T. (1990). Storm-time magnetospheric currents inferred from mid-latitude geomagnetic field variations. *Journal of Geomagnetism and Geoelectricity*, 42, (11), 1249–1265 (1990). <https://doi.org/10.5636/jgg.42.1249>

Mitchell, T. M. (1997). *Machine learning*, (first ed.). New York, NY: McGraw-Hill, Inc.

Press, W. H., Teukolsky, S. A., Vetterling, W. T., & Flannery, B. P. (1992). *Numerical recipes in Fortran 77*, Cambridge, ed. 2, pp. 51–63

Shue, J. H., Song, P., Russell, C. T., Steinberg, J. T., Chao, J. K., Zastenker, G., et al. (1998). Magnetopause location under extreme solar wind conditions. *Journal of Geophysical Research*, 103(A8), 17,691–17,700. <https://doi.org/10.1029/98JA01103>

- Sitnov, M. I., Tsyganenko, N. A., Ukhorskiy, A. Y., & Brandt, P. C. (2008). Dynamical data-based modeling of the storm-time geomagnetic field with enhanced spatial resolution. *Journal of Geophysical Research*, 113, A07218. <https://doi.org/10.1029/2007JA013003>
- Sitnov, M. I., Tsyganenko, N. A., Ukhorskiy, A. Y., Anderson, B. J., Korth, H., Lui, A. T. Y., & Brandt, P. C. (2010). Empirical modeling of a CIR-driven magnetic storm. *Journal of Geophysical Research*, 115, (A7), A07231. <https://doi.org/10.1029/2009JA015169>
- Sitnov, M. I., Ukhorskiy, A. Y., & Stephens, G. K. (2012). Forecasting of global data-binning parameters for high-resolution empirical geomagnetic field models. *Space Weather*, 10, S09001. <https://doi.org/10.1029/2012SW000783>
- Skoug, R. M. et al. (2021), HOPE final paper (title unknown), this volume.
- Stephens, G. K., Sitnov, M. I., Kissinger, J., Tsyganenko, N. A., McPherron, R. L., Korth, H., & Anderson, B. J. (2013). Empirical reconstruction of storm time steady magnetospheric convection events. *Journal of Geophysical Research: Space Physics*, 118, 6434–6456. <https://doi.org/10.1002/jgra.50592>
- Stephens, G. K., Sitnov, M. I., Korth, H., Tsyganenko, N. A., Ohtani, S., Gkioulidou, M., & Ukhorskiy, A. Y. (2019). Global empirical picture of magnetospheric substorms inferred from multimission magnetometer data. *Journal of Geophysical Research: Space Physics*, 124, 1085–1110. <https://doi.org/10.1029/2018JA025843>
- Stern, D. P. (1987), Tail modeling in a stretched magnetosphere: 1. Methods and transformations, *Journal of Geophysical Research*, 92, 4437–4448. <https://doi.org/10.1029/JA092iA05p04437>
- Thébault, E., Finlay, C. C., Beggan, C. D., Alken, P., Aubert, J., Barrois, O., et al. (2015). International geomagnetic reference field: The 12th generation. *Earth, Planets and Space*, 67(1), 79. <https://doi.org/10.1186/s40623-015-0228-9>
- Tsyganenko, N. A. (1991). Methods for quantitative modeling of the magnetic field from Birkeland currents. *Planetary and Space Science*, 39(4), 641–654. [https://doi.org/10.1016/0032-0633\(91\)90058-I](https://doi.org/10.1016/0032-0633(91)90058-I)
- Tsyganenko, N. A. (1995). Modeling the Earth's magnetospheric magnetic field confined within a realistic magnetopause. *Journal of Geophysical Research*, 100(A4), 5599–5612. <https://doi.org/10.1029/94JA03193>
- Tsyganenko, N. A. (1996). Effects of the solar wind conditions on the global magnetospheric configuration as deduced from data-based field models, in *Proceedings of the ICS-3 Conference on Substorms*, Eur. Space Agency Spec. Publ., ESA SP-389, 181.
- Tsyganenko, N. A. (1998). Modeling of twisted/warped magnetospheric configurations using the general deformation method. *Journal of Geophysical Research*, 103(A10), 23,551–23,563. <https://doi.org/10.1029/98JA02292>
- Tsyganenko, N. A. (2002). A model of the magnetosphere with a dawn-dusk asymmetry, 1, mathematical structure. *Journal of Geophysical Research*, 107(A8), SMP 12-1–SMP 12-15. <https://doi.org/10.1029/2001JA000219>
- Tsyganenko, N. A. (2013). Data-based modeling of the Earth's dynamic magnetosphere: A review. *Annales Geophysicae*, 31(10), 1745–1772. <https://doi.org/10.5194/angeo-31-1745-2013>

Tsyganenko, N. A., & Sitnov, M. I. (2007). Magnetospheric configurations from a high-resolution data-based magnetic field model. *Journal of Geophysical Research*, 112, A06225. <https://doi.org/10.1029/2007JA012260>

Vandergriff J., R. Weigel, J. Faden, D. A. Roberts, B. Harris, R. Candey, N. Lal, D. Lindholm, T. Baltzer, T. King, Keeping Everyone HAPI: Achieving Interoperability for Heliophysics and Planetary Time Series Data, Earth and Space Science Open Archive, 2019, DOI:10.1002/essoar.10500433.1

Vassiliadis, D. (2006). Systems theory for geospace plasma dynamics. *Reviews of Geophysics*, 44, RG2002. <https://doi.org/10.1029/2004RG000161>

Voskresenskaya, M., et al. (2021). Data correction algorithms for the final processing of HOPE data, this volume.

Johnson, A.T. et al. (2020), "The FIREBIRD-II CubeSat mission: Focused investigations of relativistic electron burst intensity, range, and dynamics", *Review of Scientific Instruments* 91, 034503 (2020) <https://doi.org/10.1063/1.5137905>

Woodger, L. A., Halford, A. J., Millan, R. M., McCarthy, M. P., Smith, D. M., Bowers, G. S., Sample, J. G., Anderson, B. R., and Liang, X. (2015), A summary of the BARREL campaigns: Technique for studying electron precipitation. *J. Geophys. Res. Space Physics*, 120, 4922– 4935. doi: [10.1002/2014JA020874](https://doi.org/10.1002/2014JA020874).

Wygant, J. R., et al. (2014). The Electric Field and Waves Instruments on the Radiation Belt Storm Probes mission. In *The Van Allen Probes mission* (Vol. 9781489974334, pp. 183-220). Springer US. https://doi.org/10.1007/978-1-4899-7433-4_6

Zheng, H. et al. (2016), A statistical study of whistler waves observed by Van Allen Probes (RBSP) and lightning detected by WWLLN, *J. Geophys. Res. Space Physics*, 121, doi:10.1002/2015JA022010

Section 7 – Appendices

Appendix A –

NASA Science Data Levels

NASA	CODMAC	Description
Packet data	Raw – Level 1	Telemetry data stream as received at the ground station, with science and engineering data embedded.
Level 0	Edited – Level 2	Instrument science data (e.g., raw voltages, counts) at full resolution, time ordered, with duplicates and transmission errors removed.
Level 1A	Calibrated - Level 3	Level 0 data that have been located in space and may have been transformed (e.g., calibrated, rearranged) in a reversible manner and packaged with needed ancillary and auxiliary data (e.g., radiances with the calibration equations applied).
Level 1B	Resampled - Level 4	Irreversibly transformed (e.g., resampled, remapped, calibrated) values of the instrument measurements (e.g., radiances, magnetic field strength).
Level 1C	Derived- Level 5	Level 1A or 1B data that have been resampled and mapped onto uniform space-time grids. The data are calibrated (i.e., radiometrically corrected) and may have additional corrections applied (e.g., terrain correction).
Level 2	Derived - Level 5	Geophysical parameters, generally derived from Level 1 data, and located in space and time commensurate with instrument location, pointing, and sampling.
Level 3	Derived - Level 5	Geophysical parameters mapped onto uniform space-time grids.